Osaka University
Doctoral Thesis

Exploring Exoplanets with Detailed Analysis of Gravitational Microlensing Events including High-order Effects

Author

Shota Miyazaki

February 2021

Acknowledgements

I would like to express my sincere gratitude for the support and cooperation of many people in completing this doctoral thesis. I think the reason, why I was able to find what I wanted to do and be passionate about it during graduate school, is because I blessed with excellent environments around me. Thank you so much.

I thank Professor Takahiro Sumi, an unparalleled adviser of my research, for providing strong supports for this thesis. He has never built a ”teacher-student” relationship with me but always treated me as a researcher since I became a member of the laboratory. Although I had little experience being spoonfeeded by him, he always gives chances to me to study, discuss, and boost each other. Needless to say, I think he was teaching me how to live as a researcher.

I thank Professor Emeritus Hiroshi Shibai for having been an advisor till one year ago. He provided me with enormous lessons not only for being a researcher but also for being a person. His strict and truthful words always inspired me. I would never have thought of entering a doctoral program without him although I guess he may dislike such a motivation.

I thank all the senior researchers, especially Naoki Koshimoto, Daisuke Suzuki, Kento Masuda, Masayuki Nagakane, Taro Matsuo, and Yuki Hirao who spent countless hours discussing research and also talking with me at informal chitchat. I have been benefited so much from their continuous supports and kind help. When I was frustrated or in depression, they helped me so many times and brighten my moods. Without them, I would have lost my mind halfway.

I thank all the members of the MOA and PRIME collaboration for supporting this work. I would like to thank David P. Bennett, Nicholas J. Rattenbury, Ian A. Bond, Clément Ranc, Yasushi Muraki, Fumio Abe, Yutaka Matsubara, and Phillip Yock for providing me with many valuable advice and suggestions. In particular, Dave always turns his attention to my research and gives appropriate advice. Their deep insights and dedicated help always motivated me so many times. I thank Paul J. Tristriam and Nigel Frost at Mt.John Observatory in New Zealand. Thanks to them, my observation life at Mt.John Observatory was far from painful. I hope that the day will come when we can observe with them again.

I thank all the staffs, and the doctoral and master students working and studying with me in Osaka University, especially Natsuko Okuzawa, Ayae Yamamoto, Tomohiro Mori, Yoshito Tani, Erina Otsuka, Shohei Goda, Masayuki Ido, Yuki Satoh, Morito Saiki, Rintaro Kirikawa, Tsubasa Yamawaki, Hikaru Shoji. They provided me with a happy and productive student life in Osaka University and have been always encouraging to me.

I thank Samson A. Johnson and Matthew T. Penny for being great collaborators in my research. I was very happy to be blessed with sincere and supportive collaborators like them.

Finally, I would like to give special thanks to my family, Ryoji, Miki, Erika, Yusuke, and Kon, for their kind supports and unconditional love.

Abstract

In this thesis, I present two applications of gravitational microlensing into the study of exoplanet survey.

In chapter 1, I will present an overview of research targets, exoplanets, and brown dwarfs, that can be probed by microlensing. I will also present the introduction and motivation to research in this thesis. In Chapter 2, I review a basic theory of gravitational microlensing and its practical applications. In Chapter 3, I present the observations and detailed analysis of the planetary microlensing event OGLE-2013-BLG-0911. Detailed analysis leads to the conclusion that the lens system is an M-dwarf orbited by a massive Jupiter companion at very close ($M_{\rm host} = 0.30^{+0.08}_{-0.06}\ M_{\odot}$, $M_{\rm comp} = 10.1^{+2.9}_{-2.2}\ M_{\rm Jup}$, $a_{\rm exp} = 0.40^{+0.05}_{-0.04}$ au) or wide ($M_{\rm host} = 0.28^{+0.10}_{-0.08}\ M_{\odot}$, $M_{\rm comp} = 9.9^{+3.8}_{-3.5}\ M_{\rm Jup}$, $a_{\rm exp} = 18.0^{+3.2}_{-3.2}$ au) separation. In the analysis, we succeed to detect the significant xallarap (source orbital motion) effect which reveals that there is a late-type M-dwarf companion to the host in the source system. This is the first demonstration that dark, low-mass objects in the Galactic bulge can be detected and characterized via xallarap. In Chapter 4, I present the analysis that studies the xallarap effect with the simulated data of the *Nancy Grace Roman Space Telescope* (*Roman*) to measure the physical properties of exoplanets orbiting microlensed source stars in the Galactic bulge. The analysis shows that the *Roman* Galactic Exoplanet Survey (RGES) can detect warm Jupiters with masses down to $0.5\ M_{\rm Jup}$ and orbital periods up to 30 days, and that *Roman* will detect ~ 10 hot and warm Jupiters and ~ 30 close-in BDs around microlensed source stars during the RGES. It is also shown that the detections are likely to be accompanied by the measurements of the companion's masses and orbital elements, which will aid in the study of the physical properties for the close-in planet and BD populations in the Galactic bulge. Finally, in Chapter 5, I summarize the analyses in this thesis and present a conclusion.

Contents

Chapter 1

Introduction

1.1 Exoplanets

Although many unexplained and unknown (unrecognized) things still certainly exist, our understanding of planet formation has expanded significantly over the last few decades. Prior to the first exoplanet discovery, our knowledge about planet formation was based only on our solar system, and most theories of planet formation had been limited only to explain the solar system. To date, more than 4200 exoplanets have been found (Akeson et al., 2013), and their distributions of physical parameters (e.g. masses, orbital periods, and so on) have revealed a diversity of planetary systems that are completely different from our solar system. Such a diversity of planetary system was challenging to the predictions from conventional theories and also let us recognize the difficulty understanding the nature of planetary formation and evolution. It is difficult to observe the planet formation directly since most protoplanetary disks are optically-thick and the timescale of planet formation is thought to be several million years. The exoplanet distribution enables us to compare with the theoretical predictions and provides us with new suggestions on the planetary formation process and evolution (e.g., Suzuki et al., 2018). Therefore, revealing the distribution is important. Ultimately, understanding planet formation can lead to answer the question of whether Earth-like habitable planets are common in the universe and whether extraterrestrials other than us are common, i.e. are we alone in the universe?

1.1.1 Basic Formation Theory

Core Accretion Model

Planetary formation theories have developed to explain how our solar system and other exoplanetary systems formed. One of the current mainstream theories is the core accretion model (Hayashi, 1981; Lissauer, 1993; Pollack et al., 1996), where dust in proto-planetary disks settle in the mid plane and then a lot of planetesimals are generated and accumulated in places that local surface densities are high. Finally, planets form via collision growth of many planetesimals in the protoplanetary disks. Figure 1.1 shows a schematic view of the

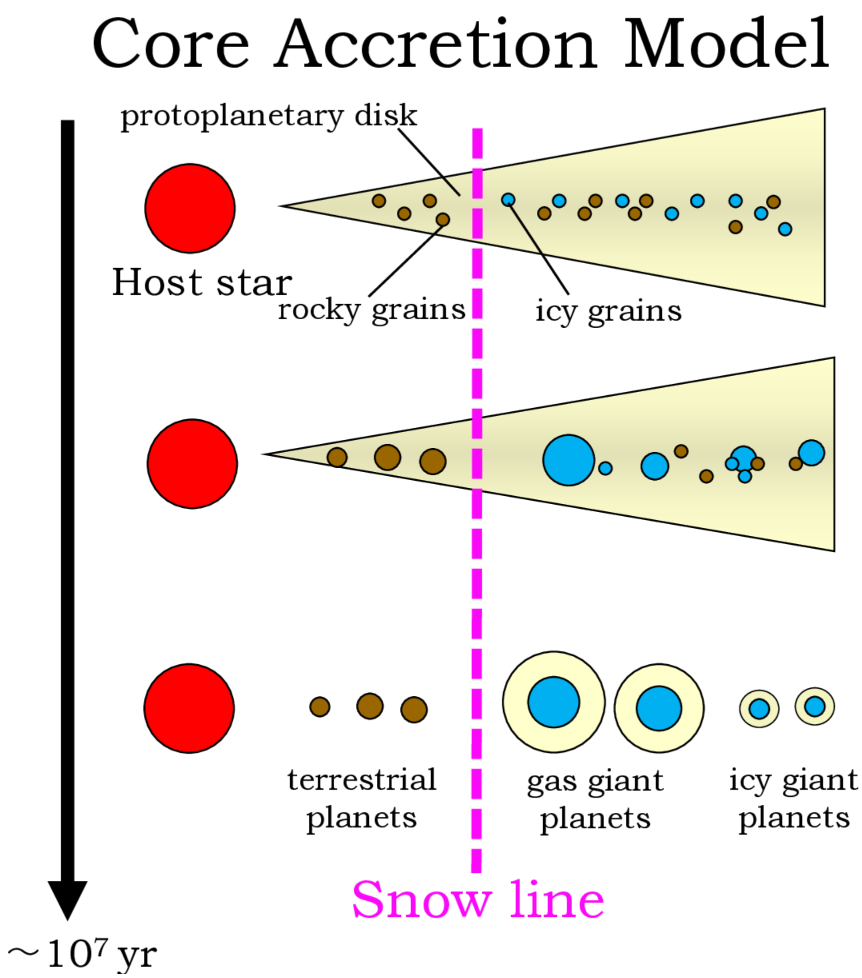

Figure 1.1 A schematic view of the core accretion model. Inside the snow line where temperatures are higher, only rocky and metallic grains can condense. Beyond the snow line, hydrogen compounds like water can condense in addition to the rocky and metallic grains. As a result, the surface density of solid grains in the disk will increase significantly at the snow line. This increase will change the timescale and mass scale of forming planets beyond the snow line.

core accretion model. Many problems remain in this theory but I provide an overview of the core accretion theory.

1. A molecular cloud contracts as it rotates. The contraction in the radial direction stops at a certain size due to the centrifugal force, but the contraction in the axial direction continues. As a result, a protoplanetary disk forms, which is composed of gaseous components and dust grains.

2. The dust grains are subjected to the gravitational and centrifugal forces from the central star. The combined force causes the dust grains to settle on the midplane

of the disk. When the density of the dust grains exceeds a threshold, it causes gravitational instability. The dust grains forms clumps of a few kilometers in size [1]. These clumps are called as planetesimal. Terrestrial planets and solid cores of gas giant planets are formed by repeated collisions and mergers of the planetesimals.

3. Outside the snow line where water can be condensed into solid ice grains, larger planetesimals can form rapidly because more solid materials are available and then massive planetary-cores with $M \geq 5-10 M_{\oplus}$ can become Jovian planets by efficiently capturing surrounding gaseous materials (Hayashi et al., 1985). This rapid accretion process is called runaway gas accretion and it occurs when the mass of the envelope gas surrounding the planetary-core is beyond the planetary-core mass (Pollack et al., 1996). For wider orbits, the planetary-cores grow slowly and are unlikely to collect gas efficiently before the gas disk dissipates. They become icy planets like Neptune and Uranus.

One of the key points in the core accretion theory is that planets form most efficiently beyond the snow line (Ida & Lin, 2005; Kennedy & Kenyon, 2008). The location of the snowline is important for understanding the planetary formation because it can be considered as a boundary that significantly affects planetary compositions and masses. However, it depends on the conditions of the disk (e.g., accretion rate, dust properties) and changes during the disk evolution (e.g. Oka et al., 2011). I present one of the simplest examples for snow line. For an optically thin disk (Hayashi, 1981) assuming blackbody dust grains, temperature of the grains in thermal equilibrium with the radiation of the host star is

$$\begin{aligned} 4\pi d^2 \times \sigma_{\rm SB} T^4 &= \frac{L_{\rm Host}}{4\pi r^2} \times \pi d^2 \\ T = \left(\frac{L_{\rm Host}}{16\pi\sigma_{\rm SB} r^2}\right)^{1/4} &\approx 280{\rm K} \left(\frac{1{\rm au}}{r}\right)^{1/2} \left(\frac{L_{\rm Host}}{L_{\odot}}\right)^{1/4} \end{aligned}$$

where d is the radius of dust grains, $L_{\rm Host}$ is the luminosity of the host, and r is the distance from the host star. With a low pressure condition of gas in the disk, freezing temperature of water is ~ 170 K and then the snow line is provided as

$$r_{\rm snow} \approx 2.7 \text{ au} \left(\frac{L_{\rm Host}}{L_{\odot}}\right)^{1/2}.$$

For main-sequence stars, the distance of the snow line scales as ~ 2.7 au $(M_{\rm Host}/M_{\odot})^2$ since $L_{\rm Host} \propto M_{\rm Host}^4$ (Ida & Lin, 2004). Note that the mass-luminosity relation for main-sequence stars also depends on the stellar age.

[1] It is known that $\sim$ 1m sized dust is difficult to form and rapidly falls into the host star, which is called the "meter-size barrier" (e.g. Weidenschilling, 1977). Though there are no clear solutions to this problem to date, some theories avoid the problem by a short timescale of the growth from 1cm to 1km via self gravitational instability and/or pebble accretion (Youdin & Shu, 2002; Youdin & Goodman, 2005).

Pros and Cons of Core Accretion Model

The core accretion model can explain many observational facts. First, gas giant planets have solid cores of $\sim 10\%$ of their masses and internal density profiles biased toward their cores (Wahl et al., 2017). On the other hand, molecular clouds that are materials to form planets are composed of gaseous and solid components. The compositional ratio of solid is an order of 1%. If gas giant planets form via gravitational instability, the composition of the planets would be the same as molecular clouds, and their structures would be the mixtures of each component[2]. The model can explain differences in size for terrestrial and gas giant planets. The model is also supported by several observational results that study the planet occurrence rate depending on the physical properties of the host stars, like metallicity and mass (e.g., Santos et al., 2001; Johnson et al., 2010; Santerne et al., 2016).

One of the main problems with the core accretion model is that it takes so long time to form Jovian and Neptune-like planets. The typical timescales to form 0.1 $M_\oplus$ planetary-cores in Jupiter and Neptune orbits are 10^7 and 1.6×10^8 years (Nakagawa et al., 1983, 1986). Since the typical timescale that the gas components in the disk dissipates is 10^7 years (Hayashi et al., 1985), Jovian and Neptune-like planets are difficult to form according to the standard model. Additional physical processes that promote forming planets are needed in order to solve the problem and improve the core accretion model. There are several suggestions about this, for example, the gravitational disk instability (Boss, 1997) and the pebble accretion process (Johansen & Lambrechts, 2017).

1.1.2 Review of Detection Methods

One of the difficulties of imaging exoplanets is that there are host stars much brighter than the nearby planets. The lights from the planets can come by reflecting the lights from the host stars mainly in optical or by their thermal radiations mainly in near-infrared (NIR). For Earth-sized planets around Sun-like stars, the brightness ratios between the hosts and planets are typically $\sim 10^{-10}$ in optical and $\sim 10^{-7}$ in NIR. The angular separation between the host star and planet is

$$\Delta\theta = \frac{a}{d} = 0.1 \left(\frac{a}{1\ \mathrm{au}}\right) \left(\frac{10\ \mathrm{pc}}{d}\right)\ \mathrm{arcsec}$$

where a is the semi-major axis of the planet and d is the distance from the observer to the planetary system. In order to image an Earth-like planet located at 10 pc, it requires removing the flux from the host star, which is 10^{10} times brighter than the planet and located at much smaller separation than the magnitude of the atmospheric seeing. Such a high requirement had prevented the discovery of exoplanetary systems for a long time. With the current-of-art, most hot and long-period exoplanets can be explored via direct imaging (Bowler, 2016). On the other hand, we can also indirectly detect the existence of exoplanets and characterize physical parameters for the planetary systems by

[2] Although solid components could settle toward their core after the planet formation.

observing some characteristics sculpted on the lights of the host star. There are several methods for detecting exoplanets and each method has different detection sensitivities for exoplanetary systems and different abilities for constraining physical parameters of the planetary systems. Here I briefly introduce several exoplanet detection methods and their uniqueness.

Radial Velocity (Doppler)

The radial velocity (Doppler) method (e.g. Butler et al., 2006) has been one of the most successful methods to detect exoplanetary system since it had succeeded to first discover an exoplanet around a main-sequence star (Mayor & Queloz, 1995). The radial velocity (hereafter RV) method measures the radial (line-of-sight) velocity of the stellar host by observing the Doppler shifts of the absorption lines of materials in the stellar atmosphere. If a host star has a companion (planet), the radial velocity will change over time because the companion causes the reflex motion of the host star due to the gravitational interactions. For a circular orbit, the semi-amplitude of RV signal K is given by

$$
\begin{aligned}
K &\equiv \left(\frac{2\pi G}{P(M_\star + M_P)^2}\right)^{1/3} M_P \sin i \\
&\approx \left(\frac{2\pi G}{P M_\star^2}\right)^{1/3} M_P \sin i \quad (\because M_P \ll M_\star) \\
&\approx 130\ \mathrm{m/s} \left(\frac{M_P \sin i}{M_{\mathrm{Jup}}}\right) \left(\frac{M_\star}{M_\odot}\right)^{-2/3} \left(\frac{a}{0.05\mathrm{au}}\right)^{-1/2} \quad \text{(For hot Jupiters)} \\
&\approx 0.1\ \mathrm{m/s} \left(\frac{M_P \sin i}{M_\oplus}\right) \left(\frac{M_\star}{M_\odot}\right)^{-2/3} \left(\frac{a}{1\mathrm{au}}\right)^{-1/2} \quad \text{(For Earth like planets)}
\end{aligned}
$$

where M_P is the mass of companion (planet), i is the orbital inclination, G is the gravitational constant, and $M_\star$ is the mass of the host star, a is the semi-major axis of the orbit, and P is the orbital period of the system. K and P is measurable from the RV variations and M_* can be estimated from the spectroscopic observation. Therefore, the RV method can provide the minimum mass of the companion $M_P \sin i$. The current observation limit for the RV is down to ~ 1 m/s (e.g. Trifonov et al., 2020) and it is not enough to detect Earth-like planets orbiting Sun-like stars. In a strategy targeting terrestrial planets in the habitable zones around M-dwarfs, the requirement of the precision will be loosen by one of an order of magnitude because both $M_\star$ and a become smaller by an order of magnitude.

Transit

If a planet transits in front of a host star, its eclipse can be observed as periodic dimming. Then, the line of sight between an observer and the host is aligned with the orbital plane of the planet, i.e. $i \sim \pi/2$, and its probability is scaled as

$$\begin{aligned} P_{\rm transit} &\approx 0.005 \left(\frac{1{\rm au}}{a}\right)\left(\frac{R_\star}{R_\odot}\right) \quad \text{(For Earth like planets)} \\ &\approx 0.08 \left(\frac{5\ {\rm days}}{P}\right)^{2/3}\left(\frac{R_\star}{R_\odot}\right)\left(\frac{M_\odot}{M_\star}\right)^{1/3} \quad \text{(For hot Jupiters)} \end{aligned}$$

assuming a random planetary orbit, where $R_\star$ is the radius of the host star. These transiting probabilities indicate that 0.5% of Earth-like planets and 8% of hot Jupiters are observable by their transiting signals if we have sufficient sensitivity. From the transiting light curves, we can extract the transiting depth as

$$\begin{aligned} \delta_{\rm depth} = \frac{\Delta F}{F} \approx \left(\frac{R_P}{R_\star}\right)^2 &\approx 0.01 \left(\frac{R_P}{R_{\rm Jup}}\right)^2\left(\frac{R_\star}{R_\odot}\right)^2 \\ &\approx 8\times 10^{-5} \left(\frac{R_P}{R_\oplus}\right)^2\left(\frac{R_\star}{R_\odot}\right)^2 \end{aligned}$$

where P is the orbital period and R_P is the radius of the companion. The transiting planets can be discovered by monitoring many stars with sufficient photometric precision. Jupiter-size transiting signals are well detectable (observable) with ground-based telescopes, but for smaller-size planets, it requires space-based observations to accomplish high photometric accuracy. The transit method can detect short-period planets around high-temperature stars like A-type stars that are difficult to observe by the RV method due to the shortage of absorption lines. It also enables estimating the inclination angle of the planetary orbit i and then determining the planetary mass M_P by combining it with the RV method.

Astrometry

Astrometry method measures the reflex motions of host stars in the sky plane and then detect the companions. Considering the two-body problem of a host star and a companion, the astrometric shift of the host during its orbit around the barycenter of the system is given as

$$\theta_{\rm shift} \approx 3\times 10^{-5}\left(\frac{M_P}{M_{\rm Jup}}\right)\left(\frac{M_\star}{M_\odot}\right)^{-1}\left(\frac{a}{3{\rm au}}\right)\left(\frac{d}{100{\rm pc}}\right)^{-1} \quad \text{arcseconds.}$$

The astrometry method is more sensitive to planets with longer orbital periods. Most ground-based telescopes cannot achieve such high precisions for the planetary astrometric signals due to the seeing limit. *Gaia* mission (Lindegren et al., 2020), whose telescope was launched in 2013 by European Space Agency, has been monitoring ~ 10 billion stars in all sky areas and measuring their positions and proper motions with very high astrometric accuracy, e.g. $\sigma_{\theta_{\rm shift}} \sim 0.02$ mas at $G = 15$ mag and $\sigma_{\theta_{\rm shift}} \sim 0.2$ mas at $G = 20$ mag. *Gaia* is expected to detect ~ 1000 exoplanets via the astrometry method.

Microlensing

Gravitational microlensing is an astronomical phenomena predicted from the general theory of relativity (Einstein, 1936). According to the theory, the light emitted from a background source star will be bent by the gravity of a foreground object when the light passes through near the object. The foreground object acts like a lens and splits the light of the source into two images. Even if the two images cannot be resolved, these images are also magnified. The relative proper motion between the source and lens leads to changing the alignment, resulting in time-variable flux of the source. If the lens has a planetary companion near the two images, the planet also acts like a lens and then perturbs the images, resulting in short-timescale anomalous features on the light curves. Typical timescales of the planetary signals are a few days for Jupiter-mass planets and a few hours for Earth-mass planets. By identifying the short planetary perturbations in microlensing events, one can detect planets orbiting the lenses. I will review in Section 1.3 and explain details on the microlensing method in Chapter 2.

Direct Imaging

Direct imaging method is directly observing the light from the planet by separating it from the light from the host. As mentioned above, this is generally difficult because the flux ratio between the host and planet is extremely large by $\sim 10^7 - 10^{10}$. In order to suppress such an extremely high flux ratio, the observation is carried out by using a method of blocking the host star light (coronagraph), a method of superimposing light of opposite phase only on the host star and attenuating only the host star light (null interferometer), with a method of adjusting atmospheric fluctuations and equipment's aberrations that makes it easier to separate the lights from the host and planet (Adaptive Optics, AO).

In current observations, relatively young and high-temperature gas-giant planets have been mainly discovered by the direct imaging method. This is because they are bright by their thermal emissions in NIR and the contrast is less extreme than that in optical. In order to detect the reflected light from planets by direct imaging, space-based observations are more optimal because of less noise (e.g. thermal emissions and/or sky background) and no atmospheric fluctuations.

1.1.3 Exoplanet Demographics

Since the first exoplanet was discovered around the star 51 Pegasi (Mayor & Queloz, 1995), more than 4,200 exoplanets have been discovered so far (2020/11/26). Figure 1.2 represents the distributions of the exoplanets discovered to date. From this figure, we can see that the exoplanet demographic is considerably diverse and different from planets in the solar system. For example, 51 Pegasi b (Mayor & Queloz, 1995) is a Jupiter-mass planet that orbits within 0.1 au around a main-sequence star. It should be noted that the sample of exoplanets plotted in Figure 1.2 is suffered from observation biases in each observation method. Because most of the exoplanets discovered so far are composed of that discovered by the RV and transit methods, the distribution is considered to be biased towards ones

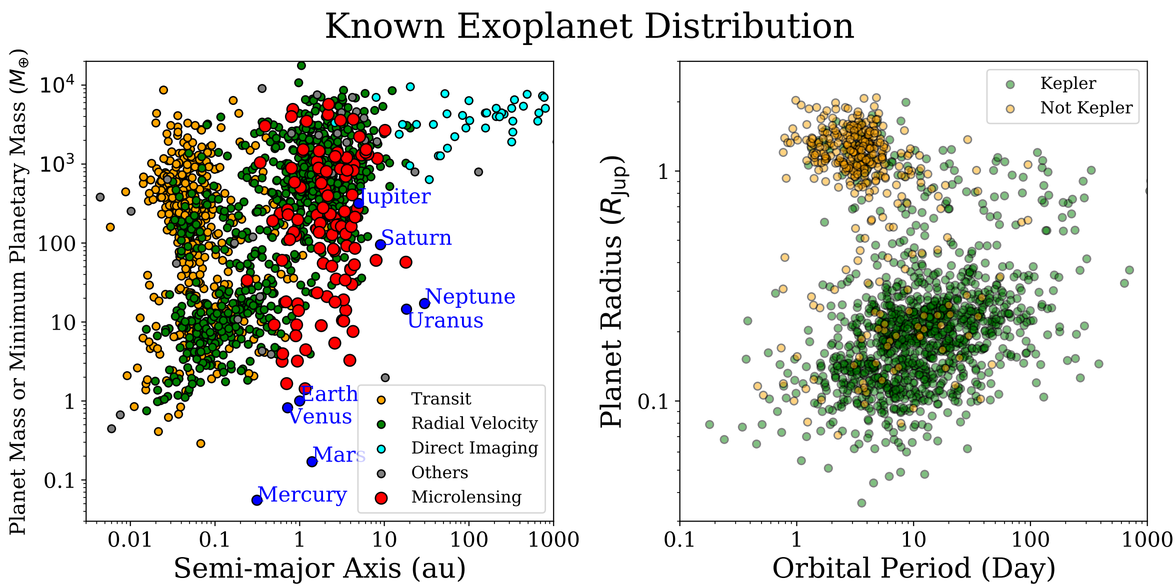

Figure 1.2 The two panels present the distributions of the exoplanets discovered to date, which is cited from the NASA Exoplanet Archive (Akeson et al., 2013). In the left panel, each exoplanet plot is colored by discovered methods, transit (orange), RV (green), direct imaging (cyan), microlensing (red), and others (gray). I also plot planets in our solar system as blue points. In the right panel, each exoplanet plot is colored by whether the planets are detected by *Kepler* (including *K2*) mission or not.

with short semi-major axes and large masses. Understanding such observational biases is difficult but important to reveal the "true" exoplanet distribution.

There have been many exoplanet survey missions using different methods so far. In the early phase, most exoplanets have been discovered by the RV method and it enabled them to conduct the statistical analysis of close-in exoplanets (Santos et al., 2001; Cumming et al., 2008; Howard et al., 2010; Johnson et al., 2010; Mayor et al., 2011). Later, NASA's *Kepler* mission (2009-2013) (Koch et al., 2010) was successful in discovering thousands of transiting small-size exoplanets (see the right panel of Figure 1.2), and it revealed that a large fraction of main-sequence stars have relatively compact planetary systems composed of super-Earth and/or sub-Neptune planets (e.g. Howard et al., 2012; Zhu et al., 2018). The statistical results obtained from the RV and transit planet sample are summarised in several review papers (e.g. Gaudi et al., 2020).

1.2 Brown Dwarfs

Brown dwarf (BD) is an intermediate-mass (∼13-80 Jupiter-mass) object between a planet and a star. Because these are not as massive as stars, the hydrogen fusion reactions do not occur in their body, but deuterium fusion reactions do, and it emits thermal radiations caused by gravitational contraction. The temperature of BDs decreases with their ages due to radiative cooling after deuterium burning had finished and is generally lower than that of typical M-dwarf stars (~ 3000 K).

Field Brown Dwarfs

Most theories suppose that field BDs form via the direct collapse of molecular clouds on a much smaller scale than stars, and promoted by turbulent fragmentation (Luhman, 2012). These theories are supported observationally, for example, some young BDs are observed with excess emission from the surrounding raw material disks (Apai et al., 2005; Luhman et al., 2005). Moreover, André et al. (2012) found self-gravitating dense clumps of gases and dust with mass $0.015 - 0.03\ M_\odot$, which are similar to those of low-mass BDs.

Survey observations for BDs had been conducted since the 1980s, but it was difficult to find by direct imaging due to its low temperatures and faintness. In the 1990s, the survey had been targeting relatively young and hot (high-temperature) brown dwarfs in young clusters like the Pleiades (see Festin, 1998). In 1995, scientists first clearly identified a brown dwarf around an M-dwarf by direct imaging using a coronagraph[3] (Nakajima et al., 1995). In the same year, a field brown dwarf was first discovered in the young cluster of the Pleiades (Rebolo et al., 1995). Recently, infrared all-sky survey have been conducted by several groups (e.g. DENIS Epchtein et al., 1997; 2MASS Skrutskie et al., 2006; VISTA Emerson & Sutherland, 2010), and many BDs (and candidates) have been discovered. One of the motivations for detecting BDs was to solve the problem of the Universe's missing mass. However, survey results found that the mass densities of brown dwarfs cannot be a major part of the dark matter (e.g. Chabrier et al., 1996).

Brown Dwarfs as Companions

The definition of BDs to distinguish them from planets is still unclear. One definition is having larger masses than a mass boundary of $\sim 13\ M_{\rm Jup}$ where deuterium burning starts. However, deuterium burning can be coupled to models of planet formation (e.g., Mollière & Mordasini, 2012) and the planetary mass formed by the core accretion process is potentially up to $\sim 30\ M_{\rm Jup}$ (Tanigawa & Tanaka, 2016). Another definition is the difference in the formation process, i.e., ones that are formed in the protoplanetary disks are planets, and others that are formed via the direct collapse of molecular clouds are brown dwarfs. However, this definition also contains incompleteness because we generally do not know how objects formed in past. The former definition is typically applied although the mass is not directly obtained as an observable quantity.

Early radial velocity surveys revealed the general absence of close-in ($a < 5$ au) BD companions to solar-type stars. Grether & Lineweaver (2006) found that $\sim 16\%$ of solar-type stars have a companion within $P < 5$yr with masses of $M_P \geq 1\ M_{\rm Jup}$, but BD companions are less than 1%. This paucity is referred to as the *brown dwarf desert*. The

[3] A possible candidate GD 165 B was discovered before 1995 but it had not been recognized as a brown dwarf (Zuckerman & Becklin, 1987).

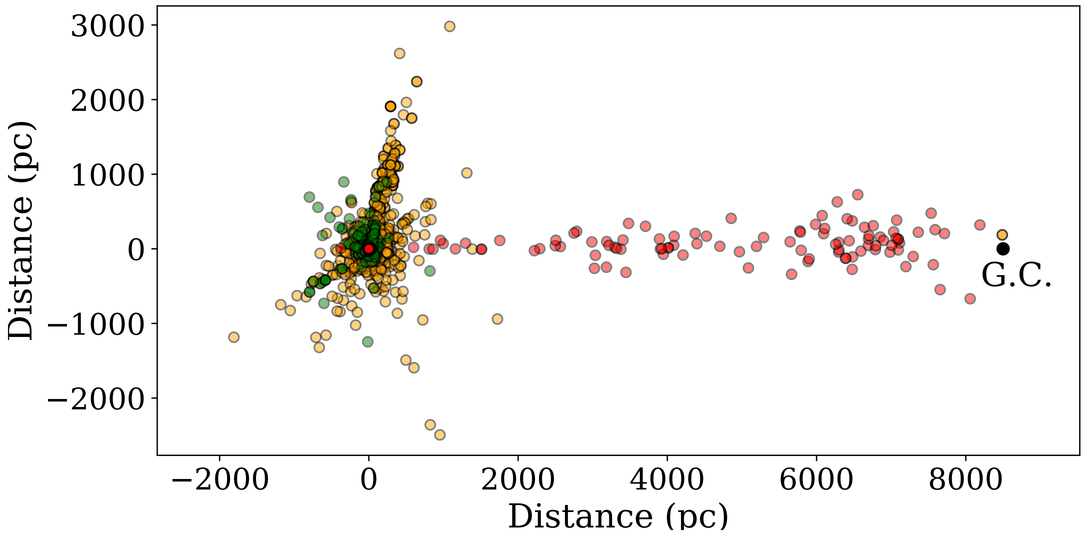

Figure 1.3 The face-on view of the Galactic distribution of discovered exoplanets seen from the Galactic pole, where the planets are colored by the discovered method; transit (orange), RV (green), microlensing (red), and other methods (gray). The black point indicates the location of the Galactic center and the origin is set on the location of the Sun.

mechanisms to form the desert have been thought to be attributed to several scenarios. One scenario is the inward migration of close-in brown dwarfs in protoplanetary disks around host stars, which causes the destruction of the close-in BDs via mergers with host stars. It is reported that the most effective mass of protoplanetary disks to lead BD companions to migrate inward is that around solar-type stars (Armitage & Bonnell, 2002). Another scenario suggests that the desert might reflect on different formation mechanisms for two populations of planets and stars (Matzner & Levin, 2005). There still debate about this.

1.3 Microlensing Results

Microlensing is the only method that is sensitive to planets with the Earth masses beyond the snow line and the planet sample discovered by microlensing is complementary to that discovered by other methods (Gould & Welch, 1996). I briefly summarize the characteristics of microlensing compared to other methods.

- Microlensing does not depend on the luminosity of the host star and thus it can detect planets around low-mass stars, brown dwarfs, and even planets (i.e. exomoons). This characteristic is important to understand planet distributions around dark low-mass objects.

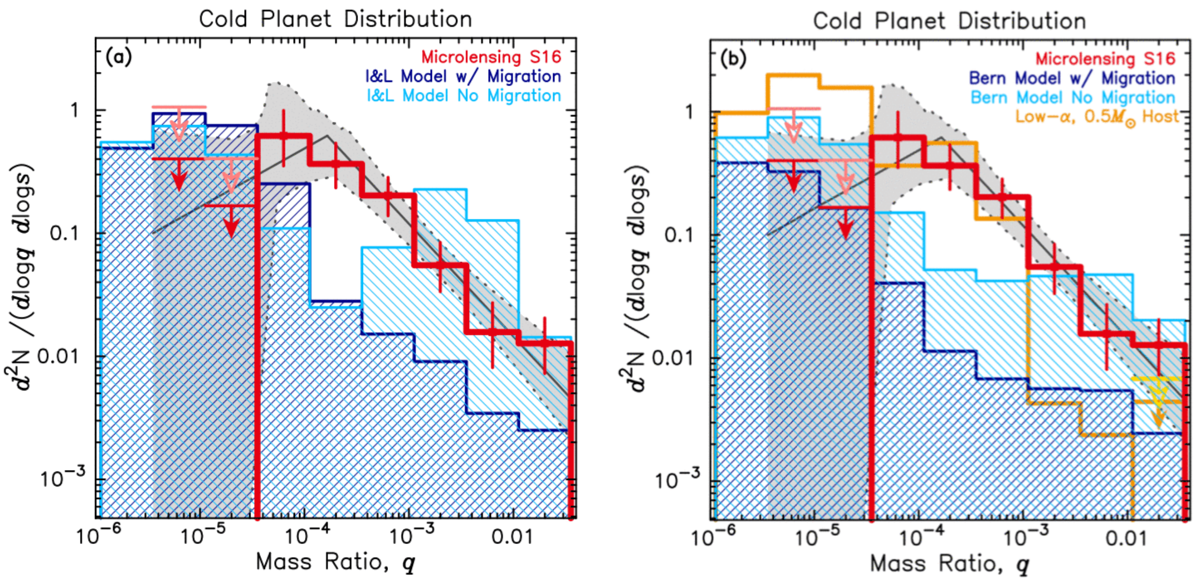

Figure 1.4 A comparison between the observational result obtained from Suzuki et al. (2016) and two simulated planet populations based on the core accretion theory derived from two groups (Ida & Lin, 2004; Mordasini et al., 2009). The red histogram is the mass-ratio distribution from Suzuki et al. (2016). The dark and light blue histograms are the simulated planet populations with and without considering planetary migration, respectively.

- Microlensing can detect wide-orbit planets with masses down to the sub-Earth-mass and with orbital distances of a few au. The RV method can also probe such parameter spaces of planets but it requires long-term observations.

- Microlensing can discover planetary systems far from our solar system distant by $1-8$kpc (see Figure 1.3), which offers a way to probe the planet distributions throughout from our solar system to the Galactic center (e.g. Penny et al., 2016).

- Microlensing can detect dark planetary-mass objects even without host stars, e.g. free floating planets and even primordial black holes (Sumi et al., 2011; Mróz et al., 2017; Niikura et al., 2019; Johnson et al., 2020).

One of the problems of microlensing is that the number of microlensing planets is small. In the early phase of searching microlensing exoplanets,it had been needed to combine the survey observations by large telescopes and follow-up observations by small telescopes in order to observe the short-term planetary signals (Gould & Loeb, 1992). Recent developments of microlensing survey obsevervation groups such as MOA (Bond et al., 2001; Sumi et al., 2003), OGLE (Udalski et al., 1994), and KMTNet (Kim et al., 2016), enabled us to detect microlensing exoplanets by only their survey data and significantly increase the detection rate these days. Here I review several statistical results of microlensing.

- Gould et al. (2010) used a sample of 13 statistically-unbiased high-magnification microlensing events and found a planet frequency distribution

$$\frac{d^2 N_P}{\mathrm{d}\log q\ \mathrm{d}\log s} = (0.36 \pm 0.15)\ \mathrm{dex}^2$$

  at the planet/host mass ratio $q = 5.0 \times 10^{-4}$ with no clear deviation from a flat distribution in log-projected separation s. The host stars for the sample have a typical mass $M_{\rm Host} \sim 0.5\ M_\odot$ and the sample is sensitive to planets with the projected separations $s \sim 1$ that approximately correspond to three times the snow line. The planet frequency is approximately 7 times larger than that derived from the RV methods at small orbital-separation (Cumming et al., 2008) although it is consistent with the extrapolation of the RV result with observed solve in orbital separation.

- Sumi et al. (2010) used a sample of 10 microlensing planets known at the time and derived the relative planet frequency function beyond the snow line, assuming a simple scale of the detection efficiency with q, as $dN/dq \propto q^{-1.68\pm0.20}$. They argued that cold Neptunes and/or Super-Earths are 7^{+6}_{-3} times more common than cold Jupiters.

- Cassan et al. (2012) conducted a statistical analysis using 43 microlensing events gathered from six years of their microlensing survey and derived a power-law mass function for the planet frequency[4]

$$\frac{d^2 N_P}{\mathrm{d}\log M_P\ \mathrm{d}\log a} = 10^{-0.62\pm0.22}\left(\frac{M_P}{M_{\rm Saturn}}\right)^{-0.73\pm0.17}.$$

  They estimated that there are $1.6^{+0.72}_{-0.89}$ planets per star in the ranges of $0.5 < a < 10$ au and $5M_\oplus < M_P < 10M_{\rm Jup}$.

- Suzuki et al. (2016) conducted a statistical analysis of planetary events discovered in MOA-II microlensing survey observation from 2007 to 2012. They found that the detection-efficiency-corrected distribution of microlensing planets cannot be modeled by a single power-law in q and derived a broken power-law function for planet frequency

$$\frac{\mathrm{d}^2 N_P}{\mathrm{d}\log q\ \mathrm{d}\log s} = (0.61^{+0.16}_{-0.21})\left(\frac{q}{q_{\rm br}}\right)^n s^{0.49^{+0.49}_{-0.47}}\ \ \mathrm{dex}^{-2} \tag{1.1}$$

  where $q_{\rm br} = 1.7 \times 10^{-4}$ is the break position in the $\log q$ power-law function and $n = -0.93 \pm 0.13$ for $q > q_{\rm br}$ and $n = 0.6^{+0.5}_{-0.4}$ for $q < q_{\rm br}$. They suggested that cold Neptunes are likely to be the most common beyond the snow line. Later, the break in the power-law function was confirmed in several papers (Udalski et al., 2018; Jung et al., 2019) although the position of the break is not determined well.

[4]They derived the planetary mass M_P and the semi-major axis a by an Bayesian analysis with a Galactic model using the observed q and s. In general, Bayesian analysis conducted in microlensing does not consider the dependencies of planet frequency on the host properties like their masses and distances.

According to the standard core accretion model, it is predicted that the most abundant planets beyond the snow line would be planets with masses of $\sim$ a few $10M_{\oplus}$ (e.g. Ida & Lin, 2004). The mass-ratio function derived by Suzuki et al. (2016) is consistent with that prediction. However, the core accretion model also predicts a process causing a deficit of planets with masses of a range of $20-80M_{\oplus}$, which is called "runaway gas accretion process" (Lissauer, 1993; Pollack et al., 1996). In the process, a $\sim 10M_{\oplus}$ mass planetary core will enter a runaway growth phase once the accumulated H/He gas reaches to equal to the core mass. During this phase, the planets are unlikely to stop growing to reach Saturn or Jupiter masses. Ida & Lin (2004) predicted a exoplanet desert at masses between $10-100M_{\oplus}$ using a planetary population synthesis model based on the core accretion theory. Figure 1.4 represents a comparison between the observational result obtained from Suzuki et al. (2016) and some simulated planet populations based on the core accretion theory (Suzuki et al., 2018). The comparison shows that the theory underpredicts the number of Jovian-mass planets between $10^{-4}<q<10^{-3}$ by a factor of a few tens. It is reported in several papers that the runaway accretion process seems to be very significant only in 1-D calculations and simulations (e.g. Szulágyi et al., 2014). Such differences between the observational results and theoretical predictions would constrain and refine planetary formation theories.

1.4 Motivation and Introduction to Research

Observational exploration of the exoplanet distribution has important implications for the theory of planet formation. The distribution of short-period planets close to their host stars has been revealed in detail mainly by the transit and RV methods. On the other hand, the distribution of long-period and small planets remains largely unexplored (see Figure 1.2). The gravitational microlensing method is the only method that is sensitive to small planets beyond the snow line which is an important place to test for the core accretion theory.

High-mass objects such as gas giant planets and their brown dwarf companions are predicted to have significant impacts on the environment of their planetary systems through their gravitational effects and their orbital evolution. For example, they can play an important role in the formation of terrestrial planets in the habitable zone (Batygin & Brown, 2010; O'Brien et al., 2018; Childs et al., 2019). It is important to understand the distribution of the high-mass objects, which can have a significant impact on the evolution of planetary systems. Exploring the distribution of the intermediate-mass objects between planetary and sub-stellar masses will also help us to understand if there are differences in their formation processes (Swastik et al., 2020). In this regard, observational determination of physical properties for planetary systems including their masses and orbital separations is needed.

The determination of the physical properties is one of the most important issues in the field of microlensing. In general, the physical properties of systems discovered by microlensing cannot be determined, but only their probability distributions can be obtained

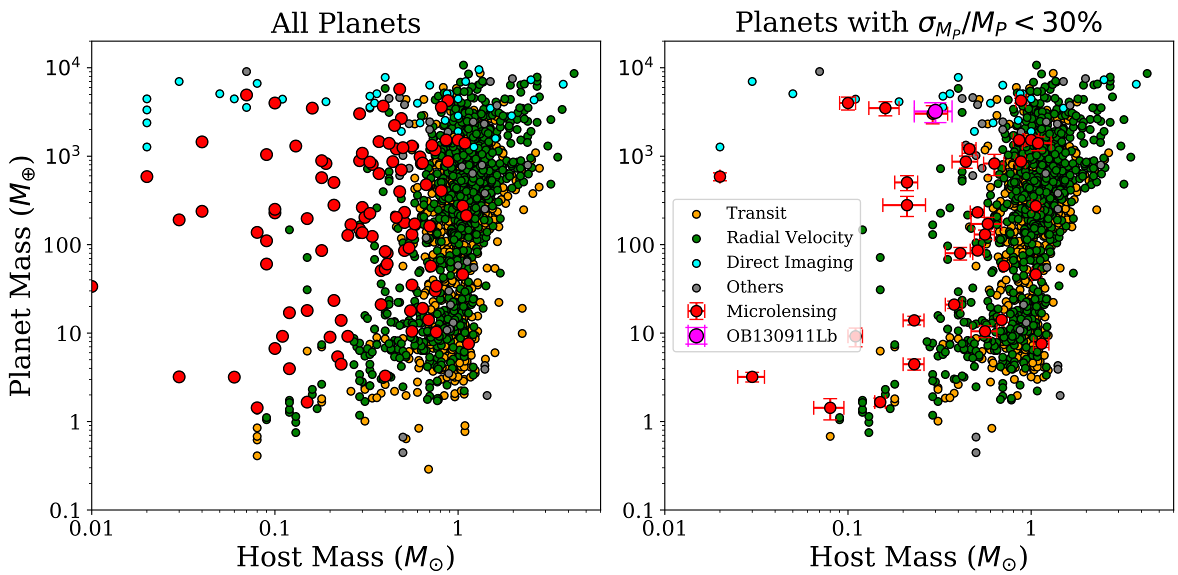

Figure 1.5 The left panel shows the distribution of exoplanets discovered to date, along the axes of the mass of the host star and the planet mass. The right panel is the same but only plotted with planets whose masses are measured with an accuracy of less than 30%. The number of discovered microlensing exoplanets is over 100 but the percentage of the number with measured masses is less than 40%.

by Bayesian estimation assuming a Galactic model of star population (e.g., Beaulieu et al., 2006). Such Bayesian estimation is likely to create bias in statistical discussions to some extent because the results strongly depend on the prior probabilities assumed and the uncertainties are typically large. For some microlensing events, it is possible to uniquely determine the physical properties by performing a detailed analysis that includes high-order effects (see next chapter). However, in most events, it has been difficult to detect the high-order effects due to the lack of S/N and/or to the characteristics of the events (see Figure 1.5). It is important to deepen the knowledge of modeling including high-order effects because the detailed analysis including them is expected to be more powerful in the future when the data becomes more accurate.

High-order effects can allow us to explore planetary systems with parameter spaces that have not been explored before. In this thesis, I focus on a high-order microlensing effect, xallarap (Han & Gould, 1997; Griest & Safizadeh, 1998a; Poindexter et al., 2005). The xallarap effect has been investigated in previous detailed analysises of microlensing events, but it had not been detected significantly (e.g., Sumi et al., 2010; Furusawa et al., 2013). In Chapter 3, I find a significant xallarap effect in a planetary microlensing event and identify a companion orbiting the microlensed source star from the xallarap signal. This is the first detection of source companion via xallarap. Stimulated on this discovery, in Chapter 4, I describe an analysis that extends and develops the detection method using xallarap. Finally, I propose a method to explore short-period exoplanets in the Galactic bulge using the xallarap effect with the Nancy Grace Roman Space telescope (Spergel et al., 2015; Penny et al., 2019; Johnson et al., 2020).

Chapter 2

Gravitational Microlensing

According to the theory of general relativity, the space near an object having mass is distorted and the gravity acts like a convex lens with respect to the lights of background stars. This phenomenon is called gravitational lensing. Gravitational lensing can be observed by images of quasars and galaxies in the background distorted or split by the gravity of galaxies and clusters of galaxies in the foreground. On the scale of lens mass of stars and planets, it is difficult to resolve the images because of the small angular separations of an order of micro-degree. However, gravitational lensing has a characteristic that magnifies each image and then raises the total fluxes from each image. We can observe the micro-scale gravitational lensing (microlensing) by stellar-mass and planetary-mass lens objects by observing the magnified fluxes of background objects.

In this chapter, I will describe a typical microlensing phenomenon, and high-order microlensing effects that are important to estimating physical quantities of the lens and microlensed source.

2.1 Basic Theory

2.1.1 Single Lens Microlensing

First, I consider a case that a point source is microlensed by a point-mass lens. Figure 2.1 represents a schematic view of a typical microlensing phenomenon. Here D_S and D_L are the distance of the source and lens from the observer, respectively. Light is emitted from a source star and the path of the light ray is bent by a small angle δ by the weak gravitational field of the lens. The observer would observe two images of the source. Let $r_1(\equiv r_0 + r)$ and r_2 be the distances between the images of the source projected on the "lens plane" and the lens, respectively. Here r_0 is an impact parameter between the source and lens on the lens plane. When $r_i \ll D_L, D_S$ (i.e. $\alpha, \beta \ll 1$),

$$D_L\alpha = r,\ D_S\beta = r_0. \tag{2.1}$$

And then the following equation is geometrically obtained as

$$D_S\alpha = (D_S - D_L)\delta. \tag{2.2}$$

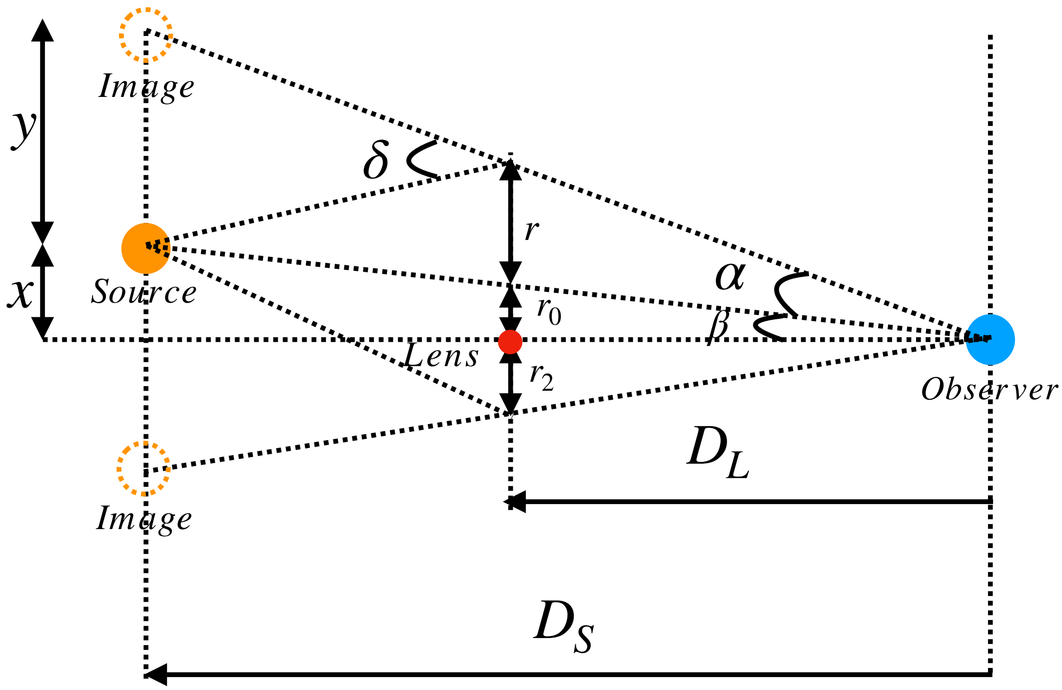

Figure 2.1 A schematic view of a microlensing event.

According to the theory of general relativity with weak-field equations[1], a light ray passing near a spherically symmetric body with a Schwartzschild radius R_s would be bent from its original path towards the direction of the mass (lens) by an angle

$$\delta(r_0, M_L) = \frac{2R_s(M_L)}{r + r_0} = \frac{4GM_L}{c^2(r + r_0)}. \tag{2.3}$$

Here M_L is the mass of the lens. Combining this with Equation (2.2), the follow equation is derived as

$$\begin{aligned} D_S\frac{r}{D_L} &= (D_S - D_L)\frac{4GM_L}{c^2 r_1} \\ \Leftrightarrow r^2 &= D_L\left(1 - \frac{D_L}{D_S}\right)\frac{4GM_L}{c^2 r_1}r. \end{aligned} \tag{2.4}$$

where $r_1 = r + r_0$. This is called the lens equation.

Now, let's substitute $r_0 = 0$ into Equation (2.4), i.e. consider a situation that the source, lens, and observer are perfectly aligned. Then, we obtain

$$r = \sqrt{\frac{4GM_L D_L}{c^2}(1 - \frac{D_L}{D_S})}, \tag{2.5}$$

[1]Typical objects like star and planets have much weaker gravitational fields than very dense objects like neutron stars and black holes. The weak-field equations are valid much outside of R_s whose value for the Sun is only ~ 3 km.

which means $r = const$ and the source image will be observed as a ring surrounding the lens. This ring image is called "Einstein ring", and its radius $R_{\rm E}$ and angular radius $\theta_{\rm E}$ are

$$\begin{aligned} R_{\rm E} &= \sqrt{\frac{4GM_L D_L}{c^2}(1 - \frac{D_L}{D_S})} \\ &\simeq 2.3 \text{ au} \left(\frac{M_L}{0.3\ M_\odot}\right)^{1/2} \left(\frac{D_S}{8 \text{ kpc}}\right)^{1/2} \left(\frac{x(1-x)}{0.25}\right)^{1/2}, \end{aligned} \tag{2.6}$$

$$\begin{aligned} \theta_{\rm E} &= R_{\rm E}/D_L \\ &\simeq 320\ \mu\text{as} \left(\frac{M_L}{0.3\ M_\odot}\right)^{1/2} \left(\frac{D_S}{8 \text{ kpc}}\right)^{1/2} \left(\frac{1 - x/0.75}{x/0.75}\right)^{1/2} \end{aligned} \tag{2.7}$$

where $x = D_L/D_S$.

For $r_0 \neq 0$, the lens equation (2.4) can be described using $R_{\rm E}$ as a simple quadratic equation

$$r^2 - r_0 r - R_{\rm E}^2 = 0. \tag{2.8}$$

This can be easily into two solutions as

$$y_\pm = \frac{u \pm \sqrt{u^2 + 4}}{2} \tag{2.9}$$

where $u = r_0/R_{\rm E}$ and $y = r/R_{\rm E}$ are the positions of the source and images on the lens plane in units of $R_{\rm E}$, respectively. Because $|y_-| < 1 < |y_+|$, this means that there are an image in the Einstein radius and another image outside the Einstein radius opposite of the source. For a typical microlensing event with $0 < u < 1$, the angular separation between these images is an order of magnitude of $2\theta_{\rm E}$ because $0 < u < 1 \Leftrightarrow 2 < |y_+| + |y_-| < \sqrt{5}$. This is a reason why this phenomenon is called microlensing. Most of the current ground-based optical and infrared telescopes can not have the ability to resolve these images[2].

Magnification

Here I consider the changes in the total flux of the source images. The two source images contribute to the total amounts of the magnified fluxes, which is proportional to their solid angle of each magnified image. Because the surface brightness of each image is preserved, the flux of each image is proportional to the rate of magnification of each image. However, note that stars have non-constant surface brightness with their stellar limb darkening. So,

[2]Recently, Dong et al. (2019) have succeeded to precisely and directly measure the image separation of a microlensed source $\theta = 3.78 \pm 0.05$ mas using an infrared interferometer, Very Large Telescope Interferometer (VLTI) GRAVITY, and then precisely estimated the angular Einstein radius $\theta_{\rm E} = 1.87 \pm 0.03$ mas.

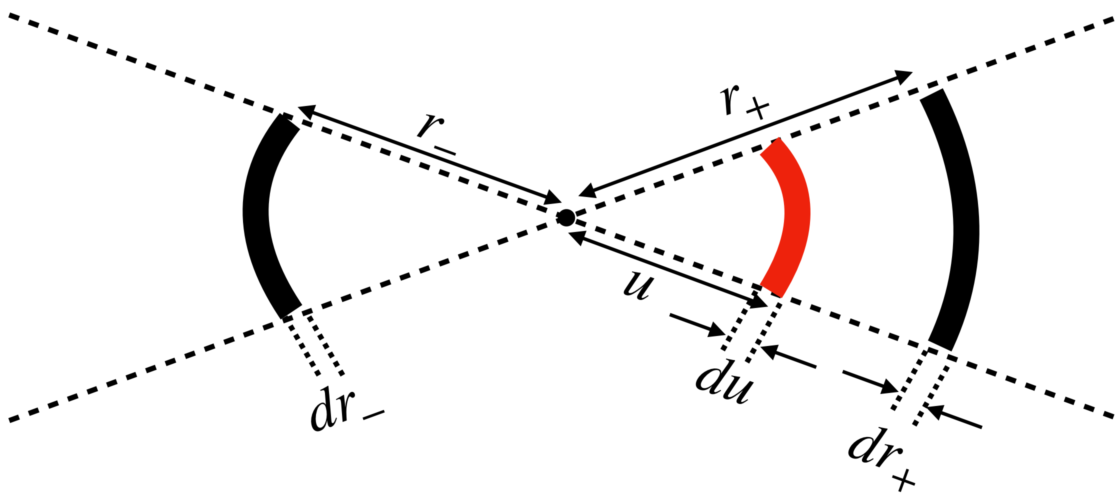

Figure 2.2 A schematic view for the magnification of a small area of the source in polar coordinate. The red arc area represents a area of the source. The two black arc areas represent the image of the magnified source.

in light curve modeling, each area of the source surface should be weighted by its limb darkening coefficient.

The magnification of the source flux A is defined by the ratio of the source flux to that is not microlensed. Here, to calculate A, I consider a polar coordinate and that the source have a small solid angle of $d\Omega$. Figure 2.2 shows a schematic view for the magnification of a small area of the source in polar coordinate. From this figure, the magnification A can be described by

$$
\begin{aligned}
A(u) &= \frac{d\Omega_+ + d\Omega_-}{d\Omega} \\
&= \left|\frac{r_+ d\theta dr_+}{u d\theta du}\right| + \left|\frac{r_- d\theta dr_-}{u d\theta du}\right| \\
&= \frac{u^2+2}{u\sqrt{u^2+4}} \simeq \frac{1}{u} \quad (u \ll 1)
\end{aligned}
\tag{2.10}
$$

From Equation (2.10), the magnification A is approximately inversely proportional to the impact parameter u and $u \to \infty \Leftrightarrow A \to 1$ and $u \to 0 \Leftrightarrow A \to \infty$. However, note that in principle the magnification will not reach infinity because the source stars have their finite source sizes and are not point sources.

In general, because the lens and source have relative velocities, the magnification changes with time. Here, I consider a relative proper motion of the source to the lens on the lens plane $\boldsymbol{\mu}_{\rm rel}$ ($\equiv \boldsymbol{v}/R_E$) where $\boldsymbol{v}$ is the transverse velocity between the source and

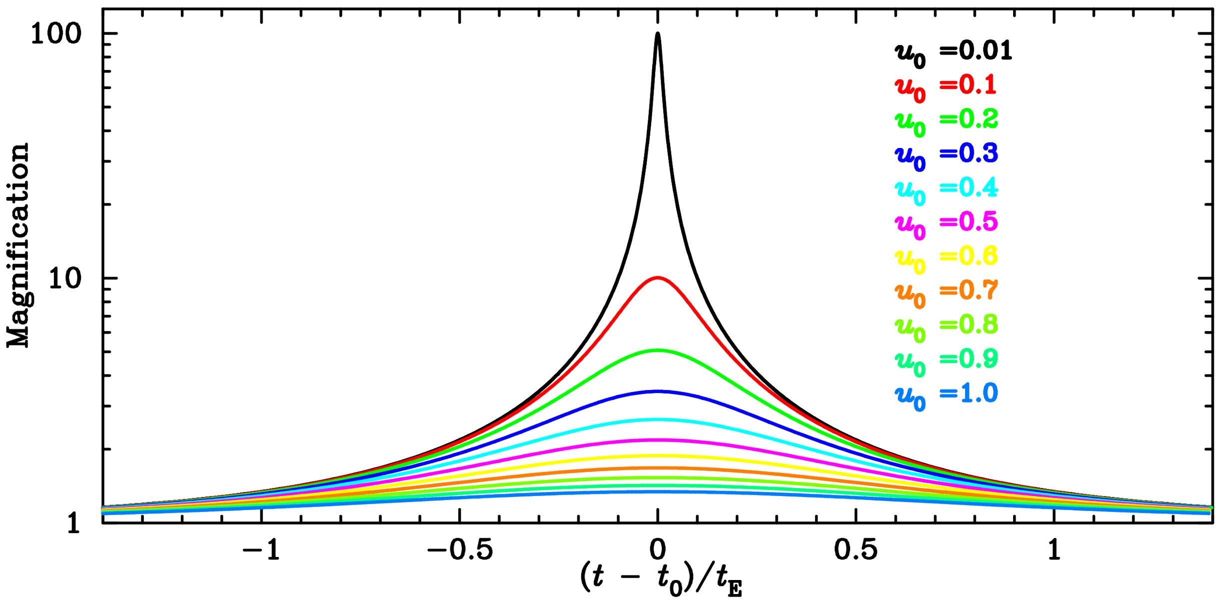

Figure 2.3 Theoretical microlensing light curves of the single-lens with different u_0.

lens relative to the observer-source line of sight. The impact parameter $u(t)$ is written by

$$\begin{aligned} u(t) &= \sqrt{u_0^2 + (\mu_{\rm rel}(t-t_0))^2} \\ &= \sqrt{u_0^2 + \left(\frac{t-t_0}{t_{\rm E}}\right)^2}, \end{aligned} \tag{2.11}$$

where u_0 is the minimum impact parameter between the source and lens, t_0 is the closest time. $t_{\rm E}$ is the characteristic timescale of a microlensing event and is defined as the time taken for the source to pass the Einstein radius and is described by

$$\begin{aligned} t_{\rm E} &= \frac{\theta_{\rm E}}{\mu_{\rm rel}} = \sqrt{\frac{4GM_L}{c^2} D_S x(1-x)} \\ &\simeq 22\ {\rm days} \left(\frac{M_L}{0.5M_\odot}\right)^{\frac{1}{2}} \left(\frac{D_S}{8\ {\rm kpc}}\right)^{\frac{1}{2}} \left(\frac{x(1-x)}{0.2}\right)^{\frac{1}{2}} \left(\frac{v}{200\ {\rm kms}^{-1}}\right)^{-1}. \end{aligned} \tag{2.12}$$

Substituting $u(t)$ into Equation (2.10), one obtains

$$A(t) = \frac{u_0^2 + \left(\frac{t-t_0}{t_{\rm E}}\right)^2 + 2}{\sqrt{u_0^2 + \left(\frac{t-t_0}{t_{\rm E}}\right)^2}\sqrt{u_0^2 + \left(\frac{t-t_0}{t_{\rm E}}\right)^2 + 4}} \tag{2.13}$$

The magnification pattern for the simplest single-lens model will draw a symmetrical light curve centered on t_0, and the smaller the minimum impact parameter u_0, the larger the maximum magnification (see Figure 2.3). When we model a microlensing light curve by the sinle-lens model, we will obtain the parameters like u_0, t_0, and $t_{\rm E}$ but not be able to directly determine physical parameters of the lens like M_L, and D_L because such physical parameters are degenerate in $t_{\rm E}$.

Binary Source (1L2S) Microlensing

Consider that two source objects in the same system are microlensed by single lens object. Such an event is often called "binary source (1L2S) event". The magnification for the binary source event is written as follows,

$$A(t) = \frac{A_1(t)F_{S,1} + A_2(t)F_{S,2}}{F_{S,1} + F_{S,2}} = \frac{A_1(t) + q_F A_2(t)}{1 + q_F}, \tag{2.14}$$

where $F_{S,i}$ and A_i are the baseline (un-microlensed) flux and the magnification for the ith sources, respectively, and q_F ($\equiv F_{S,2}/F_{S,1}$) is the flux ratio between the sources. For this event, the observed fluxes are composed of a superposition of each source flux, and then the color is changing over time. This is because the flux ratio between sources changes as the magnifications of each source independently changes over time. Note that the values of q_F differ by different pass-bands. Strictly speaking, the relative velocities of each source to the lens are different and thus $t_{\rm E}$ should be different for each source but for most cases its effect can be ignored. The features of the light curve for binary source events are sometimes degenerate with those for binary-lens events. It is worth examining which models are statistically plausible for the light curve features.

2.1.2 Binary Lens (2L1S) and Multiple Lens Microlensing

For the symmetric problem of the single-lens model, the deflection of the light ray can be considered as a 1-D problem. Since the symmetry is broken by increasing the number of lenses, it requires using 2-D vectors. Consider that the light emitted from the source at the position $\boldsymbol{\eta}$ in the source plane passes through the position $\boldsymbol{\xi}$ on the lens plane and reaches the observer (see Figure 2.4). When the light is bent on the lens plane by the angle $\boldsymbol{\delta}$,

$$\boldsymbol{\eta} = \frac{D_S}{D_L}\boldsymbol{\xi} - (D_S - D_L)\boldsymbol{\delta}. \tag{2.15}$$

Because $|\boldsymbol{\delta}(r)| = 4GM/(c^2 r)$,

$$\frac{D_L}{D_S}\boldsymbol{\eta} \;=\; \boldsymbol{\xi} - \frac{4GM}{c^2}\frac{D_L}{D_S}(D_S - D_L)\frac{\boldsymbol{\xi}}{|\boldsymbol{\xi}|^2}.$$

We can normalize this equation by the Einstein radius $R_{\rm E} = \sqrt{\frac{4GM}{c^2} D_S x(1-x)}$, and then

$$\begin{aligned} x\frac{\boldsymbol{\eta}}{R_{\rm E}} &= \frac{\boldsymbol{\xi}}{R_{\rm E}} - R_{\rm E}\frac{\boldsymbol{\xi}}{|\boldsymbol{\xi}|^2} \\ \boldsymbol{u} &= \boldsymbol{y} - \frac{\boldsymbol{y}}{|\boldsymbol{y}|^2}, \quad (\boldsymbol{u} = x\frac{\boldsymbol{\eta}}{R_{\rm E}},\ \boldsymbol{y} = \frac{\boldsymbol{\xi}}{R_{\rm E}}), \end{aligned} \tag{2.16}$$

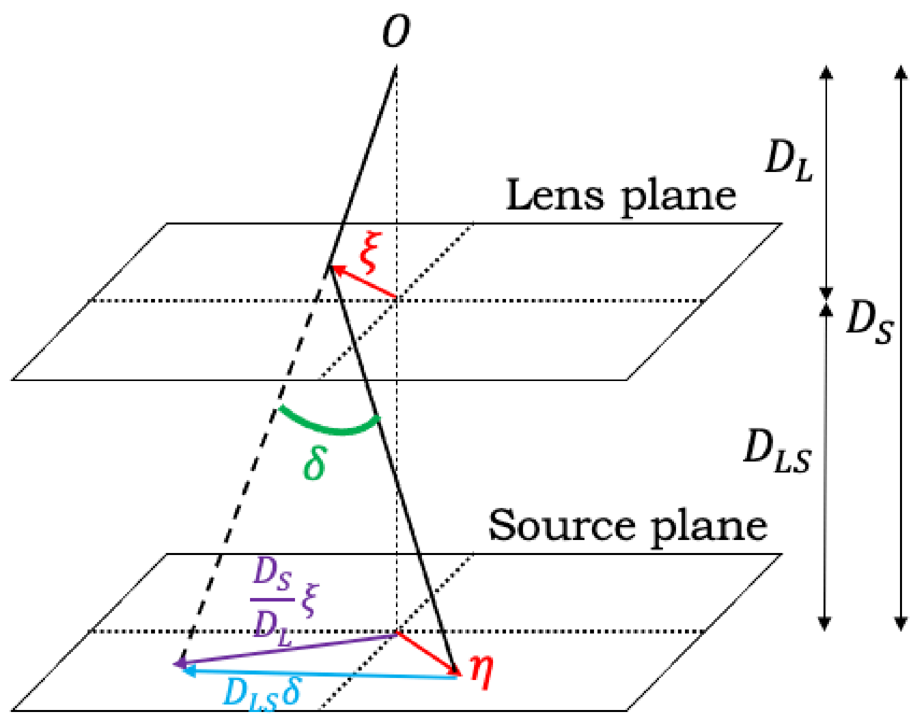

Figure 2.4 A schematic view of microlensing event. O and $\boldsymbol{\eta}$ represent the positions of the observer and the source, respectively. The observed images are located at $\boldsymbol{\xi}$ on the lens plane.

where $\boldsymbol{y}$ is the position vectors of the images on the lens plane and $\boldsymbol{u}$ is the position vector of the source on the lens plane. This is the lens equation using 2-D vectors for the single-lens microlensing.

The bending depends only on the separation between the sources and lenses. Here consider the case where there are N lenses on the lens plane. For the thin lens approximation, the effects of the additional components of gravity corresponds to the sum of the bending caused by each lens component separately. Thus, in this case, the lens equation for the N-components lens is described by

$$\boldsymbol{u} = \boldsymbol{y} - \sum_{i=1}^{N} \varepsilon_i \frac{\boldsymbol{y} - \boldsymbol{a}_i}{|\boldsymbol{y} - \boldsymbol{a}_i|^2}, \tag{2.17}$$

where $\boldsymbol{a}_i$ is the position vectors for the i-th lens on the lens plane, and ε_i is the mass fraction of the i-th lens. Note that ε corresponds to the squared ratio of the Einstein radius,

$$\varepsilon_i = \frac{m_i}{M_L} = \frac{R_{\mathrm{E},i}^2}{R_{\mathrm{E}}^2} = \frac{\theta_{\mathrm{E},i}^2}{\theta_{\mathrm{E}}^2} \tag{2.18}$$

and M_L is the total mass of the lens.

Equation (2.17) represents relation between the source position $\boldsymbol{u}$ and multiple image positions $\boldsymbol{y}$ when N-body lenses $\boldsymbol{a}$ are given. In general, this equation can not be analytically solved even for the simplest case of $N = 2$. For most cases, Equation (2.17) are solved numerically (e.g. Skowron & Gould, 2012). However, the difficulty for solving it significantly increases as the number of the lenses increases because it becomes $(N^2+1)th$ order polynomial in complex number which gives the (N^2+1) possible image positions.

Magnification

Equation (2.17) represents the mapping the positions from the lens plane to the source plane, i.e. $(\boldsymbol{y} \rightarrow \boldsymbol{u})$. The Jacobian matrix for this mapping $\boldsymbol{J}$ is described by

$$\boldsymbol{J} = \frac{\partial \boldsymbol{u}}{\partial \boldsymbol{y}}. \tag{2.19}$$

The determinant $det\boldsymbol{J}$ mean the ratios of the infinitesimal areas between the source and lens planes. Therefore, the magnification can be found from the sum of inverse values of $det\boldsymbol{J}$ at each image position $\boldsymbol{y}_i$,

$$A = \sum_{i=1}^{N} \left(\frac{1}{|det\boldsymbol{J}|} \right)_{\boldsymbol{y}=\boldsymbol{y}_i}. \tag{2.20}$$

For the binary-lens ($N = 2$), if we suppose that $\boldsymbol{y} = (y_1, y_2)$ and $\boldsymbol{a}_i = (a_{i,1}, a_{i,2})$, the determinant can be written by

$$(det\boldsymbol{J})_{\boldsymbol{y}} = 1 - \left[\sum_{i=1}^{N} \varepsilon_i \frac{(y_1 - a_{i,1})^2 - (y_2 - a_{i,2})^2}{|\boldsymbol{y} - \boldsymbol{a}_i|^4} \right]^2 - 4 \left[\sum_{i=1}^{N} \varepsilon_i \frac{(y_1 - a_{i,1})(y_2 - a_{i,2})}{|\boldsymbol{y} - \boldsymbol{a}_i|^4} \right]^2 \tag{2.21}$$

Converting to Polynomial

Here we convert the lens equation (2.17) into a polynomial equation to express each position vector using complex numbers. Here we define the source and image positions using complex numbers by

$$\begin{aligned} \boldsymbol{u} &\rightarrow \ w = u + iv, \ \ \overline{w} = u - iv \\ \boldsymbol{y} &\rightarrow \ z = x + iy, \ \ \overline{z} = x - iy \end{aligned}$$

and then the lens equation is expressed by

$$\begin{aligned} w &= z - \sum_{i=1}^{N} \varepsilon_i \frac{z - z_i}{|z - z_i|^2} \\ &= z - \sum_{i=1}^{N} \frac{\varepsilon_i}{\overline{z} - \overline{z_i}}, \end{aligned} \tag{2.22}$$

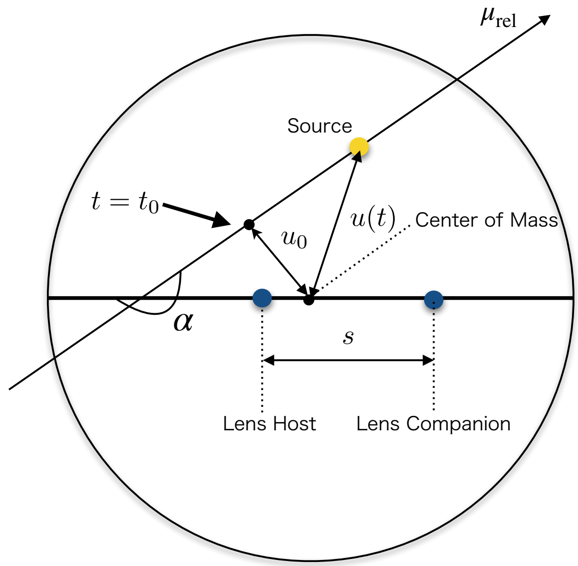

Figure 2.5 The diagram of each parameter for binary-lens

where z_i is the positions of each lens component in the complex coordinate. The determinant of the Jacobian in the complex coordinate can be written as

$$\begin{aligned} det\boldsymbol{J} &= \frac{\partial(u,v)}{\partial(x,y)} = \frac{\partial(w,\overline{w})}{\partial(z,\overline{z})} \\ &= \frac{\partial w}{\partial z}\frac{\partial \overline{w}}{\partial \overline{z}} - \frac{\partial w}{\partial \overline{z}}\frac{\partial \overline{w}}{\partial z} \\ &= 1 - \left|\frac{\partial \overline{w}}{\partial z}\right|^2 \\ &= 1 - |\kappa(z)|^2 \end{aligned} \tag{2.23}$$

where $\kappa(z)$ is defined as

$$\kappa(z) = \frac{\partial \overline{w}}{\partial z} = \sum_{i=1}^{N} \frac{\varepsilon_i}{(z - z_i)^2}. \tag{2.24}$$

Parameters for Binary-lens

Here, I introduce standard binary-lens parameters for the sake of explanations in later sections. Figure 2.5 represents the diagram of each parameter for binary-lens. The definitions of u_0, t_0, and $t_{\rm E}$ are similar to those for the single-lens model. In addition to these, there are three parameters, the mass ratio between the lens components, q, the projected distance between the lenses in units of $R_{\rm E}$, s, and the angle between the source trajectory at t_0 and the binary lens axis, α.

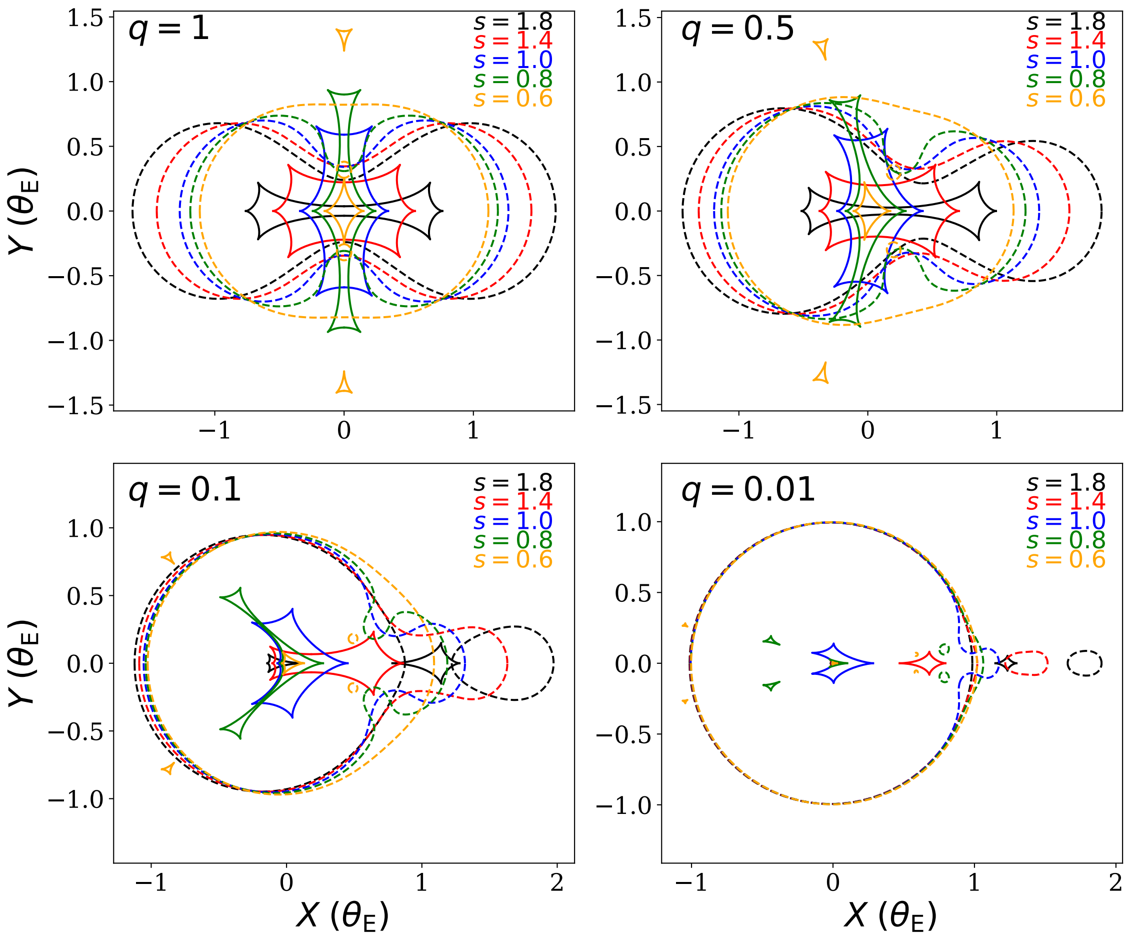

Figure 2.6 Caustic and critical curves with different q and s values. Here, caustic curves and critical curves are described by solid and dashed lines, respectively. Different cases of s values are coded in different colors. The origins are set at the barycenter of the binary lens in every case.

Critical Curve and Caustic

Because the magnification is defined as the inverse of the Jacobian determinant (Equation 2.20), $det\boldsymbol{J} = 0$ means an infinite magnification for a point-source approximation. The points on the lens (image) plane where the image magnification is infinite are called the "critical curve". The critical curves are given as the solutions to

$$\begin{aligned} det\boldsymbol{J} &= 0 \\ \Rightarrow |\kappa(z)|^2 &= 1 \\ \Rightarrow \kappa(z) &= e^{i\psi} \end{aligned} \tag{2.25}$$

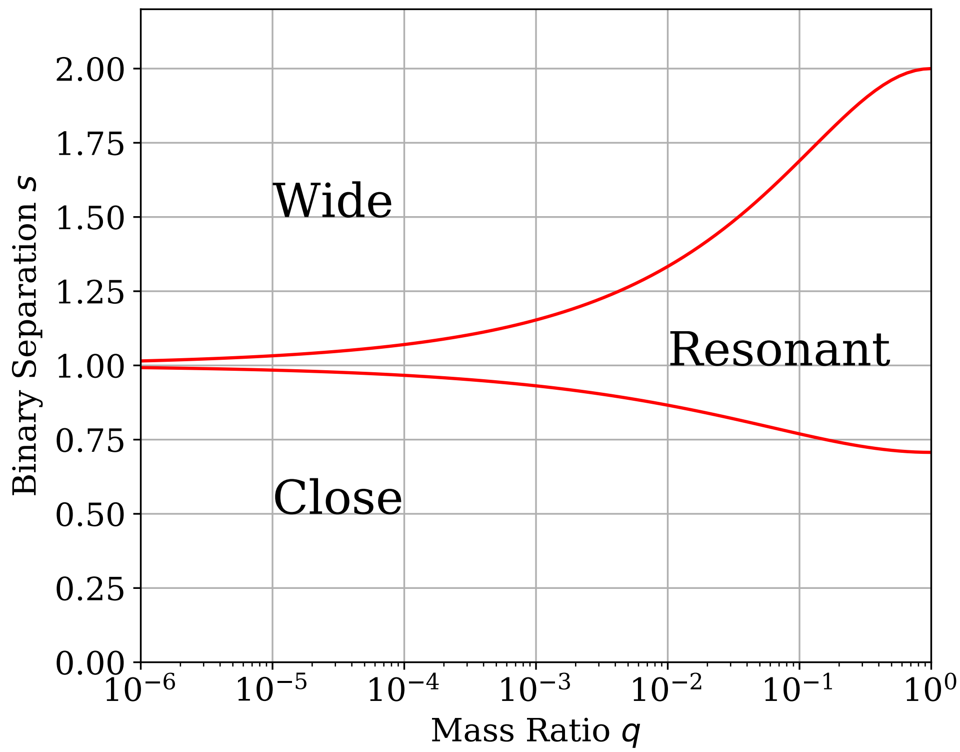

Figure 2.7 The boundaries of d_I and d_{II} that separate the parameter spaces between the resonant caustic and the central and planetary caustics.

where $\psi \in [0, 2\pi)$ (Witt, 1990). Converting Equation (2.25) into a polynomial, we derive

$$\sum_{i=1}^{N} \left[\varepsilon_i \prod_{j \neq i} (z_j - z)^2 \right] - e^{i\psi} \prod_{i} (z_i - z)^2 = 0. \tag{2.26}$$

From Equation (2.26), we need to solve the $2N$-th order polynomial to derive the positions of the critical curve given a ψ. Therefore, the positions of the critical curve are solved numerically. The points on the source plane corresponding to the critical curve are called "caustic". The positions of the caustic can be directly calculated by substituting the positions of the critical curve into Equation (2.17).

The structure of the critical curve and caustic are important for considering the characteristics of the binary-lens microlensing because not only they are positions where the magnification diverges to infinity but also they characterize the pattern of the magnification on the source plane. They depend on only two parameters, the mass ratio q and the distance between the lens components s. Figure 2.6 represents how the caustic and critical curves change with different values of the mass ratio q and s. The critical and caustic curves are represented as dashed and solid lines, and the color coding indicates different cases for (q, s). Here the origin is set on the barycenter of the binary lens in every case.

Each caustic has multiple concave parts called ”folds” and pointed parts called ”cusps”.

First, we consider a case that the two lenses have equal masses ($q = 1$). As the two lenses move apart, the critical curves deviate from a circle, and the caustic curve becomes separated into three components when $s = 0.6$. Hereafter, the caustic at the center between the lenses that has four cusps is called ”central caustic” and the other two smaller caustics that have three cusps are called ”planetary caustic”. For this case of $q = 1$, the central caustic grows with symmetric diamond-like shape as the lens separation s becomes larger and then the two planetary caustics approach toward the central caustic on the line perpendicular to the binary axis. When $1/\sqrt{2} \leq s \leq 2$, the planetary caustics merge into the central caustic and then the critical curve becomes a single closed curve. This caustic curve that has six cusps with relatively large size is called “resonant caustic”. When the lens separation is $s > 2$, the caustic curve is split into two smaller caustics with four cusps and the critical curve is also split into two lines surrounding each lens. For an unequal mass of the lenses with $s > 1$, the smaller one of the two caustics is called “planetary caustic”.

When the mass ratio is unequal ($q < 1$), the symmetric structures for the critical and caustic curves are broken. The central caustic changes with a kite-like shape and is positioned closer to the lens with larger mass than the one with smaller mass. For $s < 1$ where the planetary caustics approach the central caustic as s grows, the lines connecting the planetary and central caustics are tilted toward the larger-mass lens as q decreases.

The resonant caustic is important for planetary microlensing event because it has a maximum sensitivity to small planets and roughly 40% of microlensing planets are detected via the resonant caustic perturbations. The resonant caustic is always larger than the central and planetary caustics for a given q and always form when $s = 1$. Erdl & Schneider (1993) analytically showed the two binary separations d_I and d_{II} in which the resonant caustic becomes split into the central and planetary caustics, for $s < 1$ and $s > 1$ respectively. Figure 2.7 represents the boundaries of d_I and d_{II} in term of q and s. The sizes of the central and planetary caustics are generally scaled by q and $\sqrt{q}$, respectively (Han, 2006). The size of the caustics is also scaled by $|s - 1|$.

Figure 2.8 represents the caustic and critical curve geometries when $q = 0.003$ and $s = 0.8$, in which there are a central caustic and two planetary caustics. And, the magnification patterns are represented as color maps. One can see that the magnification sharply increases around the cusps of the caustics. The magnification patterns are well characterized by the caustic structures. Inside of the caustics, the magnification becomes significantly larger than outside of that. This is because, for example for binary-lens, the number of images is different between the inside ($N_{\rm image} = 5$) and outside ($N_{\rm image} = 3$)[3]. When a source approaches or crosses caustics, characteristic magnification variations are observed. This is a binary-lens microlensing signal.

[3]This indicates that the additional images appear from the positions of the critical curves.

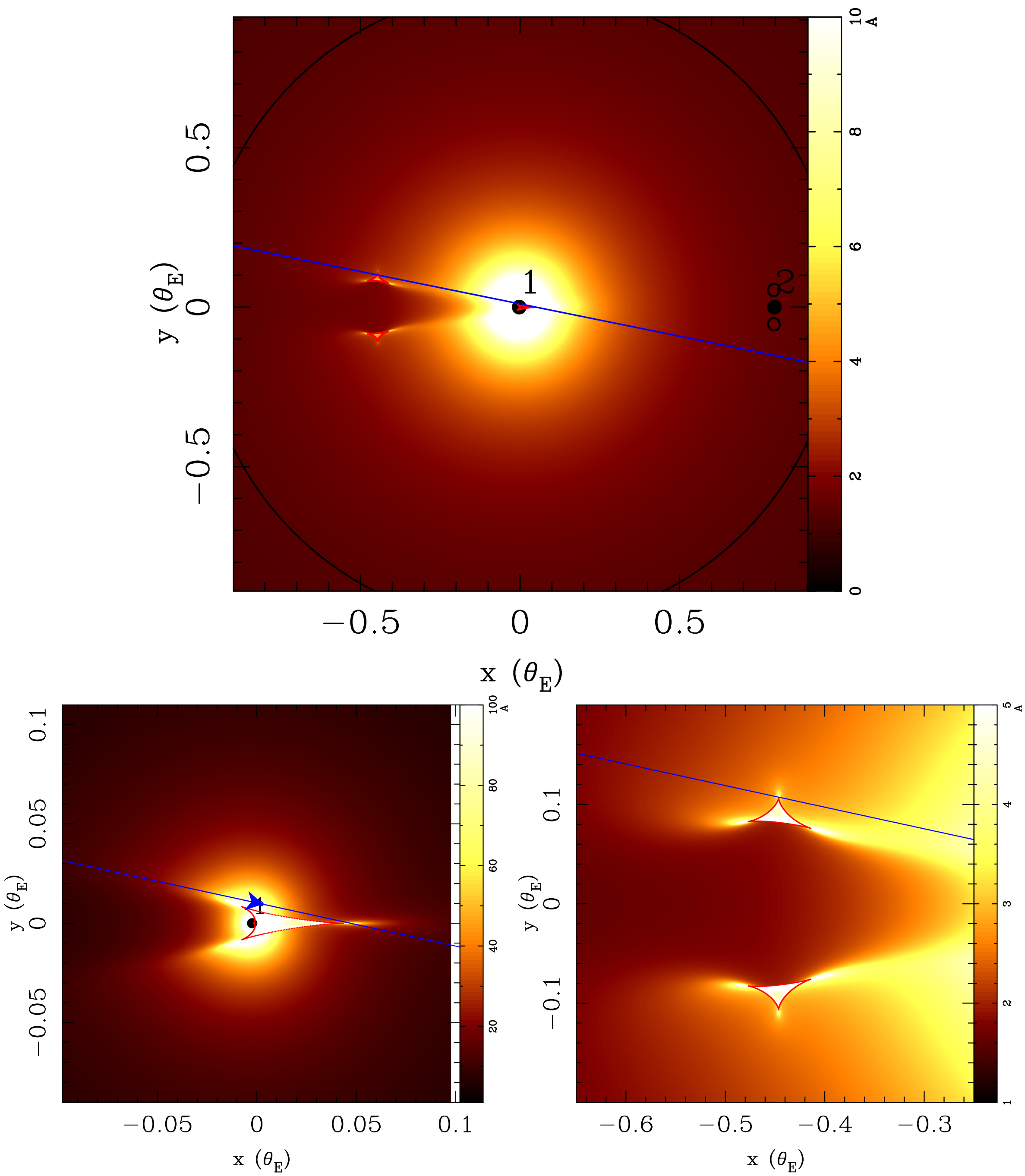

Figure 2.8 The geometries for the caustic (solid red lines) and critical curves (solid black lines) when $q = 0.003$ and $s = 0.8$. The magnification patterns are presented as color maps. The lens positions are shown as black dots. The top panel is a zoom-out view. The bottom two panels are zoom-up views into the central caustic and planetary caustics.

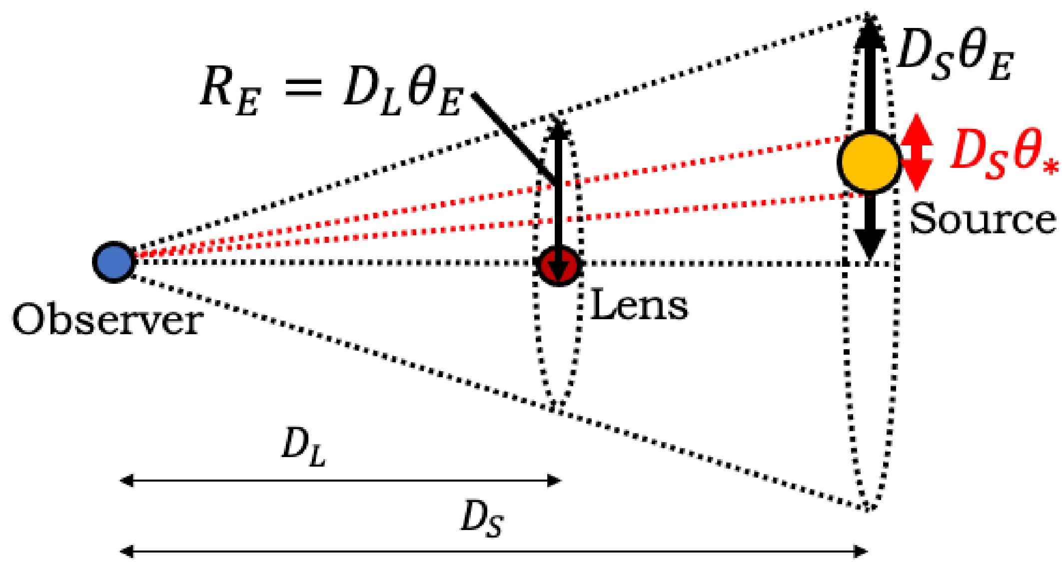

Figure 2.9 A schematic view of the finite source effect.

2.2 High-order Microlensing Effects

In general, physical parameters for the lens system like the lens mass M_L, the distance to the lens system D_L, and the lens-source relative proper motion $\mu_{\rm rel}$, cannot be directly measured from the light curve modeling of microlensing events. This is because such physical parameters are degenerate into one observable, the event timescale $t_{\rm E}$ $(M_L, D_L, \mu_{\rm rel})$. However, the assumptions we have set in previous sections are invalid for some cases and the effects can break the degeneracy and provide important information for the physical parameters. Here I introduce three high-order microlensing effects that are neglected in the previous sections.

2.2.1 Finite Source Effects

At places far from the caustics, the magnification is linearly and smoothly distributed with gentle gradients. The point-source approximation is allowed in such places because the magnification distribution over the source disk is linear and then the total magnification can be approximately calculated as an average of the central value. However, this approximation will be broken when the source is near the caustic where the magnification pattern is not linear and is with steep gradients. This is the finite source effect in microlensing (Witt & Mao, 1994). In such a case, we need to consider the finite source size and take into account the magnification distribution over the source disk in order to calculate the total magnification. The finite source effect is important because it can constrain the angular Einstein radius $\theta_{\rm E}$. From a significant finite source effect, one can

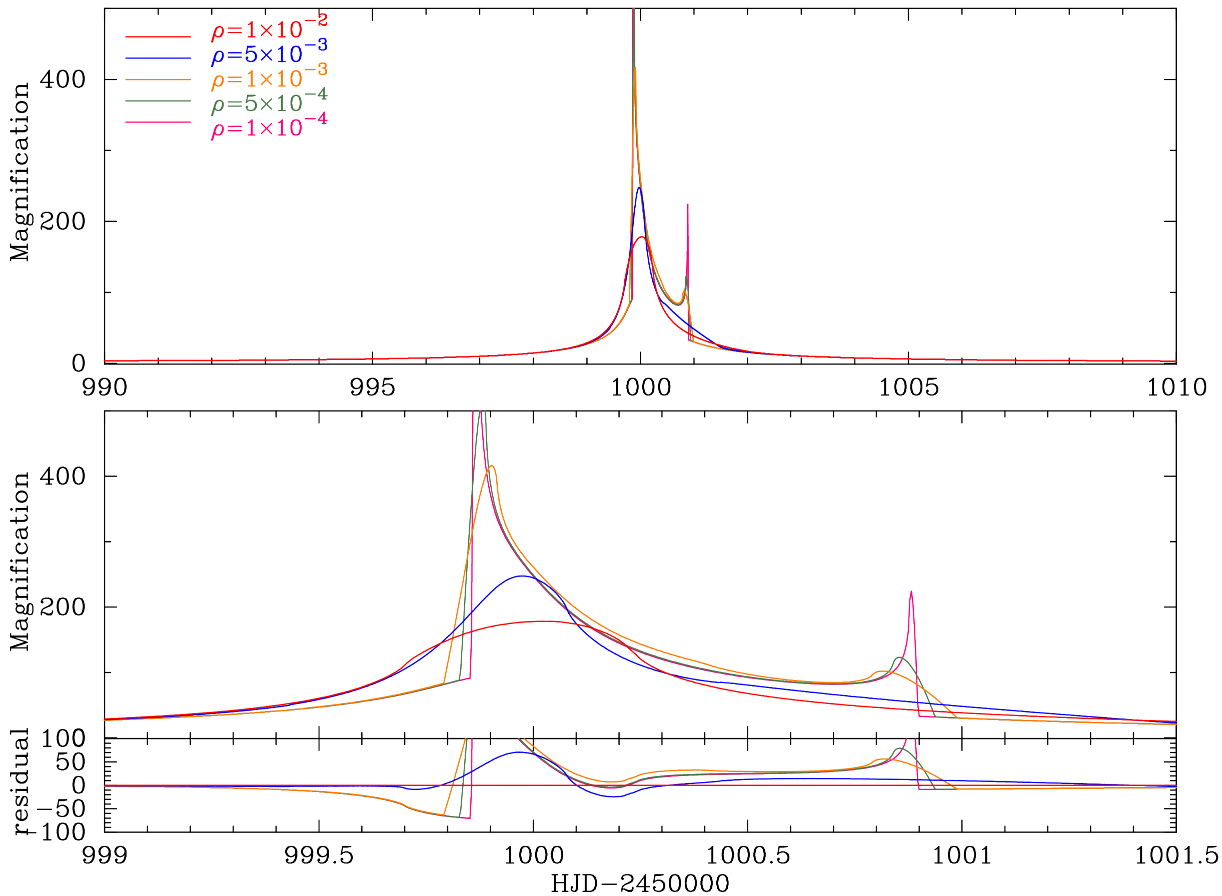

Figure 2.10 The light curves with $\rho = (0.01, 5 \times 10^{-3}, 1 \times 10^{-3}, 5 \times 10^{-4}, 1 \times 10^{-4})$ where other parameters are same with those in Figure 2.8. The top panel shows an overall view of the light curves. The second panel shows the zoom-in view into the anomaly. The bottom panel shows the residuals from the light curve with $\rho = 0.01$.

obtain the angular source size ρ against $\theta_{\rm E}$, i.e.,

$$\rho = \frac{\theta_*}{\theta_{\rm E}} \tag{2.27}$$

where θ_* is the angular radius of the source (see Figure 2.9). Once we estimate θ_* from the source color and magnitude, we can estimate $\theta_{\rm E}$ that provides an important mass-distance relation for the lens system,

$$M_L = \frac{c^2\theta_{\rm E}^2}{4G}\frac{D_S D_L}{D_S - D_L}. \tag{2.28}$$

Here we assume a finite source size $\theta_* = \rho\theta_{\rm E}$ and a uniform brightness distribution over the source disk. For the single-lens, the point-source approximation gives an infinite magnification when $u \to 0$. The image positions of the source edges are given by

$$y_+ = \frac{1}{2}(\rho + \sqrt{\rho^2+4})\theta_{\mathrm{E}}$$
$$y_- = \frac{1}{2}(\rho - \sqrt{\rho^2+4})\theta_{\mathrm{E}}$$

and images from inside the source radius are placed on the side near the angular Einstein radius. From the point symmetry, the overall image is an Einstein ring within $y_- < y < y_+$, and then the magnification is

$$A = \frac{\pi y_+^2 - \pi y_-^2}{\pi \theta_*^2} = \sqrt{1 + 4\left(\frac{\theta_{\mathrm{E}}}{\theta_*}\right)^2} = \sqrt{1+4\rho^{-2}}. \tag{2.29}$$

Therefore, the magnification does not diverge to infinity if considering the finite source size.

Figure 2.10 shows the light curve with $\rho = (0.01, 5\times10^{-3}, 1\times10^{-3}, 5\times10^{-4}, 1\times10^{-4})$ where other parameters are same with those in Figure 2.8. One can find that the sharp features of the light curves around the caustic are duller as the value of ρ increases. The anomaly induced by the caustic crossing or approaching of the source vanishes by extremely large source size. Conversely, it can be said that the smaller the source radius, the higher sensitivity to the anomaly and thus to the lens companions (Bennett & Rhie, 1996).

2.2.2 Parallax Effects

If the observer position is shifted from the original position by a vector $\Delta\boldsymbol{o}$ that is vertical to the observer-source line, the apparent position of the source will be shifted in the opposite direction by

$$\Delta\boldsymbol{s} = -\frac{D_S - D_L}{D_L}\Delta\boldsymbol{o}, \tag{2.30}$$

and then the new position vector of the source can be written by

$$\boldsymbol{s}' = \boldsymbol{s} - \Delta\boldsymbol{s}. \tag{2.31}$$

Here the relation between the projected Einstein radius onto the source plane $\hat{r}_{\mathrm{E}}$ and observer plane $\tilde{r}_{\mathrm{E}}$ can be written by

$$\begin{aligned} \tilde{r}_{\mathrm{E}} &= D_S \frac{R_{\mathrm{E}}}{D_S - D_L} \\ \Rightarrow \tilde{r}_{\mathrm{E}} &= \frac{D_L}{D_S - D_L}\hat{r}_{\mathrm{E}}. \end{aligned} \tag{2.32}$$

Using this relation, we can convert Equation (2.30) into

$$\frac{\Delta\boldsymbol{s}}{\hat{r}_{\mathrm{E}}} = -\frac{\Delta\boldsymbol{o}}{\tilde{r}_{\mathrm{E}}}. \tag{2.33}$$

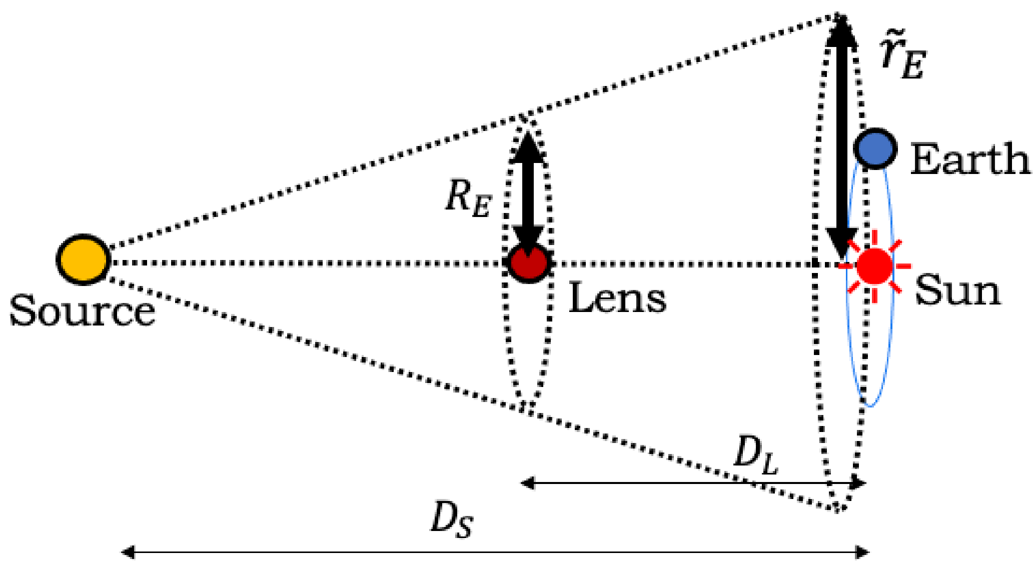

Figure 2.11 A schematic view of the parallax effect.

When we normalize the vector $\Delta\boldsymbol{s}$ and $\Delta\boldsymbol{o}$ by $\hat{r}_{\mathrm{E}}$ and $\tilde{r}_{\mathrm{E}}$ respectively, the relation becomes simpler as

$$\Delta\boldsymbol{s} = -\Delta\boldsymbol{o}. \tag{2.34}$$

In order to incorporate the parallax effect into the magnification formula in Equation (2.13), we define unit vectors that is perpendicular and parallel to the lens-source relative proper motion, $\hat{\boldsymbol{u}}_\perp$ and $\hat{\boldsymbol{u}}_\parallel$. Then, the source position on the lens plane can be described as

$$\boldsymbol{u}(t) = \begin{pmatrix} u_\perp(t) \\ u_\parallel(t) \end{pmatrix} = \begin{pmatrix} u_0 & + & \Delta\boldsymbol{o}(t)\cdot\hat{\boldsymbol{u}}_\perp \\ \frac{t-t_0}{t_{\mathrm{E}}} & + & \Delta\boldsymbol{o}(t)\cdot\hat{\boldsymbol{u}}_\parallel \end{pmatrix}. \tag{2.35}$$

The microlensing parallax vector, $\boldsymbol{\pi}_{\mathrm{E}}$, has a magnitude that gives the projected Einstein radius to the observer plane relative to 1 au, i.e.

$$\pi_{\mathrm{E}} = \frac{1\ \mathrm{au}}{\tilde{r}_{\mathrm{E}}}, \tag{2.36}$$

and its direction gives the direction of the lens-source relative proper motion (see Figure 2.11). Measuring the microlensing parallax effect is important because it gives the physical quantity in Equation (2.36) that gives a mass-distance relation for the lens system as

$$M_L = \frac{c^2}{4G}\left(\frac{1\ \mathrm{au}}{\pi_{\mathrm{E}}}\right)^2 \frac{D_S - D_L}{D_S D_L}. \tag{2.37}$$

This relation is derived independent from the one based on the finite source effect in Equation (2.28). Combining the two independent mass-distance relations, we can derive the lens mass as

$$\begin{aligned} M_L &= \frac{c^2 \times 1\ \mathrm{au}}{4G} \frac{\theta_\mathrm{E}}{\pi_\mathrm{E}} \\ &= \frac{\theta_\mathrm{E}}{\kappa \pi_\mathrm{E}} \end{aligned} \tag{2.38}$$

where $\kappa = 8.144$ mas $M_\odot^{-1}$. And, the multiplication of θ_E and π_E directly gives the lens-source distance relation as

$$\frac{\theta_\mathrm{E}\pi_\mathrm{E}}{1\mathrm{au}} = \frac{D_S - D_L}{D_S D_L}. \tag{2.39}$$

Orbital Parallax

The orbital motion of Earth around the Sun introduces additional non-inertial motions between the source, lens, and observer. This is called the orbital parallax effect. The acceleration induced by the orbital motion causes deviations of the source trajectory from the line that is derived assuming the linear motions.

Because the offset vector $\Delta\boldsymbol{o}$ is defined on the observer plane, we need to calculate it from the Earth position on the orbit plane, $\Delta\boldsymbol{p}$ by projecting it toward the lens plane. The position of the Earth on the orbit plane can approximately and numerically be calculated as a two-body problem. The offset vector $\Delta\boldsymbol{p}(t)$ is calculated by taking the difference between the positions at t and the reference time t_ref,

$$\Delta\boldsymbol{p}(t) = \boldsymbol{p}(t) - \boldsymbol{p}(t_\mathrm{ref}) - (t - t_\mathrm{ref}) \left(\frac{d\boldsymbol{p}}{dt}\right)_{t=t_\mathrm{ref}} \tag{2.40}$$

where $d\boldsymbol{p}/dt$ is the constant velocity of the system. This formula represents the positional offset from that at $t = t_\mathrm{ref}$ and for most case we take $t_\mathrm{ref} = t_0$. This is more convenient than setting $\Delta\boldsymbol{p}(t)$ as an offset from the center of the system (the position of the Sun) because other microlensing parameters like t_0 and u_0 are not needed to be significantly changed depending on whether the parallax effect is included or not (An et al., 2002; Gould, 2004). I omit describing details here for projecting the position vector $\Delta\boldsymbol{p}$ into the observer plane and then we obtain the projected vector $\Delta\boldsymbol{s}$. The source position with the parallax effect can be described by

$$\boldsymbol{u}(t) = \begin{pmatrix} u_\perp(t) \\ u_\parallel(t) \end{pmatrix} = \begin{pmatrix} u_0 & - & \pi_\mathrm{E}\Delta\boldsymbol{s}_\perp(t) \\ \frac{t-t_0}{t_\mathrm{E}} & - & \pi_\mathrm{E}\Delta\boldsymbol{s}_\parallel(t) \end{pmatrix}. \tag{2.41}$$

The projected vector $\Delta\boldsymbol{s}$ can be calculated in any celestial coordinate systems. For the equatorial coordinate, $\Delta\boldsymbol{s} = (\Delta s_n, \Delta s_e)$ where each represents north and east components respectively. In order to align each component of $\Delta\boldsymbol{s}$ to the vectors of $\hat{\boldsymbol{u}}$ and $\hat{\boldsymbol{v}}$, we need a rotate angle ϕ and then

$$\boldsymbol{u}(t) = \begin{pmatrix} u_0 & - & \pi_{\rm E}(\Delta s_e(t)\cos\phi - \Delta s_n(t)\sin\phi) \\ \frac{t-t_0}{t_{\rm E}} & - & \pi_{\rm E}(\Delta s_n(t)\cos\phi + \Delta s_e(t)\sin\phi) \end{pmatrix}. \tag{2.42}$$

When we define the microlensing parallax vector as

$$\boldsymbol{\pi}_{\rm E} = \pi_{\rm E}(\cos\phi, \sin\phi) = (\pi_{{\rm E},N}, \pi_{{\rm E},E}) \tag{2.43}$$

where $\pi_{{\rm E},N}$ and $\pi_{{\rm E},E}$ are the north and east components of $\boldsymbol{\pi}_{\rm E}$, the vector of the impact parameter $\boldsymbol{u}(t)$ is described as

$$\boldsymbol{u}(t) = \begin{pmatrix} u_0 & - & \pi_{{\rm E},N}\Delta s_e(t) + \pi_{{\rm E},E}\Delta s_n(t) \\ \frac{t-t_0}{t_{\rm E}} & - & \pi_{{\rm E},N}\Delta s_n(t) - \pi_{{\rm E},E}\Delta s_e(t) \end{pmatrix}. \tag{2.44}$$

The direction of $\boldsymbol{\pi}_{\rm E}$ is similar to that of the lens-source relative proper motion $\boldsymbol{\mu}_{\rm rel}$. This is because the rotation angle ϕ is defined to meet that.

The orbital parallax effect is generally observed in a relatively long timescale event where the Earth travels in a significant fraction of its orbit. For short timescale events, A significant effect cannot be expected because a straight-line approximation for the source trajectory is sufficient during the events.

Space Parallax and Terrestrial Parallax

From Equation (2.35), the positional shift on the observer plane gives a shift of the source from the lens, and then different peak time $t_{0,\rm shift}$ and minimum impact parameter $u_{0,\rm shift}$ will be observed. This is called space parallax effect (Refsdal, 1966; Gould, 1994). When we define the shift projected on the observer plane $D_\perp$, the microlensing parallax vector is given as

$$\boldsymbol{\pi}_{\rm E} \;\; = \;\; \frac{\rm au}{D_\perp}\left(\frac{\Delta t_0}{t_{\rm E}}, \Delta u_0\right) \tag{2.45}$$

where $\Delta t_0 = t_0 - t_{0,\rm shift}$ and $\Delta u_0 = u_0 - u_{0,\rm shift}$. The larger $\Delta\boldsymbol{o}$, the larger differences of t_0 and u_0 are to be observed. However, note that the shift should be less enough than the projected Einstein radius projected to the observer plane $\tilde{r}_{\rm E}$ to observe the magnification. Typical magnitude of $\tilde{r}_{\rm E}$ for a main-sequence star lens is $\sim$ a few au. Recently, the space parallax effect has been observed in many microlensing events by simultaneously observing events by ground-based observatories and the *Spitzer* space telescope (Yee et al., 2015; Zhu et al., 2017).

For an extreme case, the small positional shifts on different sites on the Earth can provide similar parallax effects, which is called the terrestrial parallax effect. In order to observe this effect, large gradients of magnification with small shifts are needed. There have been two events so far where the terrestrial parallax effect were significantly observed[4], OGLE-2007-BLG-224 (Gould et al., 2009) and OGLE-2008-BLG-279 (Yee et al., 2009).

[4]Freeman et al. (2015) reported the detection of the terrestrial parallax with 3σ confidence level in the microlensing event MOA-2011-BLG-274.

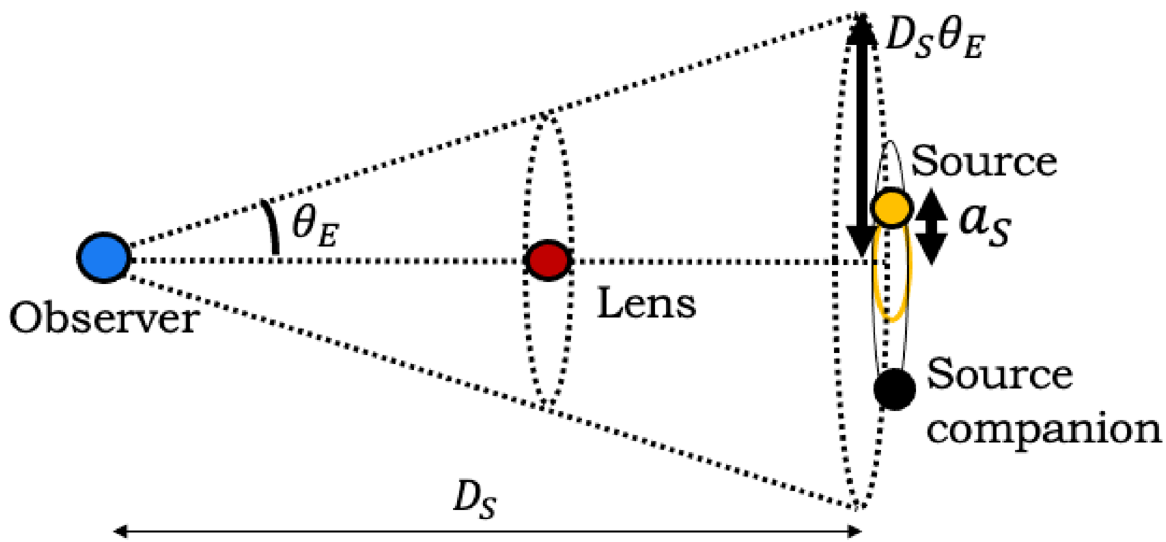

Figure 2.12 A schematic view of the xallarap effect.

2.2.3 Xallarap Effects

If the source has a companion, the source orbital motion can affect the light curve with same mechanism to the orbital parallax effect. This is called the xallarap effect (Griest & Safizadeh, 1998b; Han & Gould, 1997; Poindexter et al., 2005). In contrast to the parallax effect, the xallarap effect can measure the semi-major axis of the source orbit in unit of the Einstein radius projected to the source plane $\hat{r}_{\rm E} = D_S\theta_{\rm E}$;

$$\xi_{\rm E} = \frac{a_S}{\hat{r}_{\rm E}} \tag{2.46}$$

where a_S is the semi-major axis of the source orbit (see Figure 2.12). Kepler's third and Newton's third laws give the following relations,

$$\begin{aligned} \xi_{\rm E} &= \frac{1\ \mathrm{au}}{\hat{r}_{\rm E}}\left(\frac{M_P}{M_\odot}\right)\left[\frac{M_\odot}{M_S+M_P}\frac{P_\xi}{1\ \mathrm{yr}}\right]^{2/3} \\ &\simeq 2\times10^{-5}\left(\frac{1\ \mathrm{au}}{D_S\theta_{\rm E}}\right)\left(\frac{M_P}{M_{\rm Jup}}\right)\left[\frac{M_\odot}{M_S+M_P}\frac{P_\xi}{1\ \mathrm{day}}\right]^{2/3}, \end{aligned} \tag{2.47}$$

$$\begin{aligned} M_S a_S &= M_P a_P \\ \Rightarrow a \equiv a_S + a_P &= \left(1+\frac{M_S}{M_P}\right)a_S, \end{aligned} \tag{2.48}$$

where M_S and M_P are the masses of the source and source companion respectively, P_ξ is the orbital period of the source orbit, and a_P is the semi-major axis of the companion's orbit. The xallarap effect can be degenerate with the orbital parallax effect.

Figure 2.13 MOA-II 1.8m telescope (left) and B&C 61cm telescope (right) at Mt.John Observatory in New Zealand.

2.3 Microlensing Survey Observations

There are two observational requirements in order to detect exoplanets via microlensing, wide field of view (FOV) and high cadence observations. The former comes from the very low probability of microlensing events to occur. The microlensing optical depth, which is a probability that a star is microlensed at a given time, is an order of $\sim 10^{-6}$ even toward a very high-stellar-density region of the Galactic bulge. Therefore, we need to monitor as many background source stars as possible to earn a number of microlensing events. The latter comes from the short timescale of the planetary microlensing signals. The timescale is approximately scaled by a square root of the planetary mass. Typical timescales are $\sim$ a few days for a Jupiter-mass planet and $\sim$ a few hours for an Earth-mass planet.

2.3.1 Current Microlensing Surveys

MOA (Microlensing Observations in Astrophysics) Collaboration

MOA collaboration is an international organization of Japan, the United States, and New Zealand. MOA has been conducting the microlensing survey toward the Galactic bulge by using the MOA-II telescope at Mt.John Observatory in New Zealand, which is mainly for a purpose of the exoplanet survey via microlensing. Mt.John Observatory is the southernmost observatory in the world except for the Antarctic Observatory. In an early phase (MOA-I), the MOA group had been observing the Galactic bulge using the

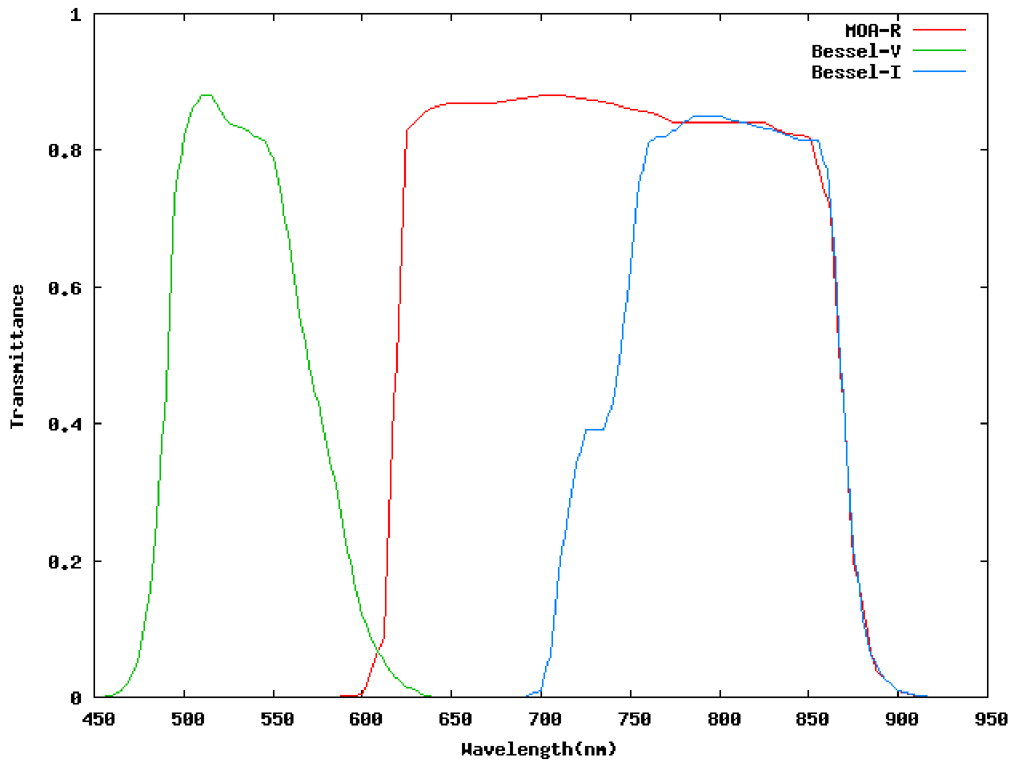

Figure 2.14 Transmittance of filters used in MOA-II.

Boller&Chivens (B&C) 61cm telescope mounted with a mosaic CCD camera with 2k [pix] $\times$ 4k [pix] $\times$ 3 [chips] at Mt.John Observatory (Figure 2.13). Since 2006 (MOA-II), MOA has been conducting the microlensing survey toward the Galactic bulge using the MOA-II 1.8m telescope mounted with a mosaic CCD camera MOA-cam3 (Sako et al., 2008) with 2k [pix] $\times$ 4k [pix] $\times$ 10 [chips]. MOA-II telescope has a large FOV of 2.18 deg^2 and uses in regular survey observations a custom band-pass filter MOA-Red that has a wide wavelength range of transmittance (see Figure 2.14). The large FOV camera enables observing $\sim$50 deg^2 sky area where several tens of millions of stars exist toward the Galactic bulge with $\sim$ 30min cadences on average. MOA detects about 500-600 microlensing events and about several microlensing exoplanets per year.

OGLE (Optical Gravitational Lensing Experiments) Collaboration

OGLE has also been conducting a microlensing survey toward the Galactic bulge using 1.4 deg^2 FOV OGLE-IV camera mounted on Warsaw 1.4m telescope at the Las Campanas Observatory in Chile. Seeing at the Las Campanas Observatory is better than $\sim 1''$ on average and they can observe with better photometric precision than MOA. OGLE detects $\sim 2,000$ microlensing events per year.

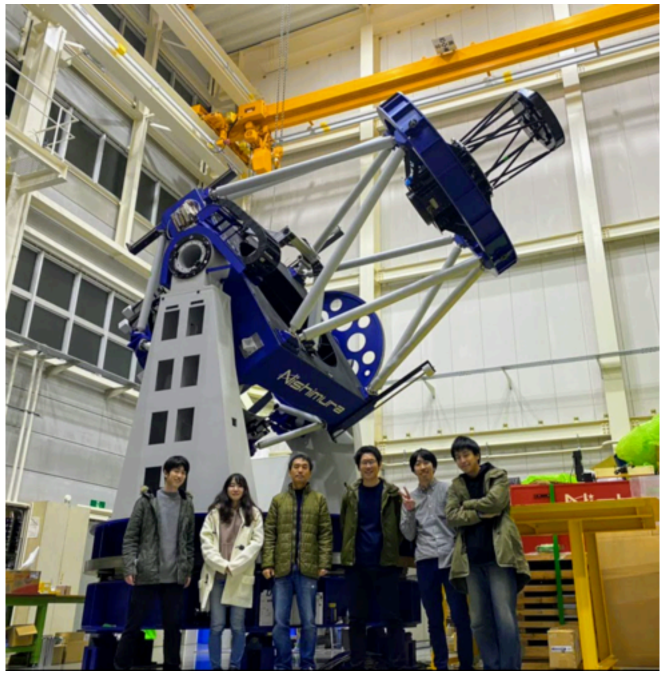

Figure 2.15 A photo showing the PRIME telescope and Japanese members in PRIME collaboration, which was taken at Nishimura factory in Shiga in 2020/11/17. At that time, the optical alignment for the PRIME optics had been completed in Japan and it was scheduled to ship the telescope to South Africa.

KMTNet (Korean Microlensing Telescope Network) collaboration

Since 2015, KMTNet has been conducting a microlensing survey using three 1.6m telescope located at the Cerro Tololo Interamerican Observatory (CTIO) in Chile, the South African Astronomical Observatory (SAAO) in South Africa, and the Siding Spring Observatory (SSO) in Australia. Each of the three telescopes is mounted with a wide FOV (4deg^2) camera and they enable continuously monitoring microlensing events with a 10min cadences and then obtaining light curves without gaps as possible. KMTNet issues $\sim 2,200$ microlensing events per year.

2.3.2 Future Microlensing Survey

PRIME (PRime-focus Infrared Microlensing Experiments) project

The PRIME collaboration will build at the Sutherland Observatory in South Africa a wide FOV 1.8m-aperture telescope with the world's largest class Near Infrared (NIR) camera to perform a NIR (H-band) microlensing exoplanet survey (Figure 2.15). In the current microlensing survey in an optical wavelength, source stars in low galactic latitudes ($|l| < 2°$) cannot be monitored because they suffer from significant interstellar extinction so that they are too faint in optical wavelength (Figure 2.16). However, such sky regions have

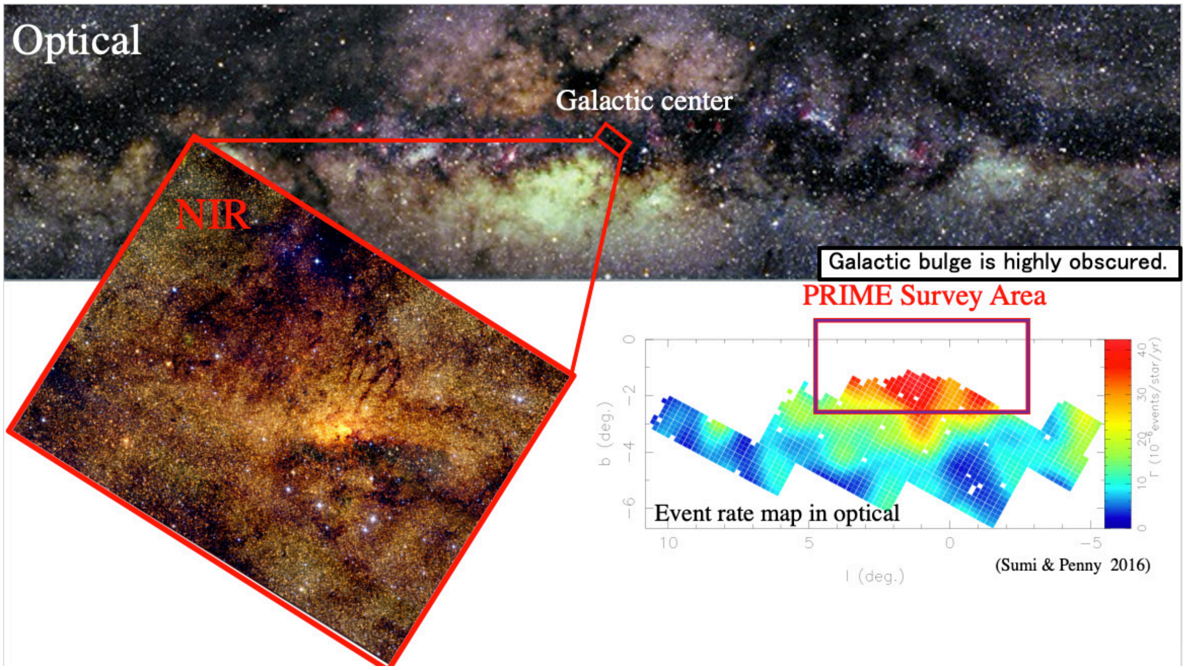

Figure 2.16 The top figure represents a picture when we observe toward the Galactic center in optical wavelength. The regions near the Galactic plane are highly obscured by interstellar extinction. The left bottom inset shows a NIR view of the red rectangle region in the top figure. More source stars near the Galactic plane can be monitored by observing in NIR. The right bottom panel shows the microlensing event rate map toward the Galactic bulge estimated by the optical microlensing survey by MOA-II (Sumi et al., 2013; Sumi & Penny, 2016). PRIME will conduct a NIR microlensing survey in the low l regions and reveal the microlensing event rate map there.

higher stellar density than regions that can be observed in optical and the microlensing event rate is expected to be highest within $\sim$ some degrees near the Galactic center region. The effcts of extinction can be reduced by NIR observations. PRIME will conduct the NIR microlensing survey over the broad regions of the low galactic latitude and will discover dozens of exoplanets including Earth-mass planets. PRIME will also contribute to optimizing the survey strategy and field for the future space-based microlensing survey conducted by the *Nancy Grace Roman Space Telescope*. This project is achieved by loaning four state-of-the-art large size NIR detectors from the *Roman* team, NASA. PRIME will start the survey observation in 2021.

The *Roman Galactic Exoplanet Survey*

The *Nancy Grace Roman Space Telescope* (*Roman*) (Spergel et al., 2015) is the NASA astrophysics flagship mission following the *James Webb Space Telescope*. *Roman* was selected as the top-priority large space mission of the 2010 astronomy and astrophysics decadal survey. It has a 2.4m primary mirror and will conduct a NIR microlensing ex-

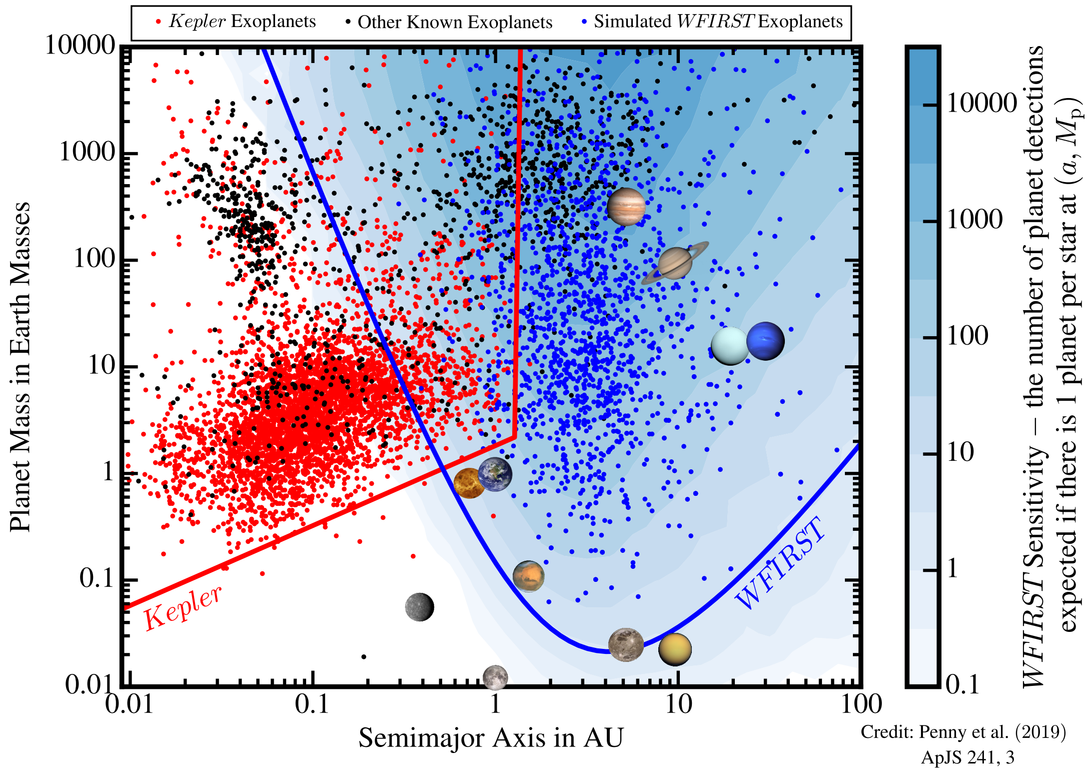

Figure 2.17 Survey sensitivity of the *Kepler* mission (solid red line) and of the *Roman* mission (solid blue line). Detailed explanations about this figure are given in the caption of Figure 9 in Penny et al. (2019).

oplanet survey in the low galactic bulge fields for 72 days $\times$ 6 seasons, which is called the *Roman Galactic Exoplanet Survey* (Johnson et al., 2020). A space-based observation is the most suitable for the exoplanet microlensing survey because it can resolve stars in crowded fields and its continuous observations can avoid missing short planetary signals regardless of any weather condition (Bennett & Rhie, 2002). During the entire mission period, it is expected that *Roman* will detect ~ 1400 bound exoplanets via microlensing, including ~ 200 exoplanets with mass $\leq 3\ M_{\oplus}$ (Penny et al., 2019). The *Roman* survey has a sensitivity to small planets with masses down to Mercury and will provide an exoplanet sample of a wide range of physical parameter spaces that cannot be explored by other exoplanets surveys like the *Kepler* mission (See Figure 2.17). *Roman* is planned to be launched and start observations in 2025.

Chapter 3

OGLE-2013-BLG-0911Lb: A Secondary on the Brown-Dwarf Planet Boundary around an M-dwarf

We present the analysis of the binary-lens microlensing event OGLE-2013-BLG-0911. The best-fit solutions indicate the binary mass ratio of $q \simeq 0.03$ which differs from that reported in Shvartzvald et al. (2016). The event suffers from the well-known close/wide degeneracy, resulting in two groups of solutions for the projected separation normalized by the Einstein radius of $s \sim 0.15$ or $s \sim 7$. The finite source and the parallax observations allow us to measure the lens physical parameters. The lens system is an M-dwarf orbited by a massive Jupiter companion at very close ($M_{\rm host} = 0.30^{+0.08}_{-0.06}\ M_{\odot}$, $M_{\rm comp} = 10.1^{+2.9}_{-2.2}\ M_{\rm Jup}$, $a_{\rm exp} = 0.40^{+0.05}_{-0.04}$ au) or wide ($M_{\rm host} = 0.28^{+0.10}_{-0.08}\ M_{\odot}$, $M_{\rm comp} = 9.9^{+3.8}_{-3.5}\ M_{\rm Jup}$, $a_{\rm exp} = 18.0^{+3.2}_{-3.2}$ au) separation. Although the mass ratio is slightly above the planet-brown dwarf (BD) mass-ratio boundary of $q = 0.03$ which is generally used, the median physical mass of the companion is slightly below the planet-BD mass boundary of $13 M_{\rm Jup}$. It is likely that the formation mechanisms for BDs and planets are different and the objects near the boundaries could have been formed by either mechanism. It is important to probe the distribution of such companions with masses of $\sim 13 M_{\rm Jup}$ in order to statistically constrain the formation theories for both BDs and massive planets. In particular, the microlensing method is able to probe the distribution around low-mass M-dwarfs and even BDs which is challenging for other exoplanet detection methods.

3.1 Introduction

Brown dwarfs (BDs) have masses of $13 - 75 M_{\rm Jup}$ being intermediate between the masses of the main-sequence stars and planets (Burrows et al., 1993). Although the existence of BDs was firstly proposed in Kumar (1962), there had been no observational evidence for BDs until 1995 (Nakajima et al., 1995) owing to their low luminosities and temperatures. To date, more than ten thousand field BDs have been discovered by several survey groups,

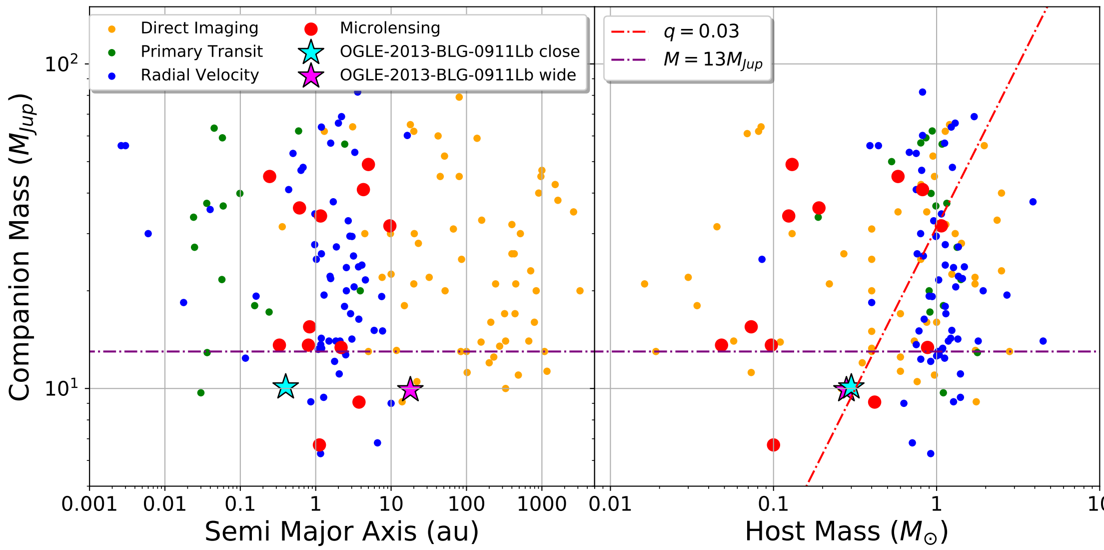

Figure 3.1 Distributions of discovered BD/massive-planet companions ($5M_{\rm Jup} \leq M \leq 75M_{\rm Jup}$) obtained from http://exoplanet.eu, in which the vertical axis shows the companion masses. The horizontal axes for the left and right panels indicate the semi major axes and host masses, respectively. The yellow, green, blue and red points indicate the BD/massive-planet companions discovered by Imaging, Transit, Radial Velocity and Microlensing method, respectively. The two solutions for OGLE-2013-BLG-0911Lb are represented as stars.

which are summarized in the Table 1 of Carnero Rosell et al. (2019). Most current theories predict that field BDs are formed in a fashion similar to that of main sequence stars, through direct gravitational collapse and turbulent fragmentation of molecular clouds (Luhman, 2012). These theories are observationally supported. For example, André et al. (2012) found self-gravitating dense clumps of gasses and dust with mass 0.015-0.03$M_\odot$,which are similar to those of low mass BDs. On the other hand, the core accretion mechanism (Mordasini et al., 2009; Tanigawa & Tanaka, 2016) and that of gravitational instability (Boss, 1997, 2001) are also able to produce companions of BD masses in protoplanetary disks. Radial velocity (RV) surveys have revealed that the frequency of BD companions with orbital radii less than $\sim$ 3 au around main sequence stars is relatively lower than that of stellar and planetary-mass companions (Marcy & Butler, 2000; Grether & Lineweaver, 2006; Johnson et al., 2010), the so-called “brown dwarf desert”. It is likely that this BD deficit is because of differences between the formation mechanisms of companions with planetary mass and stellar mass. However, it is not yet clear if the BD-mass companions formed like planets in the protoplanetary disk, formed as binary stars in the molecular cloud or were captured by the primary stars. Some theories have suggested that the BD desert might be an outcome of the interaction between massive companions and protoplanetary disks and/or of tidal evolution (Armitage & Bonnell, 2002; Matzner & Levin, 2005; Duchêne & Kraus, 2013).

Gravitational microlensing (Mao & Paczynski, 1991) surveys have probed the distribution of the outer planetary systems beyond the snow line (Hayashi, 1981), where the ice-dominated solid materials are rich, leading to efficient formation of gas-giant planets according to the core accretion theory (Lissauer, 1993; Pollack et al., 1996). Because microlensing does not depend on the luminosity of the host star, the technique is sensitive to companions to low mass objects such as late M-dwarfs or even BDs. Furthermore, the host and any companions can still be inferred at distances all the way to the Galactic bulge. In contrast, the RV and transit (Borucki et al., 2010) methods, which have discovered the bulk of currently known exoplanets and BDs orbiting around hosts, have only a sensitivity to companions relatively close to hosts and whose hosts are sufficiently bright. Figure 3.1 shows the distribution of discovered BD/massive-planet companions around main sequence stars and BDs. The RV (blue dots) and transit (green dots) methods have discovered a lot of the companions around 1 $M_{\odot}$ stars but only a few around low-mass stars below 0.5 $M_{\odot}$. This would be caused by an observational bias due to the faintness of low-mass stars in visible wavelength range. The direct imaging (orange dots) method has detected the companions around hosts with masses of $0.01 - 3$ $M_{\odot}$ but it could not have resolved the companions with relatively short orbital radii. On the other hand, microlensing (red dots) has discovered BD/massive-planet companions around hosts with masses of $\sim 0.05 - 1 M_{\odot}$ with orbital radii of $\sim 0.3 - 10$ au (e.g. Ranc et al., 2015; Han et al., 2017; Ryu et al., 2018), which are complementary to other detection methods. Gaudi (2002) estimated that more than 25% of BD companions with separations $\sim 1 - 10$ au would be detected by present microlensing surveys. According to the standard core accretion theory, massive planets and also BDs are more difficult to form around low-mass M dwarfs than solar-type stars owing to low disk surface densities (Ida & Lin, 2005) and long timescales (Laughlin et al., 2004). It is possible to constrain the BD formation mechanism around late M dwarfs from a statistical analysis of microlensing results in the BD-mass regime, which can be compared to the lack of close-in BD companions around solar-type stars found by RV observations.

Shvartzvald et al. (2016), hereafter S16, conducted a statistical analysis of the first four seasons of a "second-generation" microlensing survey (Gaudi et al., 2009) which consisted of the observations by the Optical Gravitational Lensing Experiment (OGLE; Udalski et al., 1994) collaboration, the Microlensing Observations in Astrophysics (MOA; Bond et al., 2001; Sumi et al., 2003) collaboration and the Wise team (Shvartzvald & Maoz, 2012). They analyzed 224 microlensing events and found 29 "anomalous" events which imply the presence of a companion to the lens host. They performed an automated coarse grid search for light curve modelings rather than a detailed modeling of individual events for their statistical study. Finally, they derived the planet (binary) frequency distribution as a function of companion-to-host mass ratio q and found a possible deficit at $q \sim 10^{-2}$. However, it is worthwhile to conduct the detailed analysis of individual "planetary candidate" in their sample which do not have any models in literature. For example, they reported that OGLE-2013-BLG-0911 has a planetary mass-ratio of $q \approx 3 \times 10^{-4}$, but we found new preferred solutions with a less extreme mass ratio, $q \approx 3 \times 10^{-2}$.

Here, we present the analysis of a high-magnification (maximum magnification of

$A_{\max} \sim 220$) microlensing event, OGLE-2013-BLG-0911. The "anomaly" due to a companion to the lens star was clearly detected near the peak of the light curve. We present the observations and datasets of the event in Section 3.2. Our light curve analysis is described in Section 3.3. In Section 3.4, we present our analysis of the source properties. The physical parameters of the lens system are described in Section 3.5. We summarize and discuss the result in Section 3.6.

3.2 Observation & Data Sets

3.2.1 Observation

The microlensing event OGLE-2013-BLG-0911 was discovered and alerted as a microlensing candidate on 2013 June 3 UT 21:51 by the fourth phase of the OGLE collaboration (OGLE-IV; Udalski et al., 2015). OGLE-IV[1] is conducting a microlensing exoplanet search toward the Galactic bulge using the 1.3m Warsaw telescope of Las Campanas Observatory in Chile with a wide total field of view (FOV) of 1.4 deg^2. The OGLE observations were conducted using the standard I- and near-standard V-band filters. The second phase of the MOA collaboration[2] (MOA-II; Bond et al., 2017) is also carrying out a microlensing survey toward the Galactic bulge using the 1.8m MOA-II telescope with a 2.2deg^2 FOV CCD camera (MOA-cam3; Sako et al., 2008) at Mount John Observatory (MJO) in New Zealand. Thanks to its wide FOV, the MOA collaboration is observing bulge stars with a cadence of 15-90min every day depending on the field. The MOA survey independently discovered and issued an alert for the event as MOA-2013-BLG-551. The MOA observations were conducted using a custom wide-band filter, "MOA-Red", which corresponds approximately to the combination of the standard I and R filters. The Wise[3] team also conducted a microlensing survey from 2010 to 2015 and monitored a field of 8 deg^2 within the observational footprints of both OGLE and MOA (Shvartzvald & Maoz, 2012). They observed using the 1m Wise telescope at Wise Observatory in Israel with a 1 deg^2 FOV LAIWO camera (Gorbikov et al., 2010) and the cadence for each of the eight Wise fields was $\sim$ 30min.

The event was located at $(\mathrm{R.A.}, \mathrm{Dec.})_{\mathrm{J2000}}$=(17:55:31.98, −29:15:13.8) or Galactic coordinates $(l, b) = (0.84°, -2.02°)$. Real-time analysis predicted the event would reach high peak magnification during which the sensitivity to low-mass companions is high (Griest & Safizadeh, 1998a; Rattenbury et al., 2002). Follow-up observations during the period of high magnification were encouraged to capture short planetary signals. Consequently, in addition to the OGLE and MOA survey observations, the light curve was densely observed by several follow-up groups: Microlensing Follow Up Network (μFUN; Gould et al., 2006), Microlensing Network for the Detection of Small Terrestrial Exoplanets (MiNDSTEp; Dominik et al., 2010) and RoboNet (Tsapras et al., 2009; Dominik et al., 2019). Hereafter,

[1] http://ogle.astrouw.edu.pl/ogle4/ews/ews.html
[2] https://www.massey.ac.nz/ iabond/moa/alerts/
[3] http://wise-obs.tau.ac.il/ wingspan/

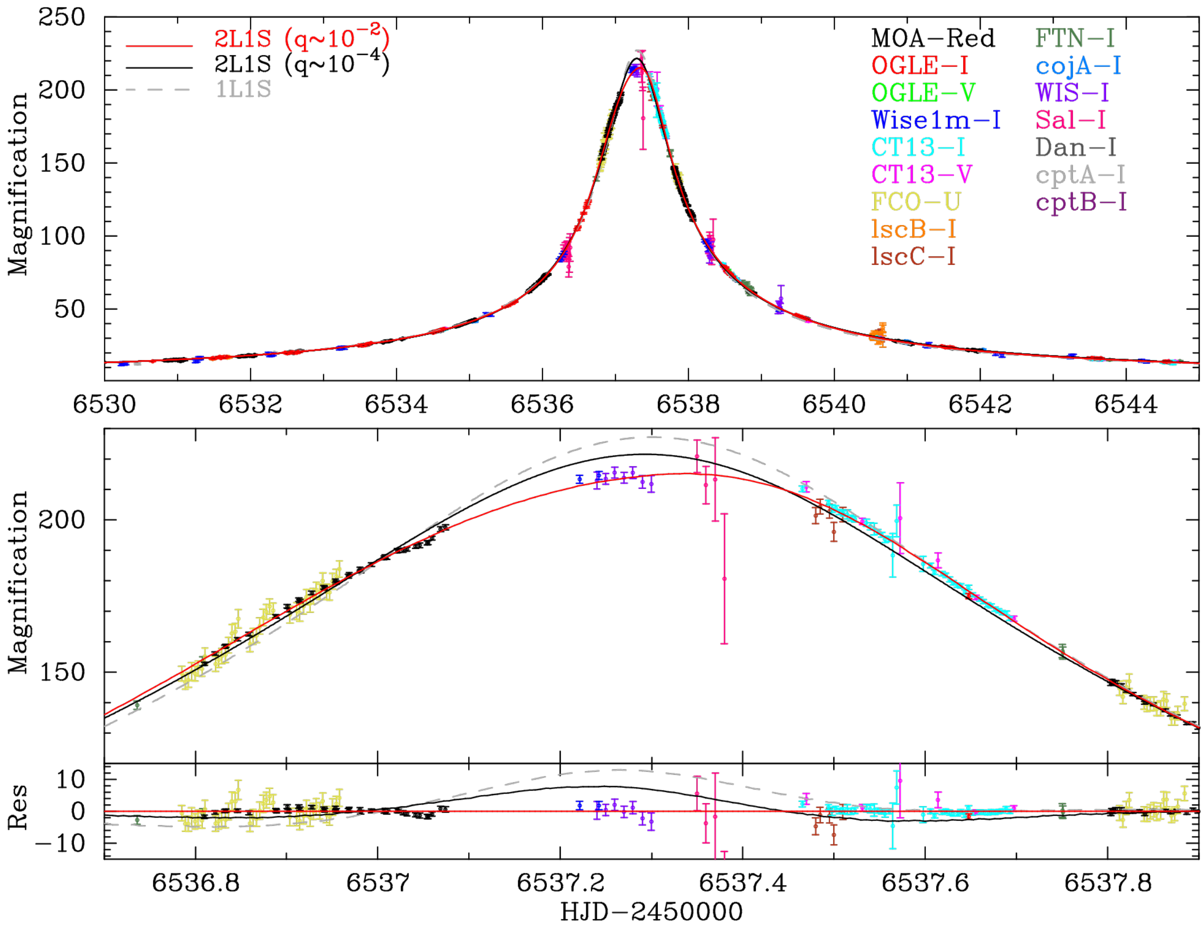

Figure 3.2 (Top) The light curve of OGLE-2013-BLG-0911. Each color on the data point corresponds to each instrument, shown on the right. The error bars are renormalized following Equation (3.1). The solid red, black and dashed gray curves represent the static 2L1S with $q \sim 10^{-2}$, 2L1S with $q \sim 10^{-4}$ and 1L1S models, respectively. (Middle) A zoom-in around the peak. (Bottom) Residuals of the zoom-in light curve from the model of 2L1S with $q \sim 10^{-2}$.

we refer this event as OGLE-2013-BLG-0911.

3.2.2 Data reduction

All the datasets of OGLE-2013-BLG-0911 are summarized in Table 3.1. Most photometric pipelines use the Difference Image Analysis (DIA; Alard & Lupton, 1998; Alard, 2000) technique, which is very effective in high stellar density fields such as those towards the Galactic bulge. The MOA and μFUN CTIO data were reduced with the MOA implementation of the DIA method (Bond et al., 2001, 2017). The OGLE data were reduced by OGLE's DIA pipeline (Wozniak, 2000). The Wise data were reduced using the pySIS DIA software (Albrow et al., 2009). The other μFUN data and MiNDSTEp data were reduced by DoPhot (Schechter et al., 1993) and DanDIA (Bramich, 2008; Bramich et al., 2013). RoboNet data were reduced using a customized version of the DanDIA pipeline (Bramich, 2008).

It is known that the nominal photometric error bars given by each photometric pipeline are potentially underestimated in high stellar density fields toward the bulge. Therefore, we empirically renormalized the error bars for each data set following procedure of Bennett et al. (2008) and Yee et al. (2012), i.e.,

$$\sigma_i^{'} = k\sqrt{\sigma_i^2 + e_{\rm min}^2}\ , \tag{3.1}$$

where $\sigma_i^{'}$ and σ_i represent the renormalized errors and the original errors given by the pipelines, respectively. The parameters k and $e_{\rm min}$ are the coefficients for the error renormalization. Here, $e_{\rm min}$ represents the systematic errors when the source flux is significantly magnified. We added 0.3% in quadrature to each error, i.e. $e_{\rm min} = 0.003$, and then calculated k values in order to achieve a value of $\chi^2/{\rm dof} = 1$ for each dataset (Bennett et al., 2014; Skowron et al., 2016). We list the renormalization coefficients k in Table 3.1 along with the number of used data points $N_{\rm use}$. We confirmed that the final best-fit model is consistent with the preliminary best-fit model found using the datasets before the error renormalization.

Table 3.1: Data Sets for OGLE-2013-BLG-0911

Site	Telescope	Collaboration	Label	Filter	$N_{\rm use}$	k
Mount John Observatory	MOA-II 1.8m	MOA	MOA	*Red*	8761	1.055
Las Campanas Observatory	Warsaw 1.3m	OGLE	OGLE	I	6895	1.480
Las Campanas Observatory	Warsaw 1.3m	OGLE	OGLE	V	78	1.344
Florence and George Wise Observatory	Wise 1m	Wise	Wise1m	I	253	0.947
Cerro Tololo-Inter American Observatory (CTIO)	SMARTS 1.3m	μFUN	CT13	I	189	1.230
Cerro Tololo-Inter American Observatory (CTIO)	SMARTS 1.3m	μFUN	CT13	V	35	1.182
Farm Cove Observatory	Farm Cove 0.36m	μFUN	FCO	Unfiltered	55	2.146
Weizmann Institute of Science, Marty S. Kraar Observatory	Weizmann 16inch	μFUN	WIS	I	17	1.140
Haleakala Observatory	Faulkes North 2.0m	RoboNet	FTN	i'	27	2.181
Siding Spring Observatory (SSO)	LCO 1.0m, Dome A	RoboNet	cojA	i'	31	1.920
Cerro Tololo Inter-American Observatory (CTIO)	LCO 1.0m, Dome B	RoboNet	lscB	i'	51	1.311
Cerro Tololo Inter-American Observatory (CTIO)	LCO 1.0m, Dome C	RoboNet	lscC	i'	71	2.315
South African Astronomical Observatory (SAAO)	LCO 1.0m, Dome A	RoboNet	cptA	i'	32	0.559
South African Astronomical Observatory (SAAO)	LCO 1.0m, Dome B	RoboNet	cptB	i'	8	0.497
ESO's La Silla Observatory	Danish 1.54m	MiNDSTEp	Dan	I	76	2.087
Salerno University Observatory	Salerno 0.36m	MiNDSTEp	Sal	I	20	1.607

The WIS, Sal and lscC data are binned for 0.01 days.

Table 3.2: Comparisons between each microlensing model

Model			N_{param}	χ^2	BIC	$\Delta\chi^2$	ΔBIC
1L1S		Static	4	21027.4	21066.3	4485.1	4368.5
1L2S		Static	10	18631.0	18728.2	2088.7	2030.4
1L2S		Xallarap	12	17554.3	17670.9	1212.0	973.1
2L1S	$(s < 1)$	Static	7	17473.7	17541.7	931.4	843.9
2L1S	$(s < 1, u_0 > 0)$	Parallax	9	17262.7	17350.2	720.4	652.4
2L1S	$(s < 1, u_0 > 0)$	Xallarap	14	16587.6	16723.6	45.3	25.8
2L1S	$(s < 1, u_0 > 0)$	Parallax+Xallarap	16	16558.9	16714.4	16.6	16.6
2L2S	$(s < 1, u_0 > 0)$	Parallax+Xallarap	16	16542.3	16697.8	-	-

3.3 Light Curve Modeling

Here, we present the light curve modeling for OGLE-2013-BLG-0911. Figure 3.2 represents the light curve of OGLE-2013-BLG-0911. The main anomalous feature can be seen between $6536.8 < \mathrm{HJD} - 245000 < 6537.6$. A standard single-lens single-source (1L1S) model fits the data worse than a binary-lens single-source (2L1S) model by $\Delta\chi^2 > 3500$. In following sections, we present the details of the light curve modeling for OGLE-2013-BLG-0911. In Table 3.2, we summarize the comparisons of the χ^2, number of fitting parameters and Bayesian information criterion (BIC) between microlensing models we examined.

3.3.1 Model Description

Assuming a single source star, the observed flux at any given time in a microlensing event, $F_{\mathrm{obs}}(t)$, can be modeled by the following equation,

$$F_{\mathrm{obs}}(t) = A(t)F_{\mathrm{s}} + F_{\mathrm{b}} \ , \tag{3.2}$$

where $A(t)$ is the magnification of the source flux, F_{s} is the unmagnified source flux, and F_{b} is the blend flux. We note that F_{s} and F_{b} can be, during the fitting process, solved analytically by the linear equation (3.2) at given $A(t)$. For a standard single-lens single-source (1L1S) model, there are four parameters that describe the light curve features (Paczynski, 1986); the time of the source approaching closest to the lens center of mass, t_0; the impact parameter, u_0, in unit of the angular Einstein radius, θ_{E}; the Einstein radius crossing time, t_{E}; the source angular radius, ρ, in unit of θ_{E}. The measurement of ρ is important because it leads to a determination of θ_{E} which is needed for the determination of the the mass-distance relation of the lens system.

In our fitting process, we used a Markov Chain Monte Carlo (MCMC) method (Verde et al., 2003) combined with our implementation of the inverse ray-shooting method (Bennett & Rhie, 1996; Bennett, 2010) in order to find the best-fit model and estimate the parameter uncertainties from MCMC stationary distribution for each parameter. Linear

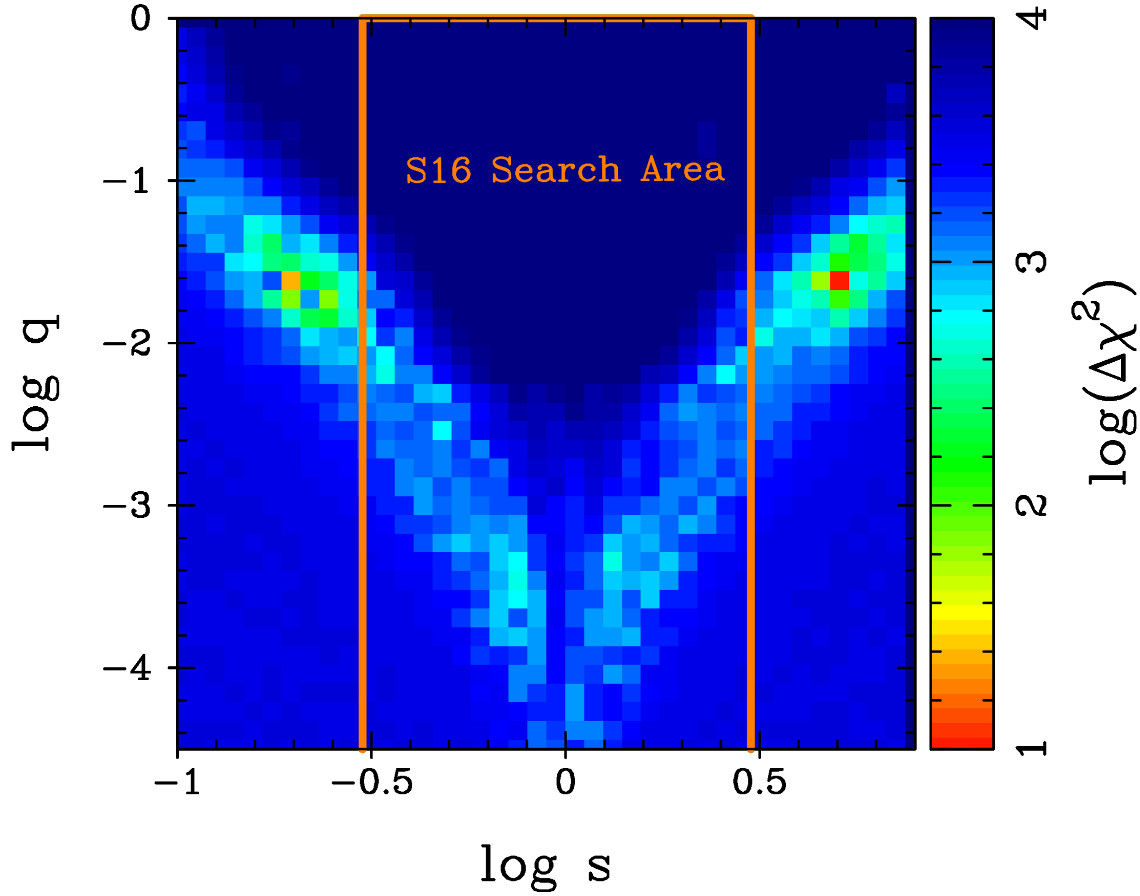

Figure 3.3 The map of the minimum $\Delta\chi^2$ in each s-q grid from the grid search. The orange box corresponds to the area of the grid search analysis in Shvartzvald et al. (2016).

limb-darkening models were used to describe the source star(s) in this work. From the measurement of the intrinsic source color of $(V-I)_{s,0} = 0.71$ described in Section 3.4, we assumed the effective temperature $T_{\rm eff} = 5750$K (González Hernández & Bonifacio, 2009), the surface gravity $\log g = 4.5$ and metallicity $\log[M/H] = 0$. According to the ATLAS model of Claret & Bloemen (2011), we selected the limb darkening coefficients of $u_{Red} = 0.5900$, $u_I = 0.5493$, $u_V = 0.7107$. Here, u_{Red} for the MOA-*Red* band is estimated as the mean of u_I and u_R and the R-band coefficient $u_R = 0.6345$ is used for an unfiltered band.

3.3.2 Binary Lens (2L1S) Model

For a standard binary-lens single-source (2L1S) model, there are three additional parameters; the lens mass ratio between the host and a companion, q; the projected binary separation in unit of the Einstein radius, s; the angle between the source trajectory and the binary-lens axis, α. Here, we introduce two fitting parameters t_c and u_c, for wide ($s > 1$) models. If $s > 1$, the system center in our numerical code is offset from the binary center of mass by

$$\Delta(x, y) = \left[\frac{q}{1+q}\left(\frac{1}{s} - s\right), 0\right]$$

where (x, y) are the parallel and vertical coordinate axes to the binary-lens axis on the lens plane (Skowron et al., 2011), and then we define the time of the source approaching closest to the "system center" and the impact parameter in units of the angular Einstein radius as t_c and u_c, respectively.

Static models

At first, we explored the 2L1S interpretation to explain the anomalous features of the light curve. In modeling 2L1S microlensing light curves, it is common to encounter situations where different physical models explain the observed data equally well, e.g. the close/wide degeneracy (Griest & Safizadeh, 1998a; Dominik, 1999) and the planet/binary degeneracy (Choi et al., 2012; Miyazaki et al., 2018), where different combinations of the microlensing parameters can generate morphologically similar light curves. Therefore, we should thoroughly investigate the multi-dimensional parameter space to find the global preferred model solution. We conducted a detailed grid search over the (q, s, α) parameter space where the magnification pattern strongly depends on these three parameters. The search ranges of q, s and α are $-1 < \log s < 1$, $-4.5 < \log q < 0$ and $0 < \alpha < 2\pi$ with 40 grid points, respectively, and thus the total number of grid points is $40 \times 40 \times 40 = 64000$. We conducted the grid search analysis following the same procedure written in Miyazaki et al. (2018). Figure 3.3 shows the map of the minimum $\Delta\chi^2$ in each s-q grid from the grid search. In Figure 3.3, we found two possible local minima around $(\log q, \log s) \sim (-1.8, -0.75)$ and $\sim (-1.8, 0.75)$, which is caused by the close/wide degeneracy. After refining all the possible solutions, we found the best-fit 2L1S close ($s < 1$) and wide ($s > 1$) models with $q \sim 0.03$, where the χ^2 difference between them is only $\Delta\chi^2 = 4.9$. As seen in Figure 3.2, the 2L1S model with $q \sim 0.03$ provide good fits to the anomalous features around the top of the light curve. We also show the model light curve of 2L1S with $q \sim 10^{-4}$ in Figure 3.2 and it does not fit the light curve anomaly well.

S16 included this event in their statistical analysis as a planetary microlensing events, using a mass ratio of $q \sim 10^{-4}$ for this event. However, our reanalysis found that the static 2L1S models with $q \sim 10^{-2}$ are preferred over the model with $q \sim 10^{-4}$ by $\Delta\chi^2 > 700$. The reason of the oversight is that models with $q \sim 10^{-2}$ are outside of the range of their grid search of $-6 < \log q < 0$ and $0.3 < s < 3$. And the search for the best-fit model outside of this range by refining model parameters found by their grid search was not conducted. Another difference from S16 is that we used re-reduced MOA and OGLE light curves and included all the follow-up datasets. However, we confirmed that the 2L1S models with $q \sim 10^{-4}$ are disfavored relative to the models with $q \sim 10^{-2}$ by $\Delta\chi^2 > 300$ even if we used the survey data, MOA, OGLE and Wise1m. Therefore, note that the survey data were sufficient to identify the new solutions.

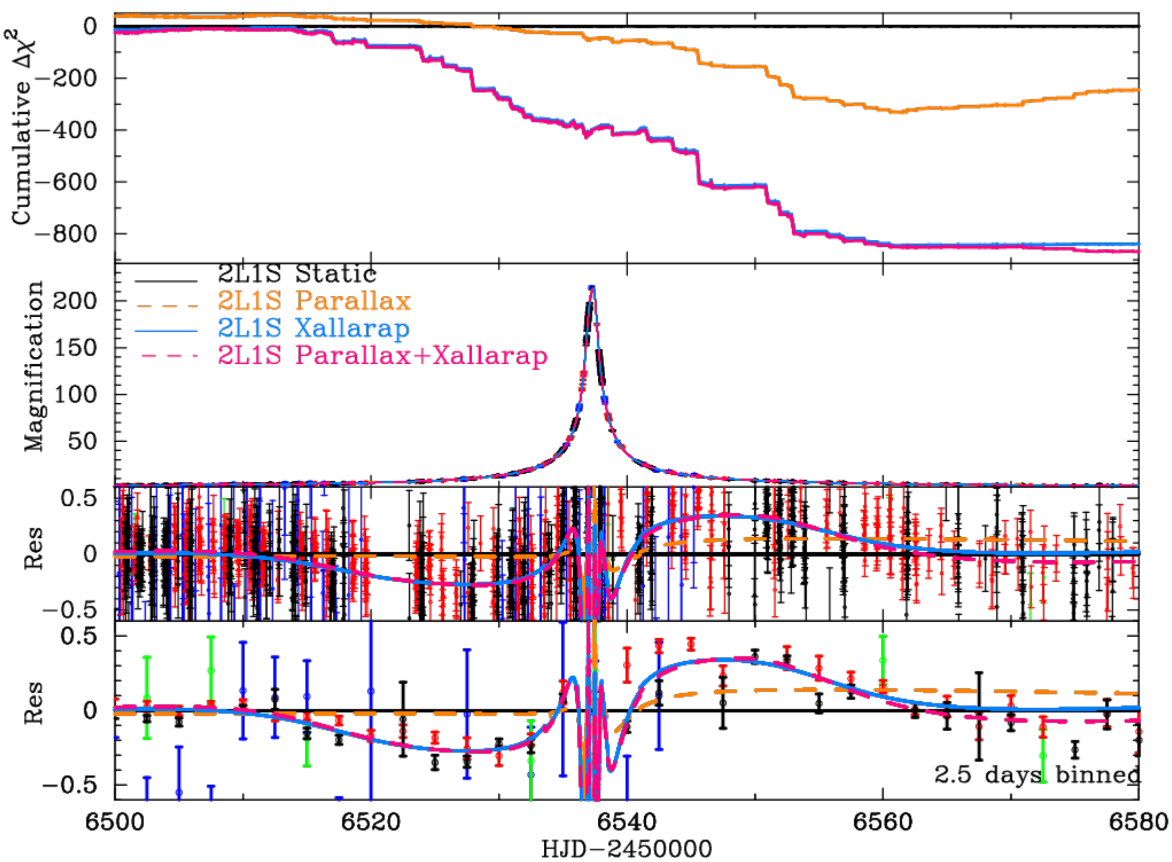

Figure 3.4 (Top) Cumulative $\Delta\chi^2$ distributions of the three 2L1S close ($u_0 > 0$) models compared to the 2L1S static model. (Second from the top) The light curve and models for OGLE-2013-BLG-0911. Here, we plot only MOA, OGLE and Wise1m light curves for clarity. (Third from the top) The residuals of the light curve and models from the static model. (Bottom) The residuals binned by 2 days.

Parallax Effects

Although the best-fit static models provide good fits to the main anomaly features around the peak of the light curve, we found that, overall, the light curve slightly deviates from the static models. The event OGLE-2013-BLG-0911 has $t_{\mathrm{E}} \sim 90$ days and had continued throughout the bulk of the bulge season, which implies that the light curve could be affected by additional high-order microlensing effects.

It is known that the orbital acceleration of Earth causes a parallax effect (Gould & Loeb, 1992; Gould, 2004; Smith et al., 2003). This can be described by the microlensing parallax vector $\boldsymbol{\pi}_{\mathrm{E}} = (\pi_{\mathrm{E},N}, \pi_{\mathrm{E},E})$. Here, $\pi_{\mathrm{E},N}$ and $\pi_{\mathrm{E},E}$ denote the north and east components of $\boldsymbol{\pi}_{\mathrm{E}}$ projected to the sky plane in equatorial coordinates. The direction of $\boldsymbol{\pi}_{\mathrm{E}}$ is defined so as to be identical to that of $\boldsymbol{\mu}_{\mathrm{rel,G}}$, which is the geocentric lens-source relative proper motion projected to the sky plane at a reference time t_{fix}, and the amplitude of $\boldsymbol{\pi}_{\mathrm{E}}$ is $\pi_{\mathrm{E}} = \mathrm{au}/\tilde{r}_{\mathrm{E}}$ where $\tilde{r}_{\mathrm{E}}$ is the Einstein radius projected inversely to the observer plane. We took a reference time $t_{\rm fix} = 6537.3$ days for this event. The measurement of $\boldsymbol{\pi}_{\rm E}$ enables constraints to be placed on the relation between the lens mass M_L and distance D_L (Gould, 2000; Bennett, 2008). For Galactic bulge source events, models with $(u_0, \alpha, \pi_{{\rm E},N})$ and $-(u_0, \alpha, \pi_{{\rm E},N})$ can yield very similar light curves (Skowron et al., 2011). This is reflected as a pair of the symmetric source trajectories to the binary and is sometimes referred to as "ecliptic degeneracy".

Taking the parallax effect into consideration for modeling, we found that the two parallax parameters gave an improvement of $\Delta\chi^2 \sim 210$ compared to the best-fit static model. However, we also found that the best-fit parallax model seemed not to explain the long-term deviations of the light curve from the best-fit static model, as can be seen in Figure 3.4. This implies that there might still be other high-order microlensing effects in the light curve. Note that adding the lens orbital motion does not improve our models.

Xallarap Effects

Xallarap (Griest & Safizadeh, 1998b; Han & Gould, 1997; Poindexter et al., 2005) is the microlensing effect on the light curve induced by the source orbital motion around the source companion. The xallarap model requires 7 additional fitting parameters which determine the orbital elements of the source system; the direction toward the solar system relative to the orbital plane of the source system, R.A.$_\xi$ and Dec.$_\xi$; the source orbital period, P_ξ; the source orbital eccentricity and perihelion time, e_ξ and $T_{\rm peri}$; the xallarap vector, $\boldsymbol{\xi}_{\rm E} = (\xi_{{\rm E},N}, \xi_{{\rm E},E})$. The direction of $\boldsymbol{\xi}_{\rm E}$ is similar to that of the geocentric lens-source proper motion $\boldsymbol{\mu}_{\rm rel,G}$ and the amplitude of $\boldsymbol{\xi}_{\rm E}$ is $\xi_{\rm E} = a_S/\hat{r}_{\rm E}$ where a_S is the semi-major axis of the source orbit and $\hat{r}_{\rm E}$ is the projected Einstein radius to the source plane, i.e., $\hat{r}_{\rm E} = \theta_{\rm E} D_S$. Kepler's third and Newton's third laws give the following relations (Batista et al., 2009),

$$\xi_{\rm E} = \frac{1\ {\rm au}}{D_S\theta_{\rm E}}\left(\frac{M_c}{M_\odot}\right)\left[\frac{M_\odot}{M_c + M_S}\frac{P_\xi}{1\ {\rm year}}\right]^{2/3}, \tag{3.3}$$

$$M_S a_S = M_C a_C \Rightarrow a_{SC} \equiv a_S + a_C = (1 + \frac{M_S}{M_C})a_S\ , \tag{3.4}$$

where M_S and M_C are the masses of the source and source companion, respectively. Therefore, we can estimate the source companion mass M_C from the xallarap measurements by assuming M_S and D_S.

Since the number of additional parameters for the xallarap effect is large, we conducted a grid search fixing $({\rm R.A.}_\xi, {\rm Dec.}_\xi, P_\xi)$ in order to avoid missing any local minima. After refining all the possible solutions, we found the best-fit xallarap model is favored over the best-fit parallax model by $\Delta\chi^2 > 650$. As shown in Figure 3.4, including the xallarap effect produces a model that fits the long-term residuals from the best-fit static model, and it dramatically improves the χ^2 values. The best-fit orbital period of the source system is $P_\xi \sim 40$ days and is clearly different from Earth's orbital period of 365 days, which implies that the parallax and xallarap signals are clearly distinguishable. Following Equation (3.3), the best-fit 2L1S xallarap model indicates a source companion mass of $M_C = 0.21 M_\odot$ and a distance between two sources $a_{SC} = 0.22$ au on the assumption of $M_S = 1.0 M_\odot$ and $D_S = 8$ kpc, which is a common stellar binary system in solar neighborhood (Duchêne & Kraus, 2013). The best-fit ξ_E values are much smaller than 1, which means that the two sources are separated by much less than the Einstein radius. Hence, the source companion was also likely to be magnified during the event. In following sections, we explore the binary source scenarios where both components of the binary source system are magnified by the lens.

3.3.3 Binary Source (1L2S) Model

When two source stars are magnified by the same single-lens, called a single-lens binary-source (1L2S) event, the observed flux would be the superposition of the two magnified single-source fluxes, i.e.

$$A(t) = \frac{A_1(t)F_{s,1} + A_2(t)F_{s,2}}{F_{s,1} + F_{s,2}} = \frac{A_1(t) + q_{F,j}A_2(t)}{1 + q_{F,j}} \ , \tag{3.5}$$

where A_i and $F_{s,i}$ represent the magnification and the baseline flux of each i-th source, and $q_{F,j} = F_{s,2}/F_{s,1}$ is the flux ratio between the two source stars in each j-th pass band. For a standard (static) 1L2S model, the fitting parameters are [t_0, $t_{0,2}$, t_E, u_0, $u_{0,2}$, ρ, ρ_2, $q_{F,j}$]. Because the magnification of each source star varies independently, the total observed source color is variable during a binary source event, which happens in single-source events only if limb-darkening effects are seen during caustic crossings[4] as microlensing does not depend on wavelength. Binary source events can mimic short-term binary-lens anomalies in a light curve, therefore it is necessary whether the anomaly features are induced by binary-lens or binary-source (Gaudi, 1998; Jung et al., 2017a,b; Shin et al., 2019).

First, we fitted the light curves with the static 1L2S model and found that it was disfavored over the static 2L1S models by $\Delta\chi^2 > 1100$. In Section 3.3.2, we found an asymmetric distortion in the light curves which can be explained by the xallarap effect (i.e. source orbital effect). Thus, we also explored 1L2S models with source orbital motion. The trajectories of two sources can be estimated by the source orbital motion from the xallarap parameters, $(\xi_{\mathrm{E},N}, \xi_{\mathrm{E},E}, \mathrm{R.A.}_\xi, \mathrm{Dec.}_\xi, P_\xi, e_\xi, T_\mathrm{peri})$, and Equation (3.3). Here, we assumed $M_S = 1\ M_\odot$ and $D_S = 8$ kpc to derive the source companion mass M_C. In Appendix A.2, we confirmed that the assumptions of $M_S = 1\ M_\odot$ and $D_S = 8$ kpc hardly impact on the light curve modeling. We conducted detailed grid search of $(\mathrm{R.A.}_\xi, \mathrm{Dec.}_\xi, P_\xi)$ and refined all the possible 1L2S solutions. We found the best-fit 1L2S model is not preferred over the static 2L1S models by $\Delta\chi^2 > 80$ even if we introduced the source orbital motion.

3.3.4 Binary-Lens Binary-Source (2L2S) Model

[4] For point lenses, this happens only if the lens briefly transits the source (Loeb & Sasselov, 1995; Gould & Welch, 1996)

Table 3.3: The 2L2S Model Parameters

Parameters	Units	Close ($s < 1$)		Wide ($s > 1$)	
		($u_0 > 0$)	($u_0 < 0$)	($u_c > 0$)	($u_c < 0$)
t_0 (t_c)	HJD-2456530	$7.3128^{+0.0005}_{-0.0005}$	$7.3127^{+0.0005}_{-0.0005}$	$7.3123^{+0.0003}_{-0.0004}$	$7.3111^{+0.0005}_{-0.0006}$
$t_{\rm E}$	day	$94.698^{+1.612}_{-1.525}$	$98.121^{+0.858}_{-0.958}$	$101.104^{+2.246}_{-1.799}$	$98.275^{+1.154}_{-1.148}$
u_0 (u_c)	(10^{-3})	$4.800^{+0.077}_{-0.079}$	$-4.620^{+0.041}_{-0.042}$	$4.522^{+0.086}_{-0.108}$	$-4.626^{+0.053}_{-0.053}$
q	(10^{-2})	$3.236^{+0.089}_{-0.084}$	$3.066^{+0.090}_{-0.094}$	$3.160^{+0.132}_{-0.134}$	$3.456^{+0.087}_{-0.067}$
s		$0.150^{+0.002}_{-0.002}$	$0.150^{+0.002}_{-0.002}$	$6.774^{+0.101}_{-0.085}$	$7.084^{+0.074}_{-0.064}$
α	radian	$4.197^{+0.004}_{-0.004}$	$2.078^{+0.006}_{-0.008}$	$4.198^{+0.007}_{-0.007}$	$2.092^{+0.006}_{-0.005}$
ρ	(10^{-3})	$1.113^{+0.148}_{-0.118}$	$1.136^{+0.090}_{-0.144}$	$1.413^{+0.093}_{-0.295}$	$0.971^{+0.118}_{-0.085}$
$\pi_{{\rm E},N}$		$0.256^{+0.044}_{-0.050}$	$0.300^{+0.027}_{-0.025}$	$0.319^{+0.039}_{-0.050}$	$0.271^{+0.032}_{-0.041}$
$\pi_{{\rm E},E}$		$0.018^{+0.005}_{-0.005}$	$0.004^{+0.006}_{-0.006}$	$0.001^{+0.006}_{-0.006}$	$0.006^{+0.003}_{-0.004}$
$\xi_{{\rm E},N}$	(10^{-3})	$-2.91^{+0.97}_{-1.01}$	$-3.13^{+1.72}_{-1.39}$	$-5.32^{+2.66}_{-1.61}$	$-2.48^{+1.28}_{-1.04}$
$\xi_{{\rm E},E}$	(10^{-3})	$-4.31^{+0.18}_{-0.17}$	$-3.59^{+0.62}_{-0.44}$	$-3.53^{+0.45}_{-0.48}$	$-3.66^{+0.50}_{-0.33}$
R.A.$_\xi$	degree	$-74.2^{+12.3}_{-12.2}$	$-87.4^{+15.5}_{-14.0}$	$260.9^{+13.5}_{-11.4}$	$-89.4^{+16.3}_{-16.3}$
Dec.$_\xi$	degree	$21.8^{+6.4}_{-7.4}$	$29.8^{+2.5}_{-3.5}$	$19.7^{+2.2}_{-6.2}$	$38.0^{+7.4}_{-7.7}$
P_ξ	day	$36.67^{+0.77}_{-0.73}$	$36.28^{+0.74}_{-0.70}$	$36.82^{+0.66}_{-0.68}$	$36.51^{+0.80}_{-0.70}$
e_ξ		$0.258^{+0.033}_{-0.029}$	$0.249^{+0.029}_{-0.031}$	$0.270^{+0.032}_{-0.029}$	$0.231^{+0.040}_{-0.038}$
$T_{\rm peri}$	HJD-2456500	$53.14^{+1.08}_{-1.10}$	$52.75^{+0.48}_{-0.51}$	$17.31^{+0.90}_{-0.84}$	$53.69^{+0.78}_{-0.96}$
$q_{F,Red}$	(10^{-3})	$1.122^{+0.388}_{-0.330}$	$0.818^{+0.317}_{-0.254}$	$0.974^{+0.439}_{-0.298}$	$0.970^{+0.342}_{-0.261}$
$q_{F,I}$	(10^{-3})	$1.424^{+0.466}_{-0.399}$	$1.058^{+0.383}_{-0.309}$	$1.246^{+0.527}_{-0.362}$	$1.241^{+0.412}_{-0.317}$
$q_{F,V}$	(10^{-4})	$3.58^{+1.58}_{-1.29}$	$2.39^{+1.24}_{-0.93}$	$3.00^{+1.76}_{-1.12}$	$2.98^{+1.36}_{-0.99}$
$q_{F,R}$	(10^{-4})	$6.62^{+2.64}_{-2.18}$	$4.61^{+2.10}_{-1.62}$	$5.63^{+2.96}_{-1.93}$	$5.60^{+2.30}_{-1.70}$
$\pi_{\rm E}$		$0.257^{+0.044}_{-0.050}$	$0.300^{+0.027}_{-0.025}$	$0.319^{+0.039}_{-0.050}$	$0.271^{+0.032}_{-0.041}$
χ^2		16542.2	16543.3	16542.3	16542.9
$\Delta\chi^2$		-	1.1	0.1	0.7

NOTE - Here, we assume $M_S = 1\ M_\odot$ and $D_S = 8$ kpc.

The flux ratios q_F and parallax amplitude $\pi_{\rm E} = \sqrt{\pi_{\rm E,N}^2 + \pi_{\rm E,E}^2}$ are not fitting parameters.

All the other parameters in this table are used as fitting parameters for modeling.

Finally, we explored the 2L2S models with source orbital motion, i.e., taking account the flux from the source companion and the xallarap effect. Here, we adopted the flux ratios q_F estimated from M_C which is derived from the xallarap parameters to keep the consistency. We derived the flux ratios in each band from a combination of M_C and a theoretical stellar isochrone model[5] (PARSEC; Bressan et al., 2012) for solar metallicity and a typical bulge star age of 10 Gyr. For the Unfiltered passband, we used the R-band flux ratio assuming $q_{F,{\rm Unfiltered}} \approx q_{F,R}$. For the MOA-Red band, we derived the flux ratio from that in I- and V- bands, $q_{F,Red} = q_{F,I}^{0.827} q_{F,V}^{0.173}$. This formula comes from the following color transformation that is derived by using bright stars around the event (Gould et al., 2010; Bennett et al., 2012, 2018),

$$R_{\rm MOA} - I_{\rm O3} = 0.173(V_{\rm O3} - I_{\rm O3}) + {\rm const}$$

[5]http://stev.oapd.inaf.it/cgi-bin/cmd

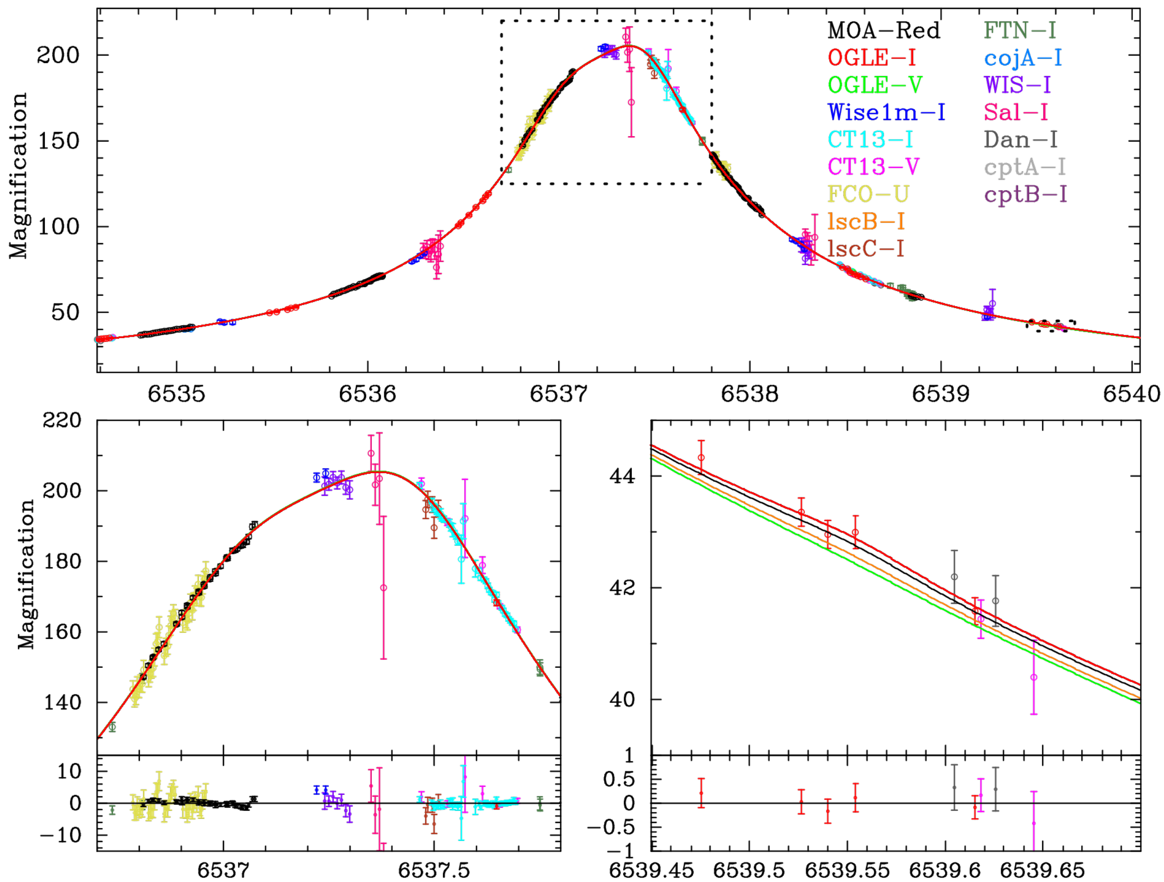

Figure 3.5 The light curve of OGLE-2013-BLG-0911. Each color on the data point corresponds to each instrument, shown on the right. The error bars are renormalized following Equation (3.1). The 2L2S ($s < 1$, $u_0 > 0$) model light curves in MOA-Red, I, V, Unfilered bands are shown as the solid black, red, green and orange lines, respectively. The dotted boxes in the top panel correspond to the areas represented in the bottom left and right panels, where the primary and secondary sources were significantly magnified, respectively.

where $R_{\rm MOA}$, $I_{\rm O3}$ and $V_{\rm O3}$ are the magnitudes in MOA-Red, OGLE-III I- and V-bands, respectively.

We found the four best 2L2S models, which suffer from the close/wide degeneracy and the ecliptic degeneracy. The parameters of these models are shown in Table 3.3. The light curve of the best-fit 2L2S ($s < 1$, $u_0 > 0$) model is shown in Figure 3.5. Here, as shown in Equation (3.5), the light curves in each passband are different. The black, red, green and cyan solid curves indicate the model light curves in the MOA-Red, I-, V- and R-bands, respectively. The caustic geometry and source trajectories of the best-fit 2L2S ($s < 1$, $u_0 > 0$) model are shown in Figure 3.6. Here the source companion trajectory indicates that the source companion is more strongly magnified than the primary source. In general, such magnification differences in two sources, allow us to resolve the close/wide degeneracy and the ecliptic degeneracy. However, as shown in the bottom right panel of

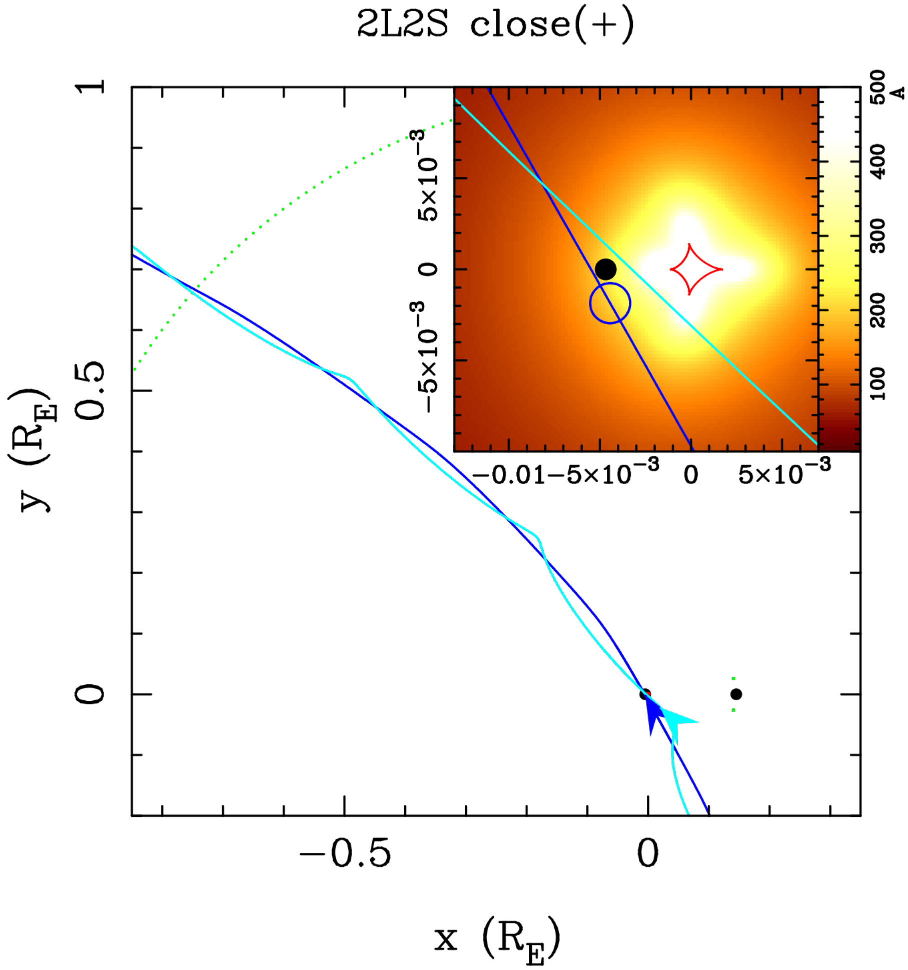

Figure 3.6 Caustic geometry for the best-fit 2L2S ($s < 1, u_0 > 0$) model is shown as the red curves, respectively. The blue and light blue curves show the primary and secondary source trajectories with respect to the lens systems, with the arrows indicating the directions of each source motion. The black dots are lens components and the green dots represent critical curves. The inset shows a zoom-in view around the central caustic. The magnification patterns are described as color maps. The brighter tone denotes higher magnification. The blue circle on the lines indicates the primary source size and its positions is at t_0.

Figure 3.5, where the secondary source magnification is peaked at HJD'$\sim$ 6539.55 , the flux contribution is $\sim$ 0.01 times smaller than the primary source because the source companion is intrinsically much fainter than the primary source. Consequently, we could not resolve these degeneracies. These 2L2S models are preferred relative to the 2L1S models with parallax and xallarap effects by $\Delta\chi^2 \sim 16$ without additional fitting parameters. The fitting and physical parameters for the 2L1S and 2L2S models are almost identical each other. Therefore, it hardly affects the final results whichever we take. Hereafter, we take the 2L2S models for the final result.

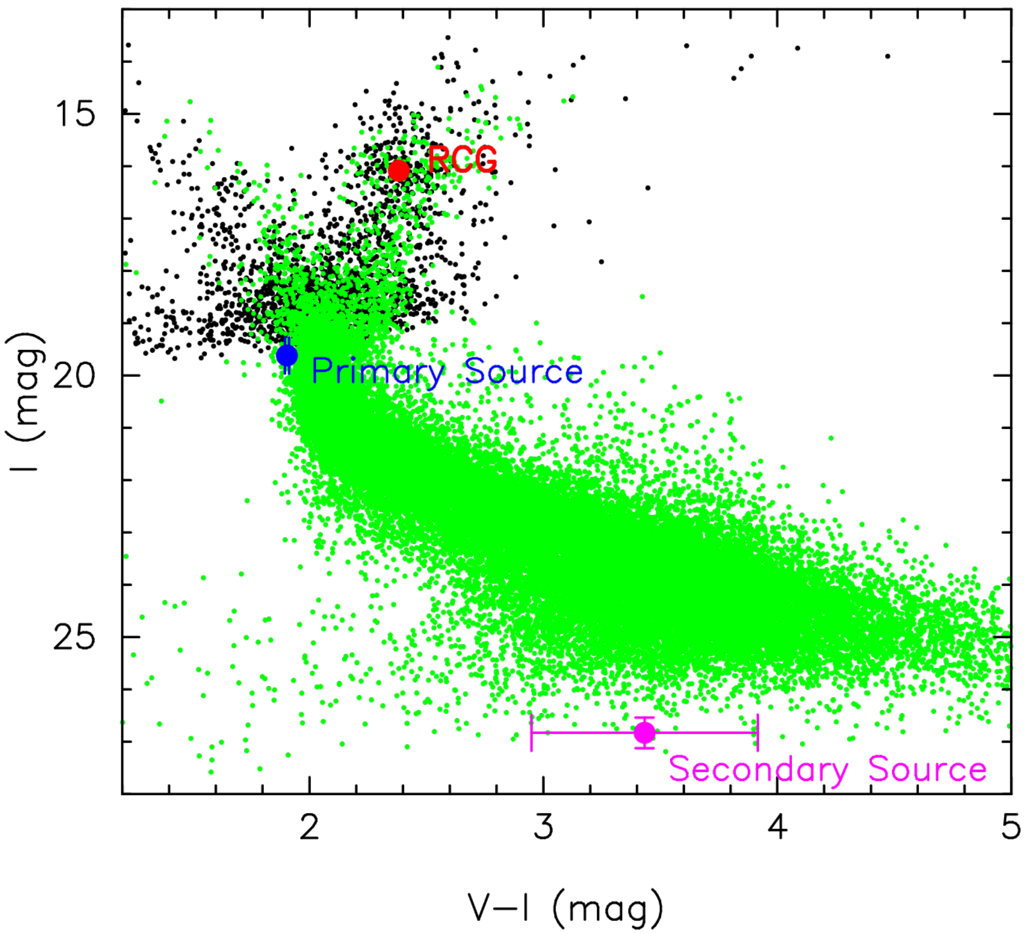

Figure 3.7 The $(V-I, I)$ color magnitude diagram (CMD) in the standard Kron-Cousins I and Johnson V photometric system. The positions of the primary and secondary source and the centroid of RCG are represented as the blue, magenta and red circles. The black dots indicate the OGLE-III catalog stars within $1'$ of the source. The green dots indicate the *Hubble Space Telescope* CMD in Baade's window (Holtzman et al., 1998) whose color and magnitude are matched by using the RCG position.

3.4 Source Properties

The measurement of ρ enables us to determine the angular Einstein radius $\theta_{\rm E} = \theta_*/\rho$ where θ_* is the angular source radius. The angular source radius θ_* can be estimated from the extinction-free color and magnitude of the source star by using a method similar to that of Yoo et al. (2004) which adopts the centroid of the bulge red clump giants (RCG) as a reference point. Yoo et al. (2004) assumed that the source star suffers from the same extinction as that of the bulge RCG so that the extinction-free color and magnitude of the source star can be described as the following equation,

$$(V-I, I)_{S,0} = (V-I, I)_{0,\rm RCG} - \Delta(V-I, I) \ , \tag{3.6}$$

where $(V-I, I)_{0,\mathrm{RCG}} = (1.06\pm0.07, 14.40\pm0.04)$ is the extinction-free color and magnitude of the bulge RCG centroid (Bensby et al., 2011, 2013; Nataf et al., 2013) and $\Delta(V-I, I)$ are the offsets of the color and magnitude from the RCG centroid to the source star measured in the standard color magnitude diagram (CMD).

Table 3.4: The Source Properties

	$V-I$(mag)	I(mag)	θ_*(μas)
apparent	1.904 ± 0.009	19.618 ± 0.006	-
intrinsic	0.714 ± 0.071	18.104 ± 0.049	0.757 ± 0.054
	From Bensby et al. (2017)		
Effective Temperature (K)	T^a_{eff}	5785 ± 77	
	T^b_{eff}	6616	
Source Color (mag)	$(V-I)^a_{S,0}$	$0.71^{+0.03}_{-0.02}$	
	$(V-I)^b_{S,0}$	0.49	
Absolute Magnitude (mag)	M^a_V	3.69	
Heliocentric Radial Velocity (km/s)	$\mathrm{RV}_{\mathrm{helio}}$	-46.8	

NOTE - Bensby et al. (2017) modeled OGLE-2013-BLG-0911 as a 1L1S event.
[a] Derived from spectroscopy.
[b] Derived from their microlensing model.

3.4.1 Photometric Source Properties

We obtained the apparent source color and magnitude of $(V-I, I)_S = (1.904 \pm 0.008, 19.618 \pm 0.006)$ derived from the measurements of CT13-I and V in the light curve modeling, which is detailed in Appendix A.1. We also derived the source color and magnitude from the measurements of OGLE-I and V and confirmed that they are consistent within 2σ, which is also detailed in Appendix A.1. In addition, we independently measured the source color using a linear regression from CT13-I and V, $(V-I)_{\mathrm{CT13,reg}} = 1.910 \pm 0.005$, which is consistent with $(V-I)_S$. Therefore, we judged the measurements of the source color and magnitude are robust. Here, we took the source color and magnitude derived from the CT-13 measurements because both CT13-I and -V covered the light curve well when the primary source were significantly magnified.

Figure 3.7 shows the CMD of the OGLE-III catalog within $60''$ of the sources plotted as black dots, and the CMD of Baade's window from Holtzman et al. (1998) plotted as green dots. We found that the extinction-free color and magnitude of the primary source star are $(V-I, I)_{S,0} = (0.582\pm0.071, 17.936\pm0.049)$ assuming that the source suffers from the same extinction of the RCG centroid of $(E(V-I), A_I)_{\mathrm{RCG}} = (1.322\pm0.071, 1.682\pm0.049)$. The primary and secondary source stars are represented as blue and magenta dots in Figure 3.7. The primary source star seems to be somewhat bluer and brighter than other typical bulge dwarfs, which implies that the source possibly suffered less from reddening and extinction than the bulge RCG centroid.

3.4.2 Spectroscopic Source Properties

Bensby et al. (2017) took a spectrum of OGLE-2013-BLG-0911S and reported the source properties in detail, which are summarized in Table 3.4[6]. They suggested a possibility that the source star belongs to the foreground Galactic disk for three reasons. First, they measured the lens-source relative proper motion of $\mu \sim 0.3$ mas/yr based on their single-lens microlensing model and indicated that this small value preferred the foreground disk source. Second, the intrinsic source color $(V-I)_{S,0} = 0.71^{+0.03}_{-0.02}$ based on their spectroscopic measurement is redder than $(V-I)_{S,0} = 0.49$ from their microlensing analysis, which implies that the source suffers less extinction than the average RCG in this field. They suggested that this may be because the source is in the foreground disk. Note that our derived $(V-I)_{S,0}$ assuming the source is behind all of the dust, is less blue (0.58 vs. 0.49), but is still substantially bluer than Bensby's spectroscopic value. Third, they claimed that the heliocentric radial velocity of the source, $\mathrm{RV_{helio}}$, is consistent with a disk star.

However, if we adopt $I_{S,0} = 17.94$ which is derived from our light curve modeling and the absolute source magnitude $M_I = 2.98$ which is estimated from spectroscopic values in Bensby et al. (2017), these measurements yield a source distance of ~ 9.8 kpc, which would put the source within or behind the bulge. Furthermore, we consider that the above rationale for the disk source scenario is not strong for three reasons. First, both our 2L2S and 2L1S models provided $\mu \sim 3$ mas/yr which does not strongly favor the foreground disk source. It is likely that their 1L1S model which could not fit the light curve properly, derived the incorrect values of $\mu \sim 0.3$ mas/yr and $(V-I)_{S,0} = 0.49$. Second, the color of $(V-I)_{S,0} = 0.58 \pm 0.07$ derived in our analysis is between their spectroscopic and microlensing values and we found a similar color with their microlensing value when we use RCGs in slightly wider area around the target, where the RCG distribution gets spread wider along the extinction vector on the CMD. These indicate that their spectroscopic color $(V-I)_{S,0} = 0.71^{+0.03}_{-0.02}$ is correct and their and our photometric color $(V-I)_{S,0} = 0.49$ and 0.58 ± 0.07, respectively, which are based on the average color of RCG in wider area, are biased because of low spatial resolution relative to the actual spacial variation of the reddening. Therefore, we conclude that the color difference may be due to the local spatial variation of the extinction in this field rather than the foreground disk scenario. Third, the constraint from $\mathrm{RV_{helio}}$ is not strong because it is also sufficiently explained by the bulge velocity distribution which has a large dispersion of $\sigma \sim 100$ km/s (Howard et al., 2008).

Finally, we adopt 90% of the RCG extinction as the source extinction, i.e., $(E(V-I), A_I)_S = 0.9 \times (E(V-I), A_I)_{\mathrm{RCG}} = (1.190 \pm 0.064, 1.514 \pm 0.044)$ and thus the intrinsic primary source color and magnitude are $(V-I, I)_{S,0} = (0.714 \pm 0.071, 18.109 \pm 0.049)$. This is consistent with the spectroscopic source color $(V-I)_{S,0} = 0.71^{+0.03}_{-0.02}$. Note that even if we assumed that the source suffered from the same extinction as that for average RCG,

[6]http://cdsarc.u-strasbg.fr/viz-bin/qcat?J/A+A/605/A89

the estimated source angular radius θ_* is consistent with that with 90% of the average RCG extinction. The source properties are summarized in Table 3.4.

3.4.3 Angular Source and Einstein Radius

With the extinction-free color and magnitude of the source, we can estimate θ_* from a precise empirical $(V-I)$ and I relation

$$\log_{10}\left(\frac{2\theta_*}{\mathrm{mas}}\right) = 0.5014 + 0.4197(V-I)_{S,0} - 0.2I_{S,0} \ , \tag{3.7}$$

which is the optimized relation for the color ranges of microlensing observation, derived from the extended analysis of Boyajian et al. (2014). Using Equation (3.7), we estimated $\theta_* = 0.757 \pm 0.054$ μas for the best-fit model. We used Equation (3.7) and took account of the source extinction and its uncertainty into our MCMC calculations to derive the angular Einstein radius θ_{E} and the geocentric lens-source relative proper motion $\mu_{\mathrm{rel,G}}$ for each model. The results are summarized in Table 3.5.

3.5 Lens System Properties

The measurements of both θ_{E} and π_{E} enable us to determine the lens mass M_L and distance D_L directly (Gould, 2000; Bennett, 2008) as follows

$$M_L = \frac{c^2}{4G}\theta_{\mathrm{E}}^2\frac{D_S D_L}{D_S - D_L} = \frac{c^2}{4G}\frac{\mathrm{au}}{\pi_{\mathrm{E}}^2}\frac{D_S - D_L}{D_S D_L} = \frac{\theta_{\mathrm{E}}}{\kappa\pi_{\mathrm{E}}} \ , \tag{3.8}$$

where D_L is the lens distance. We derived the probability distributions of the physical parameters of the source and lens systems by calculating their values in each MCMC link. Here, we assumed the primary source mass $M_S = 1M_\odot$ and the source distance $D_S = 8$ kpc. As referred in Appendix A.2, we confirmed that the assumptions hardly affect the MCMC posterior distributions for the lens physical parameters except for the lens distance D_L. We combined the posterior probability distributions of each model weighting by $e^{-\Delta\chi^2/2}$. Figure 3.8 shows the probability distributions of the lens mass M_L and distance D_L for the close and wide models, and the result is summarized in Table 3.5. The result indicates that the lens system is an M-dwarf orbited by a massive Jupiter companion at very close ($M_{\mathrm{host}} = 0.30^{+0.08}_{-0.06}M_\odot$, $M_{\mathrm{comp}} = 10.1^{+2.9}_{-2.2}M_{\mathrm{Jup}}$, $a_{\mathrm{exp}} = 0.40^{+0.05}_{-0.04}$au) or wide ($M_{\mathrm{host}} = 0.28^{+0.10}_{-0.08}M_\odot$, $M_{\mathrm{comp}} = 9.9^{+3.8}_{-3.5}M_{\mathrm{Jup}}$, $a_{\mathrm{exp}} = 18.0^{+3.2}_{-3.2}$au) separation.

We evaluated the expected apparent magnitude of the lens brightness by conducting a Bayesian analysis based on the observed t_{E}, θ_{E} and π_{E} and prior probabilities from a standard Galactic model (Sumi et al., 2011). Here, we evaluated the extinction in front of the lens by

$$A_{i,L} = \frac{1 - e^{-D_L/h_{\mathrm{dust}}}}{1 - e^{-D_S/h_{\mathrm{dust}}}}A_{i,S}, \tag{3.9}$$

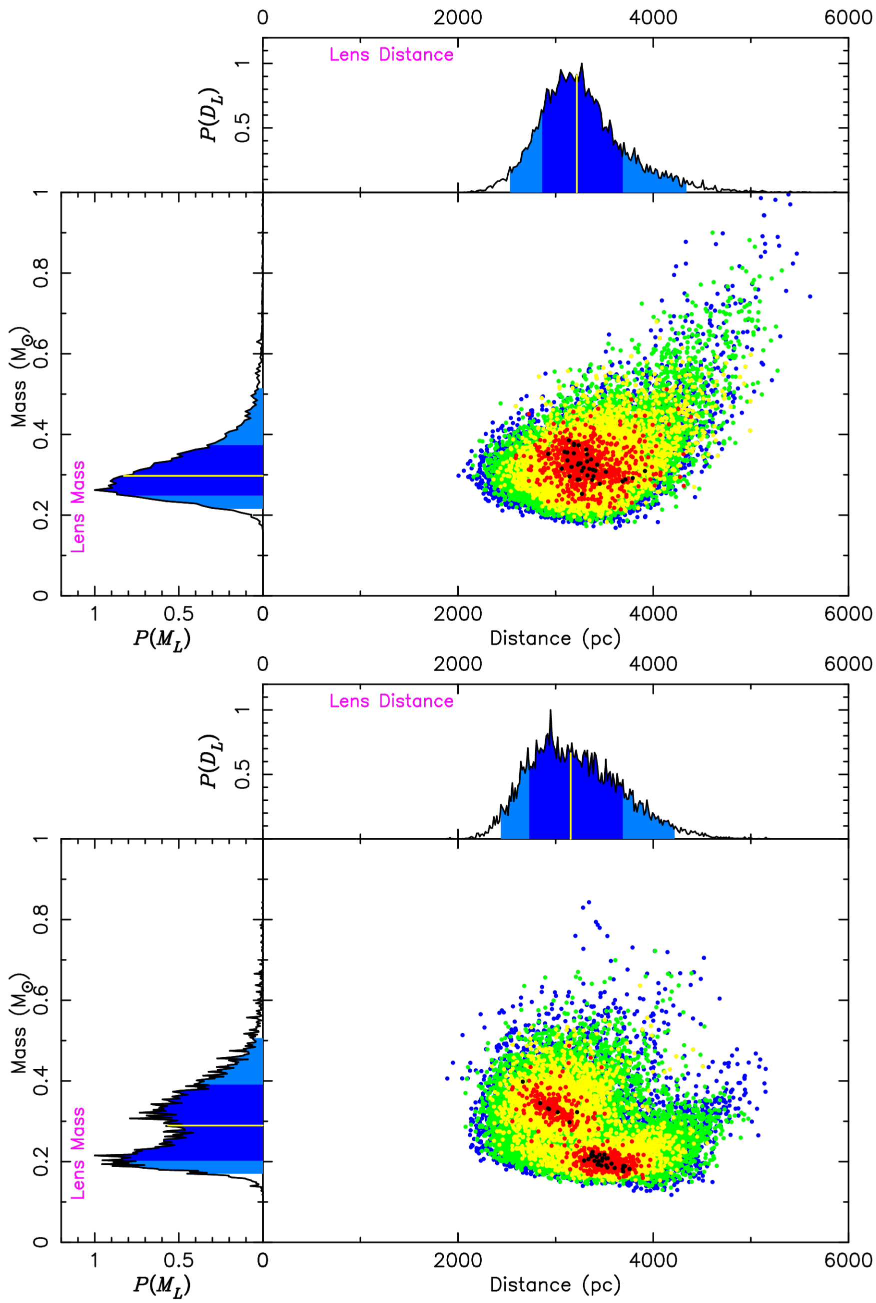

Figure 3.8 The main panel shows $\Delta\chi^2$ distribution of the lens mass M_L and distance D_L for the close (upper) and wide (bottom) models derived from MCMC, where black, red, yellow, green and blue dots indicate links with $\Delta\chi^2 < 1$, 4, 9, 16 and 25, respectively. Top and left insets represent the posterior probability distributions of M_L and D_L, where the dark and light blue regions indicate the 68.3% and 95.4% credible interval, and the perpendicular yellow lines indicate the median values.

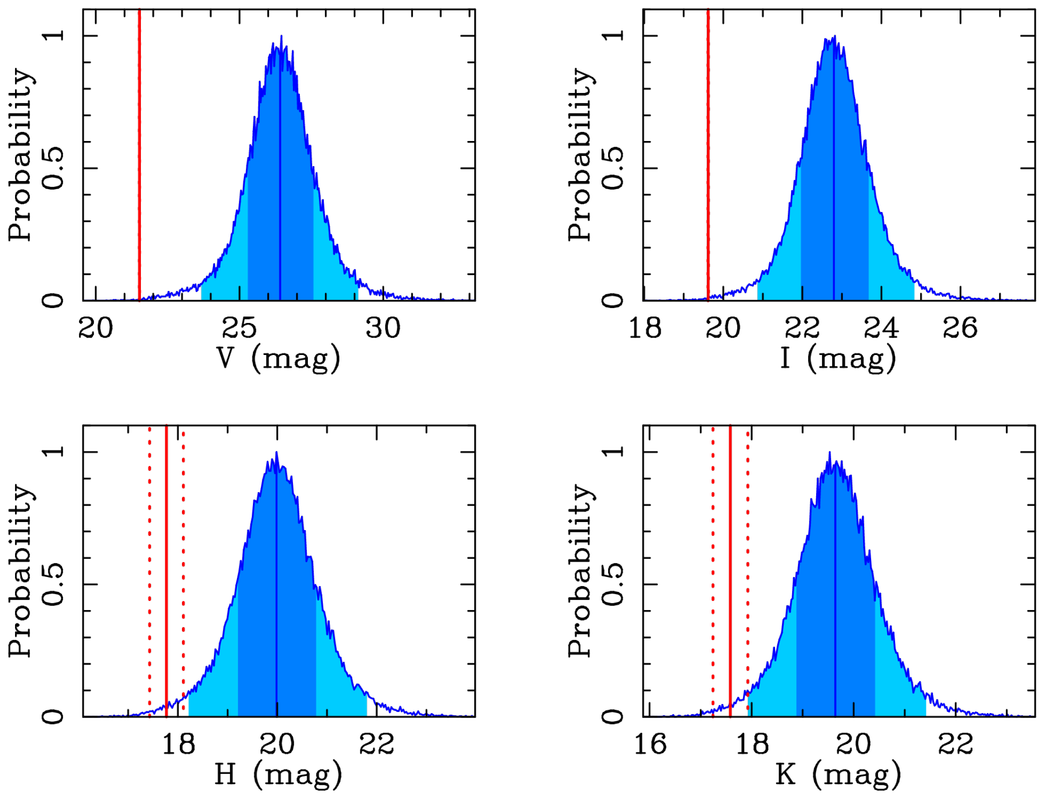

Figure 3.9 Posterior probabilities of the lens apparent magnitudes derived from the Bayesian analysis with the observed $t_{\rm E}$, $\theta_{\rm E}$ and $\pi_{\rm E}$ and prior probabilities from a standard Galactic model. The dark and light blue regions indicate the 68.3% and 95.4% credible interval, and the vertical blue lines indicate the median values. The vertical solid and dashed red lines are the source magnitudes and its 1σ uncertainties in each passband.

where the index i corresponds to the passband V, I, H and K, and the $h_{\rm dust} = (0.1~{\rm kpc})$ $/\sin|b|$ is a scale length of the dust toward the event (Bennett et al., 2015). The lens brightness and the extinction values are estimated from the color-color and mass-luminosity relations of main sequence stars (Henry & McCarthy, 1993; Kenyon & Hartmann, 1995; Kroupa & Tout, 1997) and the extinction law in Nishiyama et al. (2009), respectively. We also estimated the source magnitudes in H- and K-bands from Kenyon & Hartmann (1995) with taking account of 10% uncertainty.

Figure 3.9 represents the apparent lens magnitudes in each band derived from the Bayesian analysis. The dark and light blue regions indicate the 16th and 84th percentile and the vertical blue lines indicate the median values. The vertical solid and dashed red lines are the source magnitudes and its 1σ uncertainties in each passband. The relationship between the heliocentric and geocentric relative proper motion is

$$\boldsymbol{\mu}_{\rm rel,H} = \boldsymbol{\mu}_{\rm rel,G} + \frac{\pi_{\rm rel}}{\rm au}\boldsymbol{v}_{\oplus} \tag{3.10}$$

where $\pi_{\rm rel} = {\rm au}(D_L^{-1} - D_S^{-1})$ and $\boldsymbol{v}_{\oplus} = (v_{\oplus,N}, v_{\oplus,E}) = (-2.91, 9.44)~{\rm km~s^{-1}}$ are the relative lens-source parallax and the instant velocity of Earth on the plane of the sky at the reference time, respectively. The heliocentric relative proper motion is $\mu_{\rm rel,H} \sim 2.5$ mas yr^{-1} and thus the angular separation between the source and lens would be ~ 15 mas in 2019. Bhattacharya et al. (2017) have demonstrated the feasibility of *Hubble Space Telescope* follow-up observations to measure the separation between the source and the lens with 12 mas when the lens is not too much fainter than the source (The current state of technical arts for high angular resolution analysis is detailed in Bhattacharya et al. (2018)). Hence, it might benefit from a high-resolution follow-up observation in order to constrain the physical parameters of the lens system. However, we note that the four degenerate solutions have parallax vectors $\boldsymbol{\pi}_{\rm E}$ with amplitudes, directions and uncertainties approximately similar to each other and thus it is unlikely that the degenerate solutions are resolved by high-resolution follow-up observations.

Table 3.5: Physical Parameters

Parameters	Units	Close	Wide
Lens Host Mass, $M_{\rm host}$	$M_\odot$	$0.29^{+0.07}_{-0.05}$	$0.28^{+0.10}_{-0.08}$
Lens Companion Mass, $M_{\rm comp}$	$M_{\rm Jup}$	$9.51^{+2.72}_{-1.69}$	$9.92^{+3.78}_{-3.45}$
Lens Distance, D_L	kpc	$3.22^{+0.47}_{-0.35}$	$3.15^{+0.53}_{-0.42}$
Expected Semi-major Axis, $a_{\rm exp}{}^1$	au	$0.39^{+0.05}_{-0.03}$	$17.98^{+3.21}_{-3.24}$
Source Companion Mass, M_C	$M_\odot$	$0.137^{+0.018}_{-0.016}$	$0.137^{+0.017}_{-0.014}$
Distance between Sources, a_{SC}	au	$0.225^{+0.004}_{-0.004}$	$0.225^{+0.003}_{-0.003}$
Angular Einstein Radius, $\theta_{\rm E}$	mas	$0.67^{+0.10}_{-0.08}$	$0.68^{+0.14}_{-0.17}$
Geocentric Lens-Source Proper Motion, $\mu_{\rm rel,G}$	mas/yr	$2.54^{+0.37}_{-0.30}$	$2.50^{+0.56}_{-0.65}$
Predicted Lens Magnitude, V_L	mag	$26.42^{+1.15}_{-1.13}$	
Predicted Lens Magnitude, I_L	mag	$22.80^{+0.88}_{-0.83}$	
Predicted Lens Magnitude, H_L	mag	$19.99^{+0.79}_{-0.78}$	
Predicted Lens Magnitude, K_L	mag	$19.64^{+0.78}_{-0.76}$	

NOTE - The median value and 68.3% credible interval derived from MCMC.
Here, we assume $D_S = 8$ kpc and $M_S = 1 M_\odot$ except for the lens magnitudes.
$^1 a_{\rm exp} = \sqrt{3}/2 a_\perp$.

3.6 Summary & Discussion

We have presented the analysis of the microlensing event OGLE-2013-BLG-0911. The previous research on the event (Shvartzvald et al., 2016) reported that the lensing anomaly could be explained by a planetary mass ratio, $q \approx 3 \times 10^{-4}$. From a detailed grid search analysis, however, we found that a binary mass ratio $q \approx 3 \times 10^{-2}$ is preferred over a planetary mass ratio to explain the light curve. Finally, we conclude that the lens system is an M-dwarf orbited by a massive Jupiter companion at very close ($M_{\rm host} = 0.30^{+0.08}_{-0.06} M_\odot$, $M_{\rm comp} = 10.1^{+2.9}_{-2.2} M_{\rm Jup}$, $a_{\rm exp} = 0.40^{+0.05}_{-0.04}$au) or wide ($M_{\rm host} = 0.28^{+0.10}_{-0.08} M_\odot$,

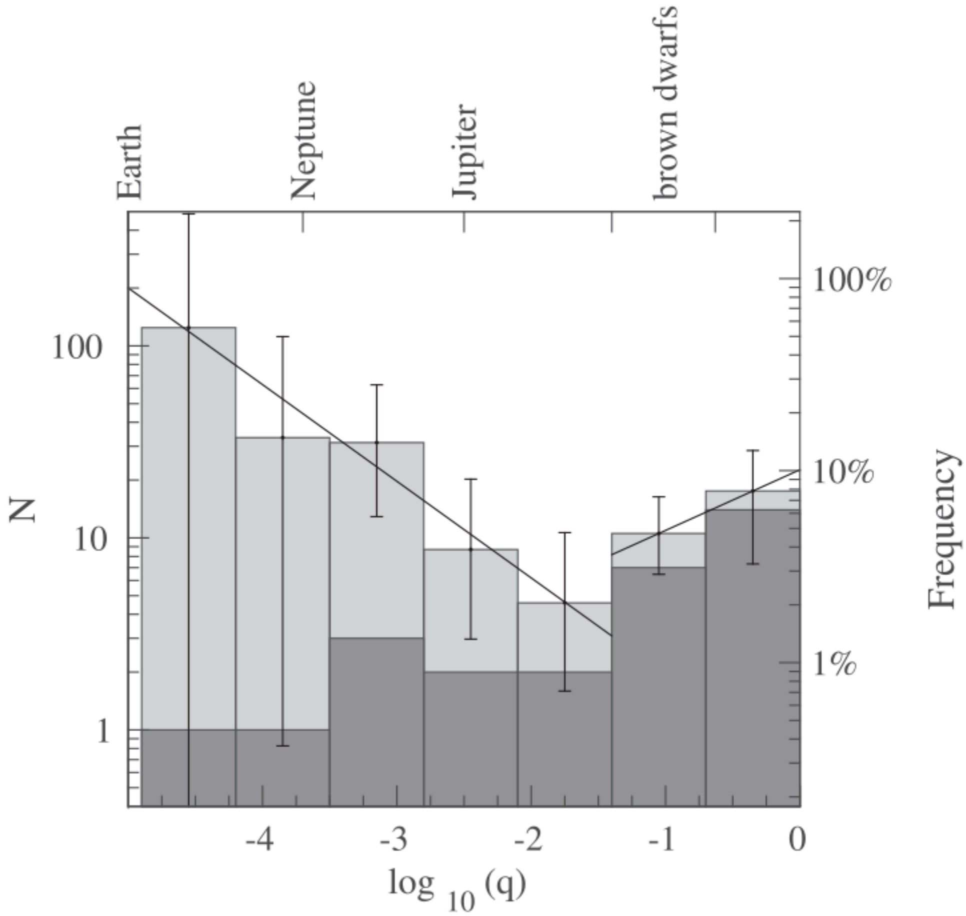

Figure 3.10 The mass-ratio distribution of microlensing companions analyzed in Shvartzvald et al. (2016). Solid lines are power-laws, $d\log f/d\log q = -0.50 \pm 0.17$ in $\log(q) < -1.4$ and $d\log f/d\log q = 0.32 \pm 0.38$ in $\log(q) > -1.4$. The dark-gray histogram represents their sample used in the analysis. The gray histogram represents the detection-efficiency-corrected distribution. From Shvartzvald et al. (2016) by permission of ESO and D. Suzuki who is one of the coauthors.

$M_{\rm comp} = 9.9^{+3.8}_{-3.5} M_{\rm Jup}$, $a_{\rm exp} = 18.0^{+3.2}_{-3.2}$au) separation.

Microlensing light curves generally provide much more precise estimation of the mass ratio rather than that of the absolute lens mass. Bond et al. (2004) defined the mass ratio boundary between BDs and planets as $q = 0.03$ in order to distinguish planetary and stellar binary (including BD) microlensing events. For this event, the best-fit mass ratio is slightly above the mass ratio boundary of $q = 0.03$. On the other hand, the median mass of the companion is slightly below the lower limit of BD mass of $13 M_{\rm Jup}$. Therefore, it is ambiguous to classify the companion as a BD or a planet. In fact, these boundaries are somewhat arbitrary and it might be nonsense to classify such an ambiguous companion according to the boundaries. However, the formation mechanisms for BDs and planets are likely to be different and the object near the boundaries could have been formed by either formation mechanism. Therefore, it would be very important to probe the distribution of intermediate mass companions of $\sim 13 M_{\rm Jup}$.

Missing the best lens model explanation to the observed microlensing light curve data might have serious impacts on any statistical microlensing analysis incorporating those modeling results. For instance, Shvartzvald et al. (2016) suggests that there is a possible BD deficit corresponding to $q \sim 10^{-2}$ in their detection-efficiency-corrected mass ratio function. However, we found OGLE-2013-BLG-0911, which was adopted as a planetary sample in their analysis, would correspond to the position of the BD deficit, which would affect their result to some extent (see Figure 3.10). The reason why they missed the best solution would be the very small/wide projected separation $s \approx 0.2$ or ≈ 7. They explored the s parameter space of $0.3 < s < 3$ in their grid search analysis. It is known that a central caustic size is approximately proportional to not only q but also s^2 (for $s \ll 1$) and s^{-2} (for $s \gg 1$) (Chung et al., 2005). Therefore, when we model microlensing light curves with perturbations caused by possibly small-size central caustics, we should suspect the possibilities of not only very low-mass but also very close and wide lens companions. The detection efficiency for companions with such extremely close and wide separation is much lower than that with $s \approx 1$ (Suzuki et al., 2016). Hence, even a small number of detections may be important in the statistical analysis.

The successful discovery of the best fit model depends on the initial parameters for the MCMC fitting. Currently, the initial parameters for modeling binary-lens events are mainly based on the experiences of the modelers or the brute-force with the grid search analysis across the wide range of the parameter spaces. The systematic analysis of many events relies on the latter method. However, it would not work if the best-fit solutions are out of range of the grid search, which happened on this event OGLE-2013-BLG-0911. Broadening the search range as possible is a straightforward way to avoid the problem. However, it is computationally expensive and it is getting more difficult for statistical analysis including hundreds of stellar binary events in the recent high cadence surveys by MOA, OGLE and KMTNet (Kim et al., 2016). Furthermore, the *Nancy Grace Roman Space Telescope* (e.g., Spergel et al., 2015) will be launched in 2025 and be expected to discover $\sim$ 54000 microlensing events ($|u_0| < 3$) with thousands of binary lens events including $\sim$ 1400 bound exoplanets with masses of $0.1 < M_p/M_\oplus < 10^4$ (Penny et al., 2019). We should consider a new method to efficiently search for the best binary-lens solutions. Bennett et al. (2012) applied the different parameterization for the wide-separate binary events. Khakpash et al. (2019) proposed the algorithm that can rapidly evaluate many binary-lens light curves and estimate the physical parameters of the lens systems, which is successful for very low mass-ratio events but less for higher mass-ratio events.

There are only four discoveries of BD companions to M dwarfs within 10 pc from Solar system (Winters et al., 2018), while approximately 200 M dwarfs are known to exist within 10 pc (Henry et al., 2006, 2016) and much effort has been dedicated to detect such BD companions (Henry & McCarthy, 1990; Dieterich et al., 2012). Because of their scarcity, incoming new BD discoveries around M dwarfs provide valuable constraints on the formation and evolution theories of stars, BDs and planets. Microlensing is a powerful method to probe the BD/massive-planet occurrence frequency across orbital radii $0.1 \leq a \leq 10$ au around low-mass hosts such as M dwarfs and even BDs (Gaudi, 2002), which is challenging for other exoplanet detection methods. Although microlensing samples generally can not provide some information such as host metallicity and eccentricity, microlensing can provide both thier masses and orbital separations. It is very important to uncover the distributions of BD properties by microlensing.

Chapter 4

Revealing Short-period Exoplanets and Brown Dwarfs in the Galactic Bulge using the Microlensing Xallarap Effect with the *Nancy Grace Roman Space Telescope*

The *Nancy Grace Roman Space Telescope* (*Roman*) will provide an enormous number of microlensing light curves with much better photometric precisions than ongoing ground-based observations. Such light curves will enable us to observe high-order microlensing effects which have been previously difficult to detect. In this chapter, we investigate *Roman*'s potential to detect and characterize short-period planets and brown dwarfs (BDs) in source systems using the orbital motion of source stars, the so-called xallarap effect. We analytically estimate the measurement uncertainties of xallarap parameters using Fisher matrix analysis. We show that the *Roman* Galactic Exoplanet Survey (RGES) can detect warm Jupiters with masses down to 0.5 $M_{\rm Jup}$ and orbital periods of 30 days via the xallarap effect. Assuming a planetary frequency function from Cumming et al. (2008), we find *Roman* will detect $\sim$ 10 hot and warm Jupiters and $\sim$ 30 close-in BDs around microlensed source stars during the microlensing survey. These detections are likely to be accompanied by the measurements of the companion's masses and orbital elements, which will aid in the study of the physical properties for close-in planet and BD populations in the Galactic bulge.

4.1 Introduction

Gravitational microlensing (Mao & Paczynski, 1991; Bennett & Rhie, 1996) has a unique sensitivity to low-mass exoplanets beyond the snow line (Hayashi et al., 1985) where planet formation is considered active by the enhanced surface density of solid materials. It has maximum sensitivity to planets (around the lens objects) with projected semi-major axes roughly equal to the projected Einstein ring radius $R_{\rm E}$, where

$$R_{\rm E} = \left(\frac{4GM_L}{c^2} \frac{D_L D_{LS}}{D_S} \right)^{1/2}. \tag{4.1}$$

Here D_S and D_L are the distances of the source and lens from the Earth, M_L is the mass of the lens, and $D_{LS} = D_S - D_L$. For typical microlensing events toward the Galactic bulge ($D_S = 8$ kpc, $D_L = 4$ kpc, $M_L = 0.3\ M_\odot$), $R_{\rm E}$ is ~ 2.3 au. Using this "binary-lens" channel of microlensing, the *Nancy Grace Roman Space Telescope* (Spergel et al., 2015, previously named *WFIRST*, hereafter *Roman*) will conduct the *Roman* Galactic Exoplanet Survey and discover $\sim$ 1400 cold wide-orbit exoplanets (Penny et al., 2019, hereafter P19) and provide an otherwise-inaccesible statistical sample of exoplanets in previously un-probed regions of exoplanet parameter space (see Figure 9 of P19).

Roman will observe many thousands of microlensing light curves which will generally have better photometric precision than many ground-based microlensing surveys. This will enable the measurement of high-order microlensing effects which have been previously difficult to detect. One of the high-order effects that can be measurable in the *Roman* light curves is xallarap (Griest & Safizadeh, 1998b; Han & Gould, 1997; Poindexter et al., 2005). Xallarap is a microlensing effect where the reflex motion of a source star in a binary system modulates the magnification of the source star. A more commonly known microlensing effect, orbital microlens parallax (Gould, 2004), also causes the variations with the same mechanism by the orbital motion of an observer.[1] The xallarap amplitude $\xi_{\rm E}$ corresponds to the semi-major axis of the source star a_S normalized by the angular Einstein radius $\theta_{\rm E}$ projected to the source plane, i.e.,

$$\xi_{\rm E} = \frac{a_S}{D_S \theta_{\rm E}} = \frac{a_S}{\hat{r}_{\rm E}}, \tag{4.2}$$

where $\hat{r}_{\rm E}$ is the projected Einstein radii. We note that a_S is the distance between the source and the center of masses of the source system. Using Newton's version of Kepler's third law, we can derive following equations from the Equation (4.2),

$$\begin{aligned} \xi_{\rm E} &= \frac{1\ \text{au}}{\hat{r}_{\rm E}} \left(\frac{M_P}{M_\odot} \right) \left[\frac{M_\odot}{M_S + M_P} \frac{P_\xi}{1\ \text{yr}} \right]^{2/3} \\ &\simeq 2 \times 10^{-5} \left(\frac{1\ \text{au}}{D_S \theta_{\rm E}} \right) \left(\frac{M_P}{M_{\rm Jup}} \right) \left[\frac{M_\odot}{M_S + M_P} \frac{1}{1} \frac{P_\xi}{1\ \text{day}} \right]^{2/3}, \qquad (4.3) \\ M_S a_S &= M_P a_P \\ \Rightarrow a &\equiv a_S + a_P = \left(1 + \frac{M_S}{M_P} \right) a_S, \qquad (4.4) \end{aligned}$$

where M_S and M_P are masses of the source (host) and source companion, P_ξ is the orbital period, a_P is the semi-major axis of the source companion, and a is the distance between the host and companion in the source system.

[1] Xallarap can be considered as the inverse of parallax and is a semordnilap.

Equation (4.3) means that when a solar-type source star in the Galactic bulge ($D_S =$ 8 kpc) is accompanied by a planet with $M_P = 10\ M_{\rm Jup}$ and $P_\xi = 10$ days, the angular size of the semi-major axis of the source star orbit around the barycenter is a factor 10^{-4} smaller than $\theta_{\rm E}$. Present ground-based microlensing survey observations do not have typical sensitivities to detect such small fluctuations induced by planetary-mass source companions.

In several microlensing analyses, xallarap has been investigated to explain light curve deviations from a standard model (Paczynski, 1986) which assumes uniform linear motions between the source, lens, and observers (e.g. Bennett et al., 2008; Sumi et al., 2016). However, identifying the xallarap signals clearly is rarely successful. For example, Sumi et al. (2010) analyzed a planetary microlensing event OGLE-2007-BLG-368 and found clear asymmetric features that can be interpreted as xallarap signals. However, they could not conclude it because possible unknown systematics in the light curve could not be ruled out. Recently, Miyazaki et al. (2020) identified a significant xallarap signal in a planetary microlensing event OGLE-2013-BLG-0911. Using the observed xallarap parameters, they concluded that there is a late M-dwarf orbiting the source star with a mass of $0.14^{+0.02}_{-0.02}\ M_\odot$ and an orbital period of $36.7^{+0.8}_{-0.7}$ days. This is the first demonstration that dark, low-mass objects in the Galactic bulge can be detected and characterized via xallarap even with ground-based photometry. Rahvar & Dominik (2009) suggested a possibility that planets orbiting sources in the Galactic bulge are detectable via xallarap with sufficiently good photometry. With space-based photometry like *Roman*, planetary-mass objects might be detectable and characterizable via xallarap.

In this chapter, we investigate the possibility of detecting planetary xallarap signals in the *Roman* microlensing events. In Section 4.2, we describe our Fisher matrix analysis and analytical quantification of the ability of the *Roman* light curves to detect xallarap signals and characterize the physical properties of the source systems. To predict how many planets are detectable in the *Roman* mission via the xallarap effect, we apply our analysis to simulations of the *Roman* survey in Section 4.3. Finally, we give our conclusion and discussion in Section 4.4.

4.2 Fisher Matrix Analysis

In this section, we conduct the Fisher matrix analysis based on the expected *Roman* observations and evaluate its sensitivity for xallarap. Rahvar & Dominik (2009) adopted the value of $\Delta\chi^2$ between the xallarap and non-xallarap (standard) models as the detection threshold of the source companion. However, it could be insufficient for evaluating the ability to characterize the physical parameters of planets. Further discussion on this is presented in Appendix B.1. The mechanisms of how xallarap affects light curves are essentially identical to the microlens parallax. Therefore, we conduct the Fisher matrix analysis by modifying the formulas of parallax that are conducted by Gould (2013), Mogavero & Beaulieu (2016, hereafter M16), and Bachelet et al. (2018, hereafter B18).

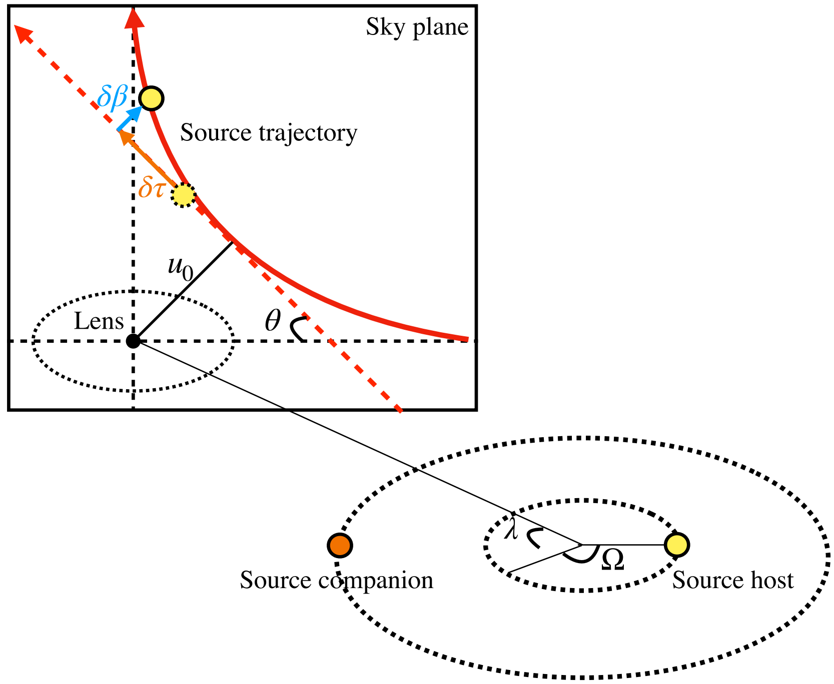

Figure 4.1 Schematic view of the xallarap problem. Due to the source orbital motion, the source trajectory (solid red curve) deviates from the inertial trajectory (dashed red line).

4.2.1 Parameterization of the Xallarap effect

Here we describe the xallarap effect observed by a single observatory. We follow B18's descriptions for the parallax effect observed by space-based observatories and then modify it for the case of xallarap effect.

In general, the observed flux of microlensing event is

$$F = F_S A + F_B = \overline{F}\left[(1-\nu)A + \nu\right] \tag{4.5}$$

where $F_S,\ F_B,\ \overline{F}(\equiv F_S+F_B)$ are the fluxes of the source, blend and baseline, respectively. $\nu \equiv F_B/(F_S+F_B)$ denotes the blend flux ratio[2]. For a single-lens single-source (1L1S) model, the source flux magnification A is described by

$$A(t) = \frac{u^2(t)+2}{u(t)\sqrt{u^2(t)+4}}, \tag{4.6}$$

where u is the magnitude of the lens-source separation vector normalized by the angular Einstein radius $\theta_{\rm E}$, $\boldsymbol{u}$. For uniform linear motions between the source, lens, and observers, $u(t) = \sqrt{\tau^2 + u_0^2}$, where $\tau \equiv (t-t_0)/t_{\rm E}$, t_0 is the time of the magnification peak, and u_0 is the lens-source impact parameter normalized to $\theta_{\rm E}$.

[2] $\overline{F}$ and ν are non-standard variables.

Figure 4.1 gives a schematic view of the xallarap problem. Here we consider a planet in a circular orbit ($e = 0$) around a source star with orbital period P_ξ and mass M_P. Then the source also orbits around the barycenter of the source system. In this chapter, we assume that the source companion contributes no flux to the event, i.e. it acts as a 1L1S event, not a binary source event (Han & Jeong, 1998). The displacement of the source position due to the orbital motion can be described by

$$\boldsymbol{S}(t) = \begin{pmatrix} s_1 \\ s_2 \end{pmatrix} = \begin{pmatrix} \cos\Omega - \cos\phi_\xi \\ \sin\lambda_\xi(\sin\Omega - \sin\phi_\xi) \end{pmatrix}, \tag{4.7}$$

where $\Omega = \omega(t - t_0) + \phi_\xi$ and $\omega = 2\pi/P_\xi$. Here, λ_ξ denotes the inclination of the source orbital plane with respect to the observer and ϕ_ξ denotes the orbital phase at t_0. We define θ as the angle between the direction of the lens-source relative motion and the major axis of the source orbit projected on the sky. When we define the xallarap vector $\boldsymbol{\xi}_{\rm E} = (\xi_{{\rm E},\parallel}, \xi_{{\rm E},\perp}) = \xi_{\rm E}(\cos\theta, \sin\theta)$, the displacement of the source position due to the orbit relative to the inertial source position is

$$\delta\tau = \boldsymbol{\xi}_{\rm E} \cdot \boldsymbol{S} \tag{4.8}$$

$$\delta\beta = \boldsymbol{\xi}_{\rm E} \times \boldsymbol{S}, \tag{4.9}$$

where $|\boldsymbol{\xi}_E| = a_S/(D_S\theta_{\rm E})$. The lens-source separation vector $\boldsymbol{u}(t)$ can be described by

$$\boldsymbol{u}(t) = \begin{pmatrix} \tau'\cos\theta - u'\sin\theta \\ \tau'\sin\theta + u'\cos\theta \end{pmatrix}, \tag{4.10}$$

where $\tau' = \tau + \delta\tau$ and $u' = u_0 + \delta\beta$. The xallarap model can be described by ten parameters:

$$\boldsymbol{\zeta} = (\overline{F}, \nu, t_0, t_{\rm E}, u_0, \xi_{{\rm E},\parallel}, \xi_{{\rm E},\perp}, \phi_\xi, \lambda_\xi, P_\xi). \tag{4.11}$$

4.2.2 Fisher Matrix Analysis

To estimate the expected uncertainty of each parameter (ζ_i) by the *Roman* microlensing survey, we calculate the Fisher matrix of the light curve model $F(t_k, \boldsymbol{\zeta})$ with given parameter set $\boldsymbol{\zeta}$. Under the assumption of independent errors, the Fisher matrix elements $b_{i,j}$ can be written as

$$b_{i,j} = \sum_{k=1}^{N} \frac{1}{\sigma_k^2} \frac{\partial F(t_k)}{\partial \zeta_i} \frac{\partial F(t_k)}{\partial \zeta_j} \tag{4.12}$$

where N is the total number of the data points, and σ_k is the photometric error on data point at t_k. Once the Fisher matrix is calculated, the covariance matrix for parameters $\boldsymbol{C}$ is given by its inverse matrix, i.e.,

$$\boldsymbol{C} = \boldsymbol{b}^{-1}. \tag{4.13}$$

We follow the logic of M16 and discard (negligible) contribution of $\bar{F}$ from our Fisher matrix analysis[3]. In principle, the uncertainties for the xallarap amplitude depend on the event geometry, i.e., $\sigma^2_{\xi_\mathrm{E}}(\theta, \phi_\xi)$. To produce the results which are independent from the geometric conditions, M16 analytically found the minimum uncertainty on parallax measurement, $\sigma^2_{\pi_\mathrm{E},\mathrm{min}}$, which is independent of θ. We modify it for xallarap measurements $\sigma^2_{\xi_\mathrm{E},\mathrm{min}}(\phi_\xi)$ as

$$\begin{aligned}
\sigma^2_{\xi_\mathrm{E},\pm}(\phi_\xi) &= \frac{\sigma^2_{\xi_{\mathrm{E},\parallel}} + \sigma^2_{\xi_{\mathrm{E},\perp}}}{2} \\
&\pm \frac{\sqrt{(\sigma^2_{\xi_{\mathrm{E},\parallel}} - \sigma^2_{\xi_{\mathrm{E},\perp}})^2 + 4\mathrm{cov}(\xi_{\mathrm{E},\parallel}, \xi_{\mathrm{E},\perp})^2}}{2}, \\
\sigma^2_{\xi_\mathrm{E},\mathrm{min}} &\equiv \min_{\phi_\xi \in [0,2\pi]} \sigma^2_{\xi_\mathrm{E},-}(\phi_\xi).
\end{aligned} \tag{4.14}$$

As M16 noted, for $P_\xi \ll u_0 t_\mathrm{E}$, the covariance between the xallarap vector components $\xi_{\mathrm{E},\parallel}$ and $\xi_{\mathrm{E},\perp}$ disappear so that σ_{ξ_E} becomes independent of ϕ_ξ.

In this work, we assume continuous observations of 72 days with a 15 min cadence and Gaussian photometric errors that are consistent with simulated photometric error bars shown in Figure 4 of P19. Periodic correlated noise is expected to be mainly produced by spacecraft systematics and stellar pressure-driven (p-mode) oscillations. Detailed photometric simulations on all systematic errors are computationally expensive. P19 applied sub-optimal aperture photometry in their simulated photometric pipeline and added a Gaussian systematic error floor of 1 mmag in quadrature into their photometric results to compensate for un-modeled systematic errors. Timescales of xallarap signals, which are typically > 0.1 day, are much longer than the expected timescale of p-mode oscillations of main-sequence stars (Broomhall et al., 2009). Moreover, Gilliland et al. (2015) found that most *Kepler* stars have a median photometric variability of ~ 0.2 mmag, with timescale of < 0.6 hr. This is somewhat smaller than P19's error floor of 1 mmag.

We also assume the source mass and distance to be $M_S = 1\ M_\odot$ and $D_S = 8$ kpc, respectively, and the angular Einstein radius to be $\theta_\mathrm{E} = 0.3$ mas, which approximately leads to

$$\xi_\mathrm{E} \sim 4.6 \times 10^{-5} \left(\frac{M_P}{M_\mathrm{Jup}}\right) \left(\frac{P_\xi}{\mathrm{day}}\right)^{2/3}. \tag{4.15}$$

In our analysis, we consider the orbital inclination of $\lambda_\xi = 45°$ and t_0 to be at center of 72 days *Roman* observing window. Our result is hardly dependent on θ because we adopt $\sigma_{\xi_{\mathrm{E},\mathrm{min}}}$ that is independent of the event geometry. Here we set $\theta = 45°$. For each *W146*$_S$, we adopt the value of the blend flux ratio ν to be the same with the median value of the ν distribution that is obtained by the P19 simulation. Note that we assume the

[3] An arbitrary uncertainty on $\overline{F}$ is achievable with a sufficient number of photometric observations while the event is at baseline. *Roman* will collect $\sim 40{,}000$ measurements in its *W146* bandpass per light curve during the survey, which spans 6×72-d seasons spread out over 4.5 years.

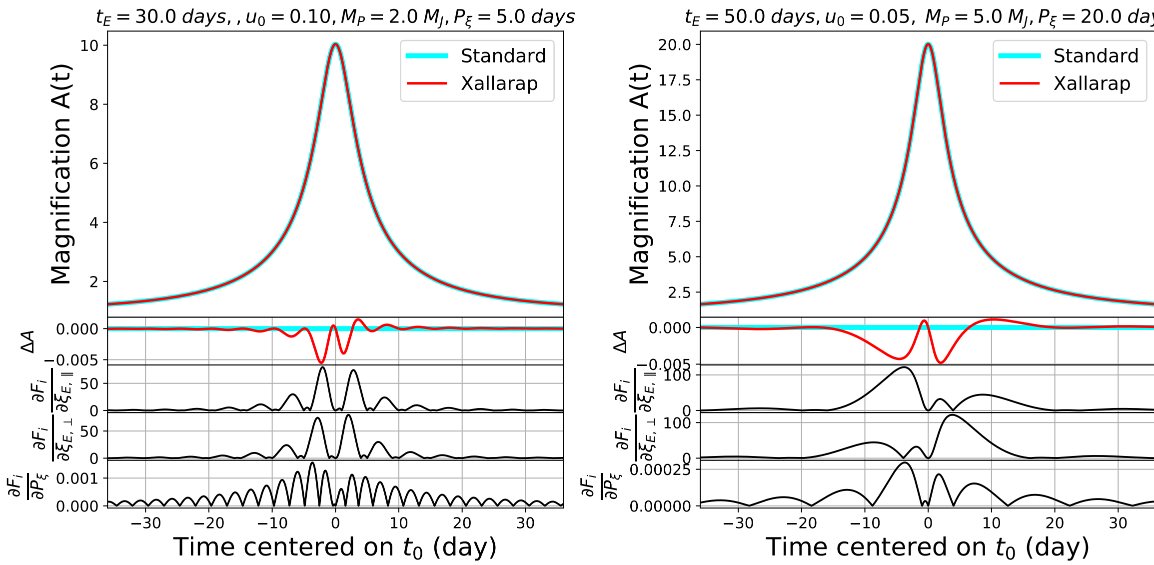

Figure 4.2 Two examples of simulated *Roman* light curves with xallarap. Top: The standard (cyan solid line) and xallarap (solid red line) light curves. Second to the Top: The residuals of the xallarap light curves relative to the standard ones. The three bottom panels: The absolute values of components of integrands of the Fisher matrix $\partial F(t_k)/\partial \zeta_i$ at a given time t_k.

microlens parallax effect does not affect the measurement of xallarap effect because the xallarap period we focus here is much shorter than 365 days for the parallax, and is thus likely distinguishable. We do not consider the finite source effect (Witt & Mao, 1994) because the effect can be easily modeled and is distinguishable from xallarap. We also do not consider binary-lens events. Although the binary-lens event would be more sensitive to the xallarap effect than the single-lens event, it is outside the scope of this work. We also ignore any accelerations induced by *Roman*'s orbit around L2.

The nominal expected fractional error on the companion mass can be derived from Equation (4.3) as

$$\frac{\sigma_{M_P}}{M_P} = \sqrt{\left(\frac{\sigma_{\xi_{\mathrm{E,min}}}}{\xi_{\mathrm{E}}}\right)^2 + \frac{4}{9}\left(\frac{\sigma_{P_\xi}}{P_\xi}\right)^2}, \tag{4.16}$$

by assuming the uncertainties on θ_{E}, D_S, and M_S are negligible. We set the detection threshold for the xallarap companions as $\sigma_{M_P}/M_P = 0.3$ in the following analysis. The impacts of uncertainties of θ_{E}, D_S, and M_S on the measurements of companion's masses is discussed in Appendix B.2.

4.2.3 Xallarap Light Curves

Figure 4.2 shows two samples of model light curves with and without xallarap effect in the top panels. The residuals of light curves between that with xallarap and without are shown

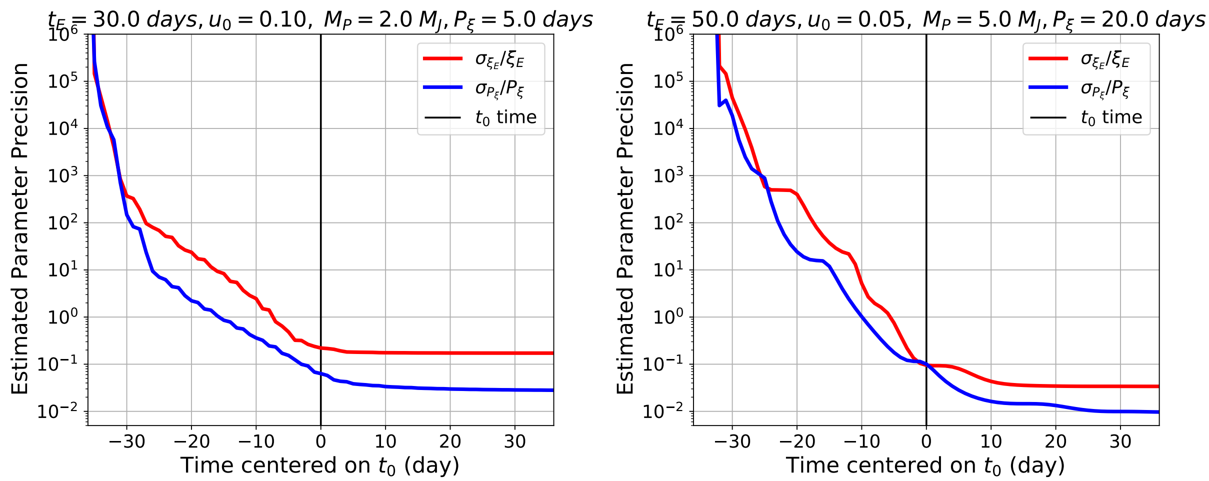

Figure 4.3 Parameter uncertainties for the xallarap amplitude $\xi_{\rm E}$ (red lines) and orbital period P_ξ (blue lines) estimated at each time when a *Roman* observation is conducted. To obtain these lines, we calculate the covariance matrices from the Fisher matrix at each observation. The parameter conditions for the two panels are identical to that of Figure 4.2.

in the second panels. The left figure represents an event with $t_{\rm E} = 30$ days, $u_0 = 0.1$, $M_P = 2\ M_{\rm Jup}$ and $P_\xi = 5$ days. In this case, the maximum deviations from the standard model is about 0.5% of the source flux, which is comparable to the *Roman* photometric noise level for *W146*$\sim$ 20 mag (see Figure 4 of P19). This indicates that brighter and/or high-magnification events are promising targets for *Roman* to detect xallarap features induced by a Jupiter-mass planet around the source star. In the three bottom panels, we plot the components of integrands of the Fisher matrix $\partial F(t_k)/\partial \zeta_i$ at a given time t_k. These panels imply that the observations during $t_0 \pm P_\xi$ are most important to determine the xallarap parameters (ζ_i) related to the mass of companion M_P. However, note that observations further into the wings continue to add to the precision of the period estimate (see the most bottom panels).

For understanding what parts of light curves are important to constrain the parameters, we derive the parameter uncertainties using the Fisher matrix analysis at each time when a *Roman* observation is conducted. Figure 4.3 represents the cumulative precisions on $\xi_{\rm E}$ and P_ξ as a function of time for the *Roman* light curve with $W146_S = 18$ mag (corresponding to Figure 4.2). We found that the parameter uncertainties are gradually constrained with increasing data points from the wing of the light curves. Moreover, we also derive the cumulative precision on the parameters as a function of the coverage duration for the light curve peak (Figure 4.4). We found that the resultant parameter precisions strongly depend on how long the light curves cover around the event peaks. Figure 4.3 and 4.4 indicate that the xallarap parameters can be measured with incomplete light curves that cover around $t_0 \pm P_\xi$. This is particularly important for *Roman*, which has a short observing window of 72 days.

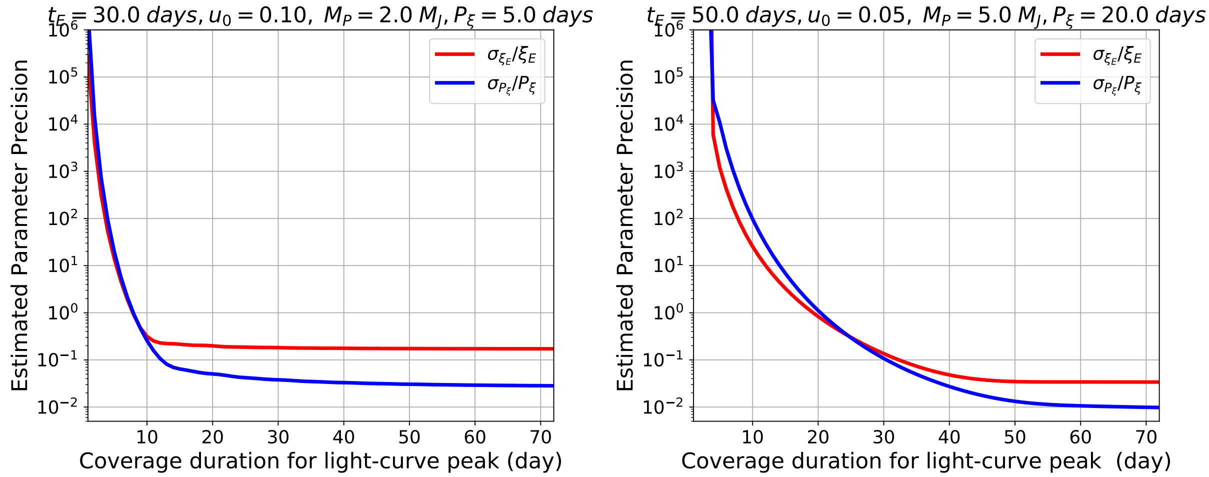

Figure 4.4 Parameter uncertainties for the xallarap amplitude $\xi_{\rm E}$ (red lines) and orbital period P_ξ (blue lines) as a function of the coverage duration for the light-curve peak (t_0). For plotting these, data points of *Roman* light curve are uniformly distributed within the duration centered on t_0 and then we conduct the Fisher matrix analysis using the data points. The parameter conditions for the two panels are identical to that of Figure 4.2.

4.2.4 Xallarap Sensitivity Map

At a given $(t_{\rm E}, u_0,\ W146_S)$, we conducted the Fisher matrix analysis on a grid of points over the ranges of $-2 \leq \log(M_P/M_{\rm Jup}) \leq 2$ and $-1 \leq \log(P_\xi/{\rm day}) \leq 3$ with 20×20 grid points, respectively. In Figure 4.5, we present samples of xallarap sensitivity maps in the mass-orbital period plane for the *Roman* event with $W146_S = 18$ mag. The color maps in each panel represent the distributions of σ_{M_P}/M_P and the black lines correspond to contour lines of our detection threshold of $(\sigma_{M_P}/M_P) = 0.3$. The row and column of a panel correspond to the labeled values of u_0 and $t_{\rm E}$. For example, in the case of $\log(t_{\rm E}) = 2,\ \log(u_0) = -1.5$ (bottom right panel), the *Roman* light curve has a potential to precisely measure the mass of a warm Jupiter with an orbital period of 10-30 days via xallarap. We found that M_P is well constrained when $t_{\rm E}$ is longer and u_0 is smaller in a given (M_P, P_ξ) grid. One can also find that there are sharp cut-offs of the sensitivity with the orbital period of a few dozens days. This might be because the *Roman* observing window of 72 days could not cover the full orbital period of the events beyond the cut-off and thus is insufficient to constrain the xallarap parameters[4]. This can be expected from the results of Figure 4.3 and 4.4.

[4]When we derive the sensitivity maps, we consider only an observing window of a single season. The sensitivity might extend toward the longer orbital period if we consider all the observing windows. However, it is not expected to be so much because of the results of Figure 4.4 and because there are long time-gaps between the *Roman* observing windows. Here we focus on only short-period planets and brown dwarfs.

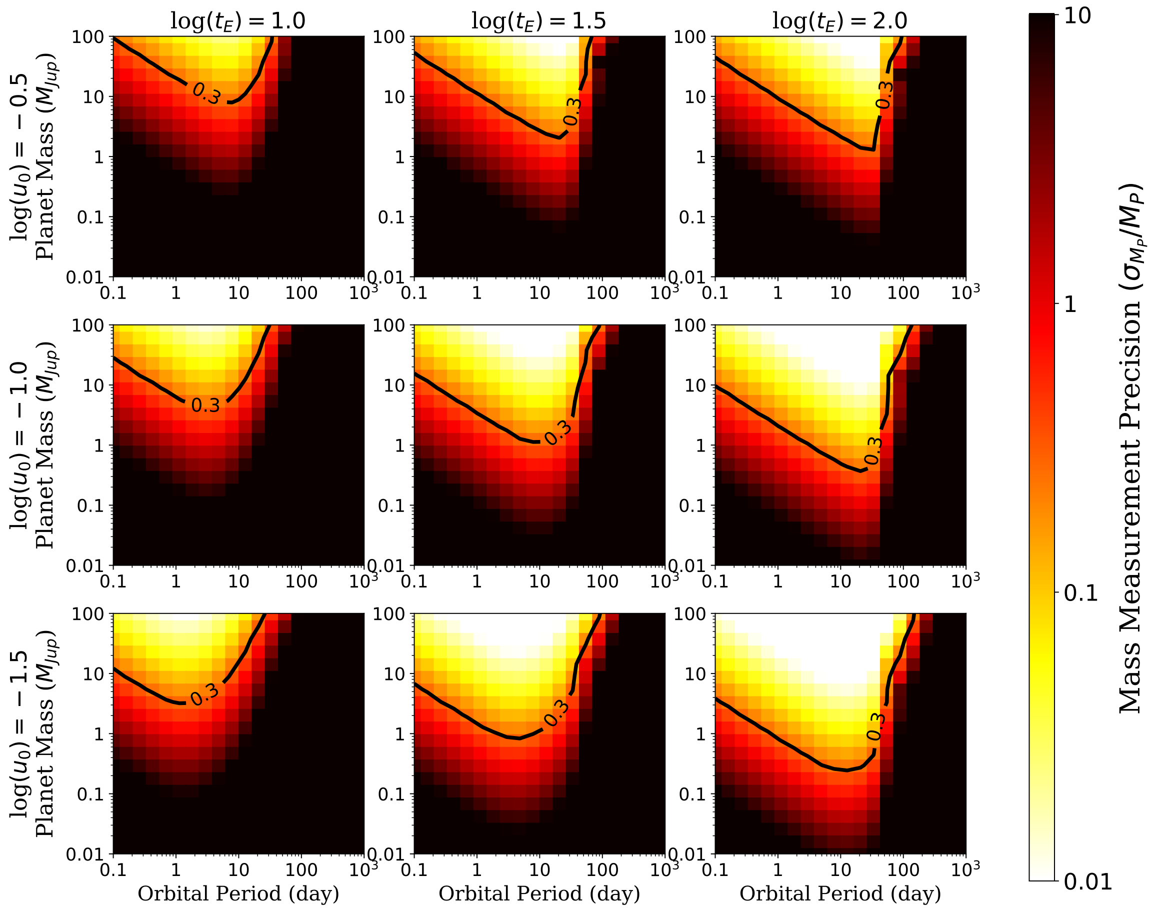

Figure 4.5 Color map distributions of the planetary mass error $\left(\frac{\sigma_{M_P}}{M_P}\right)$ for an event with the source magnitude of $W146_S = 18$ mag.

4.3 Prediction of the Yields of Close-in Exoplanets with Xallarap

4.3.1 Simulating on the *Roman* Observation

In this section, we estimate the detection number of close-in planets and brown dwarfs (BDs) in source systems via xallarap during the *Roman* mission. To simulate the *Roman* microlensing survey, we employ the single stellar lens module of the GULLS microlensing simulator (Penny et al., 2013, 2019) which uses version 1106 of the Besançon Galactic population synthesis model (Robin et al., 2003, 2012) to generate pairs of lens and source stars. In Table 4.1, we summarize the survey parameters for the Cycle 7 design that we use in our simulation. The full survey details are described in P19 and Johnson et al. (2020). Note that we consider only single-lens events whose peaks are within the *Roman* observing window.

Table 4.1: Parameters for *Roman* Galactic Exoplanet Survey

Survey Area	1.97 deg^2
Mission Baseline	4.5 years
Seasons	6×72 days
Observation Fields	7
Microlensing Events with $\|u_0\| < 1$	~ 27000
$W146$ Exposures	$\sim 41,000$ per fields
$W146$ Cadence	15 minutes
Photometric Precision	~0.01 mag @ W146~ 21.15

NOTE - The parameters for the Cycle 7 design we use are fully described in Penny et al. (2019) and Johnson et al. (2020). In this chapter, we do not consider any observations with the Z087 filter and other filters that are to be conducted during the *Roman* microlensing survey,which could improve our prediction of planet yields to some extent.

We classified the simulated *Roman* events from GULLS by the values of $(u_0, t_{\rm E}, W146_S)$ into bin $7 \times 10 \times 10$ over the ranges of $14 < W146_S < 28$ mag, $-2 < \log u_0 < 0$, and $0 < \log(t_{\rm E}/{\rm day}) < 2.5$, respectively. We generated the sensitivity maps with the parameters at the center of each bin to be used for all events in each bin. Then we counted the number of detected events by using the corresponding sensitivity maps at each (M_P, P_ξ) grid. Figure 4.6 shows the resultant detections, i.e., the expected planet yields during the *Roman* survey mission if all source stars were to have a planet at each (M_P, P_ξ) grid point. The black solid lines represent the contours of the planet yields for $1, 10, 100$ and 1000. The detection sensitivity peaks around $P_\xi = 20 - 30$ days and there it reaches to sub-Jovian or Saturn masses. In Figure 4.6, we also plotted observed exoplanets (open dots) from the NASA Exoplanet Archive[5] (Akeson et al., 2013). *Roman*'s sensitivity to planets via the xallarap effect largely covers the parameter spaces of hot and warm Jupiters with $M_P > 0.5\ M_{\rm Jup}$ and $0.1 < P < 100$ days, which suggests that this method could be useful to probe the hot and warm Jupiter populations in the Galactic bulge. Note that we used only a single 72 days season for each event.

4.3.2 Planet Yields

In order to estimate the planet yields, we assume the secondary mass and period distributions. We describe the distribution function f as a double power law,

$$\frac{\partial^2 f}{\partial \ln M\ \partial \ln P} = C_{\rm norm} \left(\frac{M_P}{M_{\rm Jup}}\right)^{\alpha_M} \left(\frac{P}{\rm day}\right)^{\beta_P}, \tag{4.17}$$

[5] https://exoplanetarchive.ipac.caltech.edu/

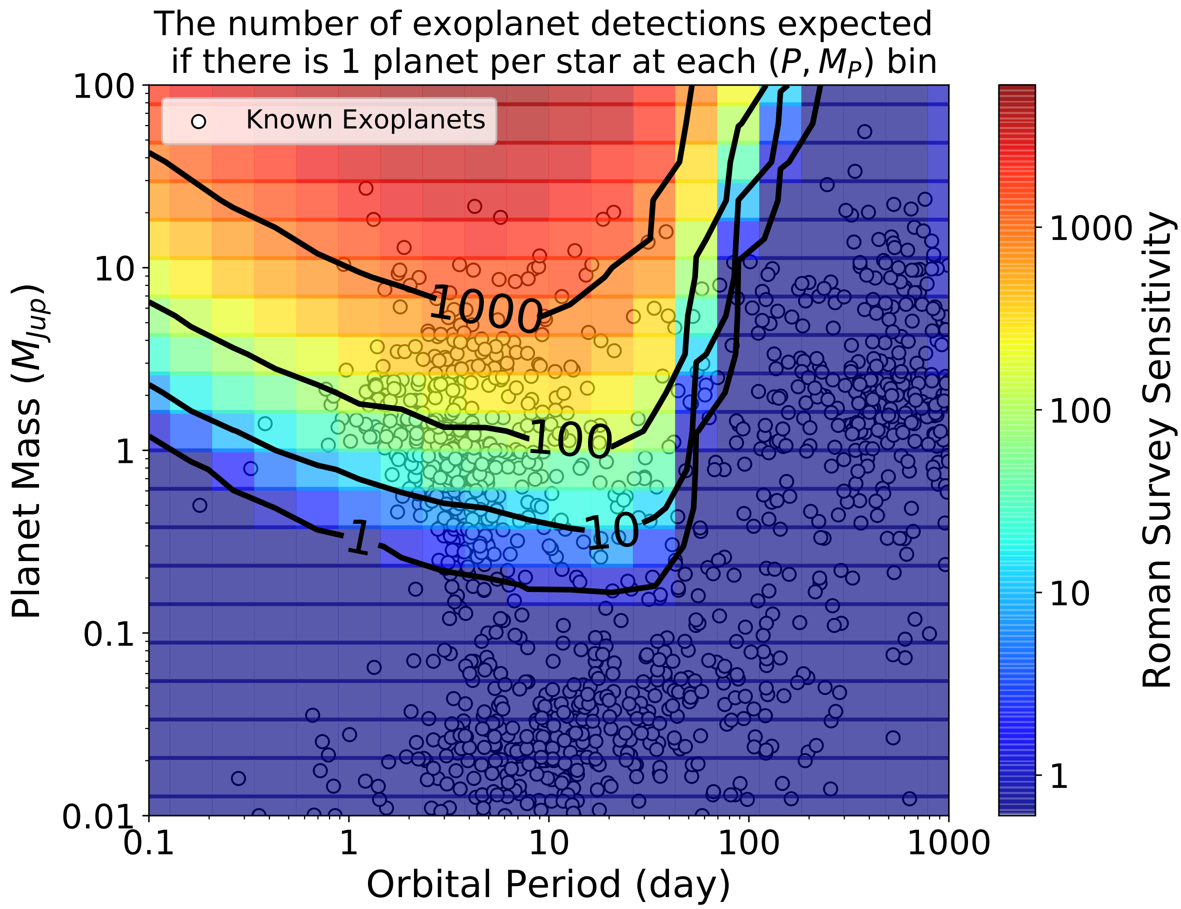

Figure 4.6 *Roman* xallarap sensitivity in the mass-orbital period plane. The color map shows the number of detections for xallarap planets or brown dwarfs during the *Roman* mission at a given mass and orbital period grid if there is one planet per star at a given grid. The open circles represent confirmed exoplanets referenced from NASA Exoplanet Archive (Akeson et al., 2013).

where C_{norm} is a normalization factor. In this work, we adopted the power law indices of $\alpha_M = -0.31 \pm 0.2$ and $\beta_P = 0.26 \pm 0.1$ derived by Cumming et al., 2008, (hereafter C08). These values are derived by using 48 RV-detected planets ranging $0.3 < M_P < 10\ M_{\text{Jup}}$ and $2 < P < 2000$ days that are around Sun-like stars. We adopted $C_{\text{norm}} = 0.036\ \text{dex}^{-2}\text{star}^{-1}$ to be consistent with a planet frequency of 10.5% around Sun-like stars in these ranges derived by C08. Note that we simply extrapolate this C08's power-law to the ranges $0.01 < M_P < 100\ M_{\text{Jup}}$ and $0.1 < P < 1000$ days. The extrapolation below $0.3\ M_{\text{Jup}}$ hardly affects the final result because the sensitivities to low-mass planets with $< 0.3\ M_{\text{Jup}}$ is very low and the *Kepler* survey suggested that the occurrence rate does not significantly rise until below Neptune size of $\sim 5\ R_\oplus$ (e.g. Fressin et al., 2013). The extrapolations to other range need cautions as discussed below. We also estimate the yields assuming

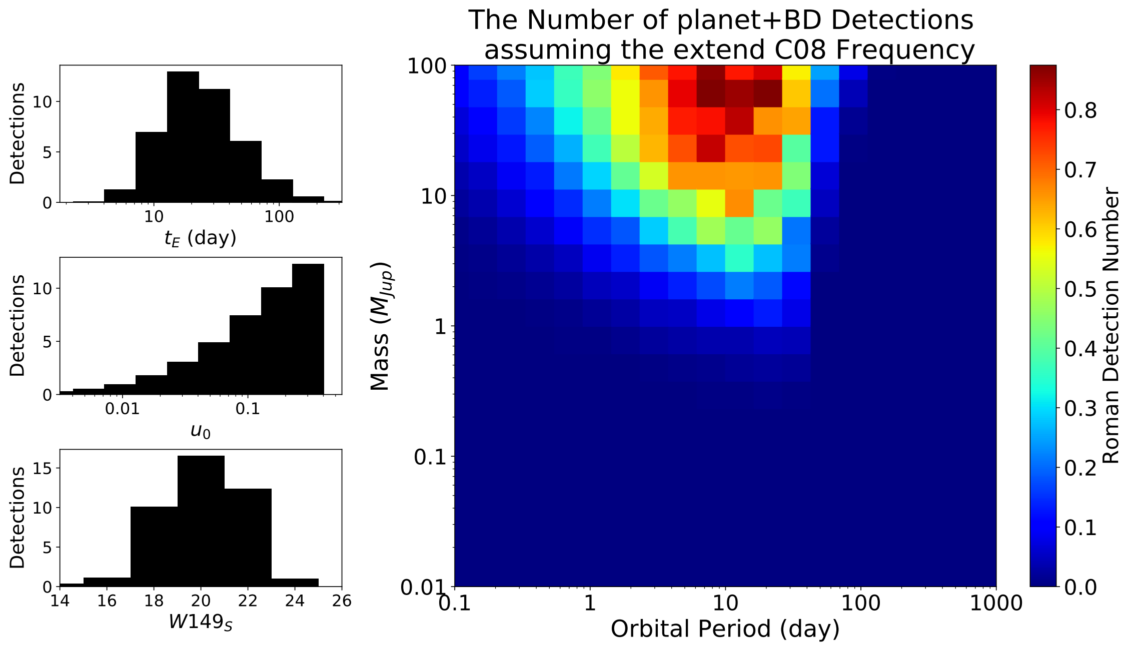

Figure 4.7 Expected number of the planet and brown dwarf yields during the *Roman* mission assuming the extended C08 frequency. The left three panels are the histograms of the yields binned by $t_{\rm E}$, u_0, and $W146_S$. The color map in the right panel represents the yields per a given mass-orbital period grid.

a simple frequency model of $(\alpha_M, \beta_P) = (0, 0)$ and $C_{\rm norm} = 0.063$ dex^{-2}star^{-1}, which corresponds to single planet per star over the ranges. This can be considered as the reference yields.

Figure 4.7 represents the expected yields of the *Roman* observations assuming the extended C08 distribution. The three left panels show the distributions of $t_{\rm E}$, u_0, and $W146_S$ for events in which the planet/BD companion around the source is detected. The yields are expected to largely come from the events with $18 < W146_S < 22$ mag, which mostly consists of main sequence source stars. Note that although the histogram with u_0 indicates that the detections increase towards larger u_0, as shown in Figure 4.5, the events with large u_0 are only sensitive to massive companions. The right panel in Figure 4.7 shows the distribution for the number of planet and BD detections over the parameter spaces of masses and periods assuming the frequency from C08. Table 4.2 summarizes the expected yields assuming the two different distribution functions. Adopting the extended C08 distribution, we found that ~ 10 planets with $M \leq 10\ M_{\rm Jup}$ would be detected by xallarap. We can expect ~ 30 companions with $10 < M_P < 100\ M_{\rm Jup}$ if the extrapolation of C08 is correct. However, due to "brown dwarf desert" (Grether & Lineweaver, 2006), BD discoveries may by much less common than predicted using the C08 frequencies [6]. We

[6]Under the extend C08 function, the existence frequency of BDs around solar-type star is $\sim 3\%$ per star. Grether & Lineweaver (2006) reported that is $< 1\%$ per star. More recently, Santerne et al. (2016) reported the occurrence rate of BDs within 200 days of the orbital period with $0.29 \pm 0.17\%$ in the *Kepler*

can test the "brown dwarf desert" in the Galactic bulge by applying this method to the upcoming *Roman* light curves.

Table 4.2: Expected Yields

	Distribution Function	
	Simple Model[a]	Extend C08[b]
Companion Mass M_P ($M_{\rm Jup}$)		
$10 \leq M_P < 100$	409.6	30.9
$1 \leq M_P < 10$	63.3	10.1
$0.1 \leq M_P < 1$	1.05	0.37
$M_P < 0.1$	0.0022	0.0014
Orbital Period P (days)		
$100 \leq P < 1000$	0.043	0.007
$10 \leq P < 100$	112	15.7
$1 \leq P < 10$	243	20.7
$P < 1$	118	5.1
Total	474	42

[a] Simple power-law function with $(\alpha_M, \beta_P) = (0, 0)$.
[b] Cumming et al. (2008) power-law function extended over ranges of $0.01 < M_P < 100$ $M_{\rm Jup}$ and $0.1 < P < 1000$ days.

4.4 Discussion

4.4.1 How to Distinguish Lens Orbital Motion

If the lensing body is in a binary system, lens orbital motion (LOM) will provide a similar effect to that of xallarap, which has been pointed out in several papers (Rahvar & Dominik, 2009; Penny et al., 2011). In a planetary system with orbital period of $P \leq 30$ days, a projected angular separation between a lensing host star and its planet in units of $\theta_{\rm E}$, $s = a/\theta_{\rm E}$, is expected to be an order of $s \leq 0.06$. It is unlikely that a lens companion with such a small s provides noticeable light curve deviations by their extremely small caustics. For example, Penny et al. (2011) found that periodic (caustic) features of light curve due to LOM would be most detectable for binary-lens with semimajor axes of ~ 1 au. Thus it is difficult to distinguish between xallarap and LOM. However the degeneracy may be resolved when following additional high-order effects are observed in the light curves. The following effects can be observed only in the xallarap events, not in the LOM events.

Magnified Planet Flux Planets orbiting source stars produce reflect light from their host and/or emit their own flux from thermal emission. If flux from these companions

transit candidates.

are magnified, we can observe these contributions in the light curve, as a so-called binary source microlensing event. (Graff & Gaudi, 2000; Sajadian & Rahvar, 2010). Typical flux ratios between solar-type stars and hot Jupiters in the *W146* band is on the order of $\sim 10^{-3}$ to 10^{-4}. Using this detection channel, Bagheri et al. (2019) estimated that *Roman* will discover ~ 70 exoplanets from single-lens events and ~ 3 exoplanets from binary-lens events.[7] We expect that the binary source effect might be observed in the *Roman* xallarap single-lens events of $P < 5$ days, which corresponds to $\sim 50\%$ of the total yields. It would also help us to constrain the orbital parameters of source systems because it provides the geometric relation between host and planet at the time when the planet is magnified. Full binary-source modeling including xallarap effect (Miyazaki et al., 2020) is more realistic and might have more sensitivity, but this is out of the scope of this work.

Transiting Source Stars If the planet transits the source star, we can also simultaneously observe the transiting signal during the microlensing event (Lewis, 2001; Rybicki & Wyrzykowski, 2014). Typical amplitudes of the transit signal for Jupiter-size planet would be $\sim 1\%$ of the source brightness, which will be easily detectable for most xallarap planetary events. For example, *Roman* is expected to detect thousands of transiting hot Jupiters, including in the galactic bulge (McDonald et al., 2014; Montet et al., 2017) The geometric transit probability of warm Jupiters is $\sim 5\%$ so that $\sim 5\%$ of xallarap planetary events could be distinguishable from LOM events by the transit signals. With the measurement of the planet radius by the transit, we can estimate the density of the planet in combination with the mass measurement by xallarap. This can potentially test how chemistry affects giant planet structures (e.g. Cabral et al., 2019).

Ellipsoidal Variations Ellipsoidal variations can be caused by tidal effects on the source from the companion (Morris, 1985). The amplitude of the ellipsoidal variation is approximated by

$$\begin{aligned} A_{\rm ellip} &\simeq \alpha_{\rm ellip} \frac{M_P \sin\lambda_\xi}{M_S} \left(\frac{R_S}{a_{SC}}\right)^3 \sin\lambda_\xi \\ &= 13 \text{ ppm} \left(\frac{M_P \sin\lambda_\xi}{M_{\rm Jup}}\right) \left(\frac{R_S}{R_\odot}\right)^3 \\ &\times \left(\frac{M_S}{M_\odot}\right)^{-2} \left(\frac{P_\xi}{\rm day}\right)^{-2} \alpha_{\rm ellip} \sin\lambda_\xi, \end{aligned} \tag{4.18}$$

where R_S is the radius of the source star. The coefficient $\alpha_{\rm ellip}$ accounts for the stellar limb darkening and gravity darkening:

$$\alpha_{\rm ellip} = 0.15 \frac{(15+u)(1+g)}{3-u}, \tag{4.19}$$

[7]Note that their detection samples were mostly composed of hot Jupiters with $a < 0.05$ au, and they assumed a source star has an exoplanet per event.

where g and u are the coefficients of the gravity darkening and linear limb darkening, respectively (Shporer, 2017). It would be difficult to observe this effect for the xallarap planetary events. However, it might be possible for events of substellar source companions.

Doppler Beaming It is known that a line of sight motion due to the orbit causes a periodic variation in the light curve, also known as Doppler beaming (Loeb & Gaudi, 2003; Shporer, 2017). The photometric amplitude of the beaming effect $A_{\rm beam}$ is described as below,

$$\begin{aligned} A_{\rm beam} &= 2.8\times 10^{-3}\,\alpha_{\rm beam}\left(\frac{P_\xi}{\rm day}\right)^{-1/3} \\ &\times \left(\frac{M_S+M_P}{M_\odot}\right)^{-2/3}\left(\frac{M_P\sin\lambda_\xi}{M_\odot}\right), \end{aligned} \tag{4.20}$$

where $\alpha_{\rm beam}$ is the coefficient accounting of variation of photon amounts in a specific band, e.g. $\alpha_{\rm beam}\equiv 1$ in bolometric light. For longer orbital period of $P_\xi > 10$ days, the amplitude of this effect is much stronger than that of the ellipsoidal variations and it is more promising to observe.

These effects may be able to resolve the degeneracy between the xallarap and LOM interpretations in some fraction of xallarap events and provide additional information for source systems.

4.4.2 Short-period Populations in the Galactic Bulge Revealed by *Roman*

Some observational results have suggested that there are possible differences in planetary populations between the local neighborhood and the distant region of our Milky Way. RV surveys around the local region close to the Sun indicates an occurrence rate of hot Jupiters of order 1% (Cumming et al., 2008; Wright et al., 2012). On the other hand, *Kepler* transit survey toward the Cygnus region suggested the occurrence rate of $0.4\pm0.1\%$ (Howard et al., 2012), which is approximately half of that in the local neighborhood. Penny et al. (2016) used a sample of 31 microlensing exoplanetary systems and suggested the abundance of planets might be less in the Galactic bulge than in the disk. Such studies would be very important to help understanding whether the planetary formations could depend on its surrounding environment in our Galaxy .

Montet et al. (2017) predicted that *Roman* is expected to discover $\sim 100,000$ transiting planets and enable us to directly confirm several thousands hot Jupiters via its secondary eclipse in the light curves. A large fraction of the transiting planets will belong to the Galactic bulge. However, in general, the most of host stars are too faint to conduct follow-up RV observations for constraining their planetary mass and avoiding false positives. Montet et al. (2017) also discussed some feasibilities for the validation for transiting planets and the estimation of their masses by using phase curve variations although it requires high photometric precisions to observe. Applying our xallarap method to the *Roman* microlensing light curves, we can expect to discover some dozens of hot and warm Jupiters and close-in BDs with measured masses. These samples will help our understanding of the exoplanet demographics at short orbital periods in the Galactic bulge. For larger masses, they are also useful to probe the“brown dwarf desert” around main-sequence stars and study of stellar binary distribution in the Galactic bulge.

Chapter 5

Summary and Conclusion

In this thesis, I have presented two analyses relevant to microlensing. In Chapter 3, I presented the observation and analysis of the planetary microlensing event OGLE-2013-BLG-0911. In the analysis, I found a new binary-lens model with planet/host mass ratio of $q \sim 10^{-2}$, which is much preferred than that reported in previous research (Shvartzvald et al., 2016). The measurements of both the finite source effect and orbital parallax effect allow us to directly estimate the physical parameters of the lens system. The lens system is an M-dwarf orbited by a massive super Jupiter companion at very close ($M_{\rm host} = 0.30^{+0.08}_{-0.06}\ M_{\odot}$, $M_{\rm comp} = 10.1^{+2.9}_{-2.2}\ M_{\rm Jup}$, $a_{\rm exp} = 0.40^{+0.05}_{-0.04}$ au) or wide ($M_{\rm host} = 0.28^{+0.10}_{-0.08}\ M_{\odot}$, $M_{\rm comp} = 9.9^{+3.8}_{-3.5}\ M_{\rm Jup}$, $a_{\rm exp} = 18.0^{+3.2}_{-3.2}$ au) separation. In addition, I found that the source has a late M-dwarf companion by the significant measurement of the xallarap effect. This is the first demonstration that dark, low-mass objects in the Galactic bulge can be detected and characterized via xallarap even with ground-based photometry. Stimulated on this discovery, in Chapter 4, I investigated the potential of the *Nancy Grace Roman Space Telescope* (*Roman*) to detect and characterize short-period planets and brown dwarfs in source systems using xallarap effect. I analytically showed that the *Roman* Galactic Exoplanet Survey (RGES) can detect warm Jupiters with masses down to 0.5 $M_{\rm Jup}$ and orbital periods up to 30 days and estimated that *Roman* will detect $\sim$ 10 hot and warm Jupiters and $\sim$ 30 close-in BDs around microlensed source stars during RGES. I also showed that the detections are likely to be accompanied by the measurements of the companion's masses and orbital elements, which will aid in the study of the physical properties for close-in planet and BD populations in the Galactic bulge.

Throughout the analyses, I particularly focused on one of the microlensing high-order effects, xallarap. Figure 5.1 shows the sensitivities of the RGES via the binary-lens channel (solid blue line) and the xallarap channel (solid red line). As shown in Chapter 4, the xallarap effect with the RGES data has the ability to detect and characterize distant short-period exoplanets and brown dwarfs that are not accessible by other methods. The galactic bulge is considered to be mainly populated with old stars that formed around 10 billion years (Zoccali et al., 2003; Hasselquist et al., 2020) and composed of fewer elements than our stellar neighborhood. The exploration using the xallarap might provide us with new implications and suggestions for planetary formation (Cabral et al., 2019; Hamer &

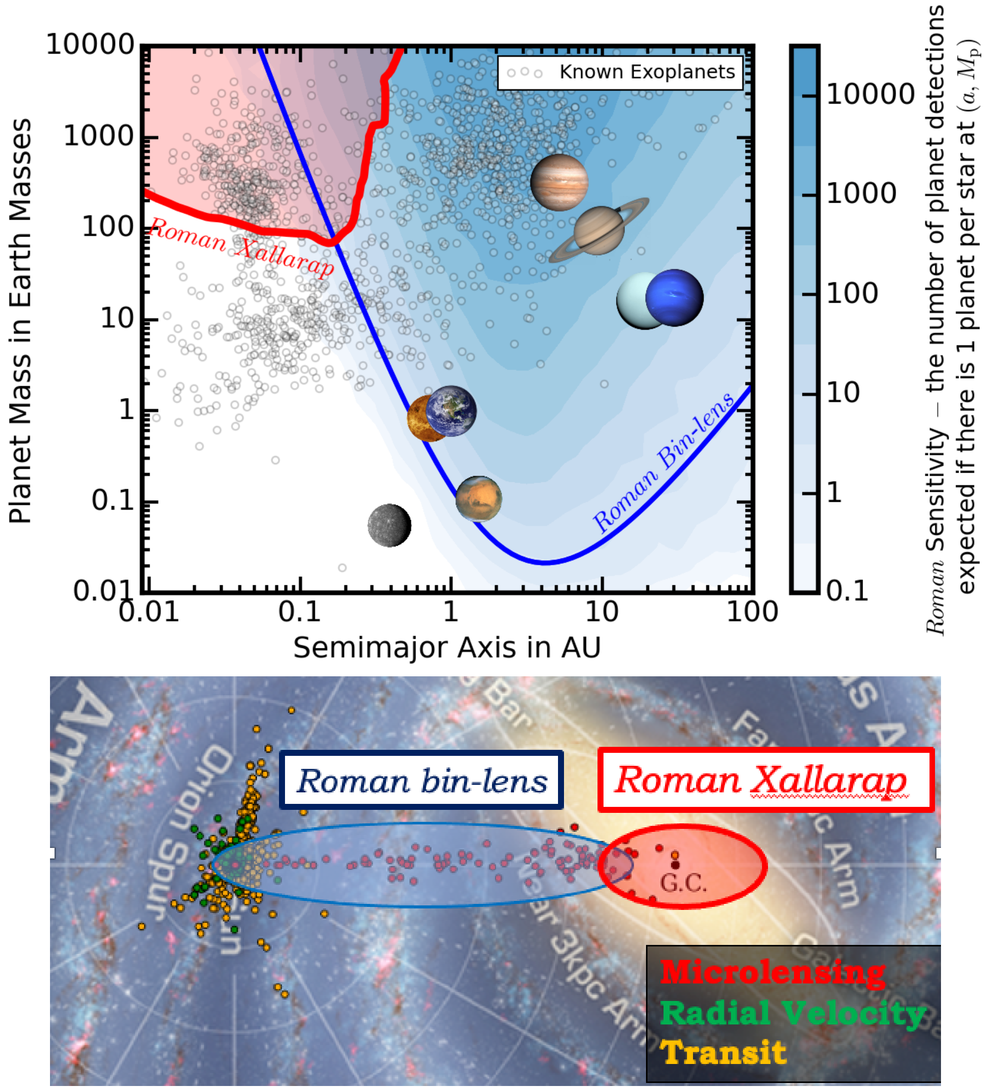

Figure 5.1 **Top panel**: The sensitivities of the RGES to exoplanets located toward the galactic bulge. Blue shading shows the number of *Roman* planet detections during the mission if there is one planet per star at a given mass and semimajor axis point via the binary-lens channel. Each colored solid line represents the 3-detection contour in each method. Red shading is the typical areas where the xallarap method has the detection sensitivity. The white dots are all the known exoplanets from the NASA exoplanet archive (Akeson et al., 2013). Solar system bodies are represented by their images.
Bottom panel: The detection sensitivity of the *Roman* survey with microlensing xallarap (red shading) and bin-lens (blue shading) methods to exoplanets located in our Galaxy. Known exoplanets are plotted and colored by the discovered method; transit (orange), RV (green), microlensing (red).

Schlaufman, 2019). Moreover, in the era of *Roman*, it is expected that other high-order effects that have not been often observed in ground-based surveys will also be detectable by the *Roman*'s high photometric accuracy. They will enable us to constrain more detailed planetary properties including mass, distance, and orbital parameters. Detailed analysis including higher-order effects as shown in this thesis with future data will expand our abilities to explore microlensing exoplanets and characterize their physical properties.

Appendix A

Appendix for Chapter 3

A.1 Calibration for the Source Magnitude for OGLE-2013-BLG-0911

We derived the apparent magnitude and color of the source from the measurements of CT13-I and V that were made during the time of high magnification. We basically followed the procedure described in Bond et al. (2017) in order to convert the CT13 instrumental magnitudes into the standard ones. We cross-referenced isolated stars around $2'$ of the source between the CT13 catalog reduced by DoPHOT (Schechter et al., 1993) and the OGLE-III catalog (Szymański et al., 2011). We found the following relation as

$$\begin{aligned} I_{\rm O3} - I_{\rm CT13} &= (27.070 \pm 0.011) - (0.032 \pm 0.006)(V - I)_{\rm CT13} \\ V_{\rm O3} - V_{\rm CT13} &= (27.851 \pm 0.017) - (0.101 \pm 0.011)(V - I)_{\rm CT13}. \end{aligned}$$

Consequently, we obtained the apparent color and magnitude of the source, $(V - I, I)_{S,\rm CT13} = (1.904 \pm 0.009, 19.618 \pm 0.006)$. Moreover, we also derived the source color and magnitude from the measurements of OGLE-I and V for confirmation. We used Equation (1) in Udalski et al. (2015) to calibrate the OGLE-IV instrumental magnitudes into the standard ones. We applied $\Delta{\rm ZP}_I = -0.056$, $\Delta{\rm ZP}_V = 0.133$, $\epsilon_I = -0.005 \pm 0.003$ and $\epsilon_V = -0.077 \pm 0.001$ for Equation (1) in Udalski et al. (2015), which are obtained by private communication with the OGLE collaboration. Finally, we derived the apparent source color and magnitude from OGLE-I and V, $(V - I, I)_{S,\rm O4} = (1.880 \pm 0.009, 19.594 \pm 0.006)$.

A.2 The impact of the assumption for M_S and D_S

We tested how the assumption of the fixed $M_S = 1\ M_\odot$ and $D_S = 8$ kpc impact on the final results. Figure A.1 represents the PARSEC stellar isochrone with solar metallicity and 10 Gyr age. Comparing the isochrone to the observed intrinsic source color and magnitude $(V - I, I)_{S,0} = (0.714 \pm 0.071, 18.104 \pm 0.049)$, we can state that the source mass and distance are likely to be in the ranges of $0.9 \leq M_S/M_\odot \leq 1.0$ and 6 kpc $\leq D_S \leq$ 10 kpc, respectively. In these likely ranges, we conducted light curve modeling for 1L2S, 2L1S and 2L2S with all the 15 combinations of the fixed $M_S = (0.9, 0.95, 1.0)\ M_\odot$ and $D_S = (6, 7, 8, 9, 10)$ kpc. We found that the fixed values have little effects on the best-fit χ^2 value and the MCMC posterior distributions for the lens physical parameters are consistent each other within 1σ except for the lens distance D_L. Therefore, we conclude that the assumptions for M_S and D_S do not significantly affect the final results except D_L.

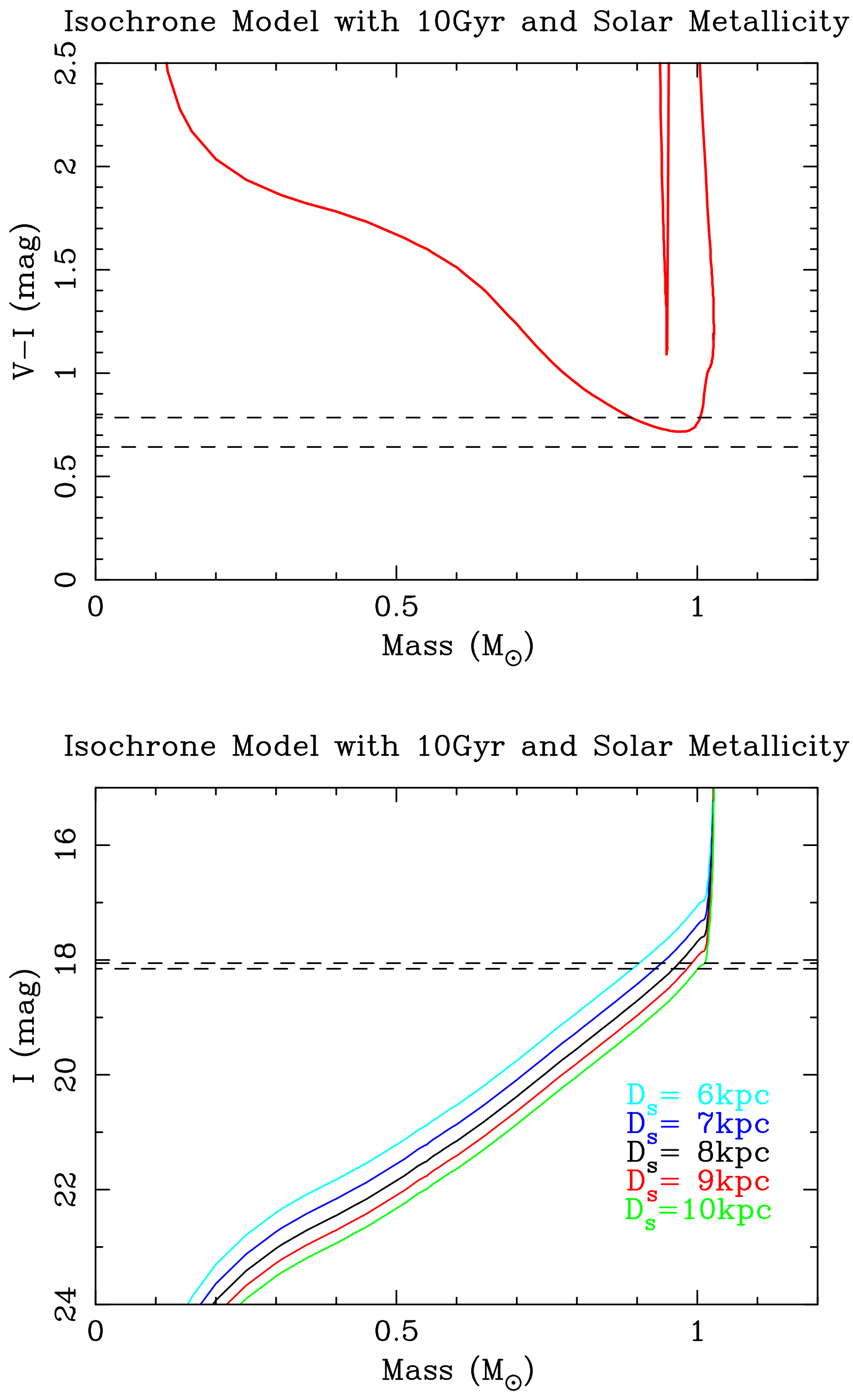

Figure A.1 PARSEC stellar isochrone model with solar metallicity and 10 Gyr age. The areas enclosed by horizontal dashed lines represent the 1σ ranges for the observed intrinsic source color $(V-I)_{S,0} = 0.714 \pm 0.071$ (right panel) and magnitude $I_{S,0} = 18.104 \pm 0.049$ (left panel), respectively.

Appendix B

Appendix for Chapter 4

B.1 $\Delta\chi^2$ Threshold and Fisher Matrix Analysis

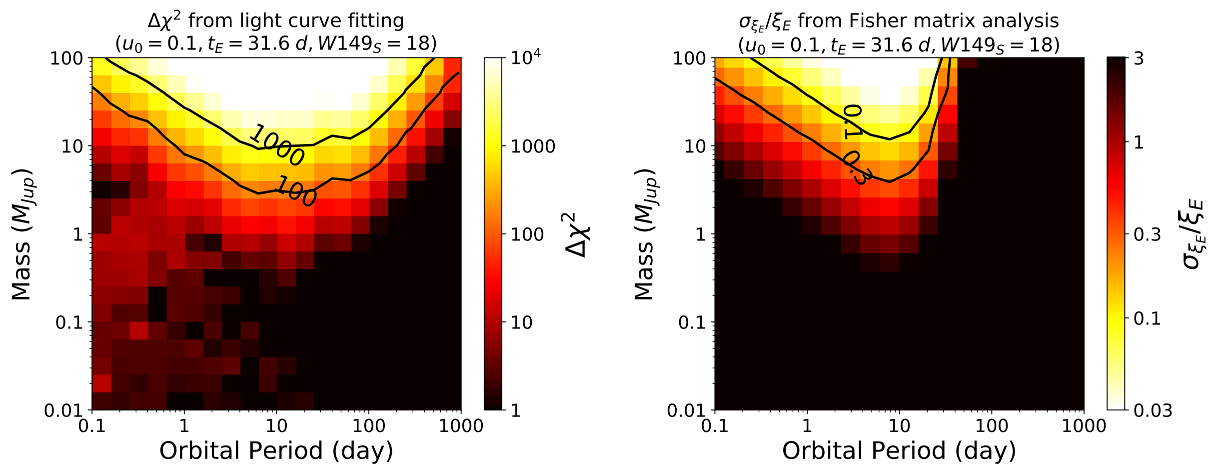

Figure B.1 The comparison of distributions over the mass-period diagram between $\Delta\chi^2$ from the light curve fitting (left panel) and the parameter uncertainty from the Fisher matrix analysis (right panel).

$\Delta\chi^2$ has been often chosen as a detection threshold of planets in most microlensing simulations (e.g. Bennett & Rhie, 1996; Penny et al., 2019; Johnson et al., 2020) possibly because quantifying the detectability can not be analytically solved for binary-lens modeling (see Penny et al., 2011 for a discussion of the challenges). Rahvar & Dominik (2009) studied xallarap induced by planetary companions also adopted the $\Delta\chi^2$ threshold of 11.07 for the detection threshold of planets. However, we adopt the Fisher matrix analysis that allows us to quantify the ability not only detecting xallarap signals but also characterizing the physical parameters. For demonstrating this, we conduct both the Fisher matrix analysis and light curve fitting in the same condition and compare them.

Figure B.1 represents an example of the result with a simulated *Roman* event of $(u_0, t_{\rm E}, W146_S) = (0.1, 31.6\ \text{days}, 18)$. In the left panel, the $\Delta\chi^2$ distribution is shown as a color map over the mass-period diagram. Here $\Delta\chi^2 = \chi^2_{\rm xallarap} - \chi^2_{standard}$ and χ^2_i value are calculated fitting each model to the simulated light curve. The right panel shows the uncertainty of xallarap amplitude $\xi_{\rm E}$ estimated from the Fisher matrix analysis. In the parameter space of $(P_\xi \geq 40\ \text{day}, M_P \geq 1\ M_{\rm Jup})$, one finds it is not possible to constrain $\xi_{\rm E}$ well though there should be large $\Delta\chi^2$ improvements if we fit the light curve by xallarap model. This can be because the light curve is strongly affected by only the source acceleration of a single direction and thus only one component of the xallarap vector $\boldsymbol{\xi}_{\rm E}$ can be constrained. For constraining xallarap parameters, it would be required to observe the source accelerations during the full time of source orbits. However, we note that it might be possible that the periodogram analysis of the residuals from a standard single-lens fit can constrain the orbital period of the planet sufficiently to enable an estimate of the planet mass (Nucita et al., 2014; Giordano et al., 2017).

B.2 Uncertainties on D_S, $\theta_{\rm E}$, and M_S

The ability of *Roman* to measure $\theta_{\rm E}$ and D_S has been studied in several papers. It is expected that most *Roman* events will have their relative lens-source proper motion $\boldsymbol{\mu}_{\rm rel}$ measured via direct detection of lens light in the *Roman* images, which enables us to measure $\theta_{\rm E}$ (Bennett et al., 2010, 2020; P19; Terry et al., 2020). Bhattacharya et al. (2018) estimated that *Roman* will measure the lens-source separations with less than 10% precision for most events. On the other hand, Gould & Yee (2014) analytically showed that events with photometric precisions of ≤ 0.01 mag have chances to provide the measurements of $\theta_{\rm E}$ with $\leq 10\%$ precision via astrometric microlensing in space-based microlensing experiments.[1] D_S for bright source events can potentially be measured by the direct parallax (astrometry) measurements in the *Roman* survey data (Gould et al., 2015). Even if not for bright source events, the combination of the three measurements of the microlens parallax $\pi_{\rm E}$, lens flux F_L, and $\theta_{\rm E}$ allows us to directly determine D_S. Moreover, D_S can be statistically estimated with $\sim 20\%$ precision using priors of standard Galactic model (e.g. Sumi et al., 2011; Bennett et al., 2014). For main sequence stars, M_S is expected to be approximately estimated from the source magnitude and color which are obtained by the multi-band *Roman* photometry (we expect it with less than 20% precision using a stellar isochrone model, e.g., Bressan et al., 2012), and it will become more accurate if D_S is also measured. For evolved source stars, the mass can be constrained via the age distribution of the bulge. In this paper, we evaluate the *Roman* ability to characterize the physical parameters of the xallarap companions by adopting (σ_{M_P}/M_P) in Equation (4.16). Of course, the resultant errors on the companion's masses will become somewhat larger than the 30% $(\sigma_{M_P}/M_P = 0.3)$ due to errors on D_S, $\theta_{\rm E}$ and M_S. However, we expect the mass measurements would be possible by *Roman* with less than 40% precision in most cases even if all the errors were included.

[1] They also show that source companions with short orbital periods of $P \leq 1$ yr hardly affect the measurements of the astrometric signatures.

Reference

Akeson, R. L., Chen, X., Ciardi, D., et al. 2013, PASP, 125, 989

Alard, C. 2000, A&AS, 144, 363

Alard, C., & Lupton, R. H. 1998, ApJ, 503, 325

Albrow, M. D., Horne, K., Bramich, D. M., et al. 2009, MNRAS, 397, 2099

An, J. H., Albrow, M. D., Beaulieu, J. P., et al. 2002, ApJ, 572, 521

André, P., Ward-Thompson, D., & Greaves, J. 2012, Science, 337, 69

Apai, D., Pascucci, I., Bouwman, J., et al. 2005, Science, 310, 834

Armitage, P. J., & Bonnell, I. A. 2002, MNRAS, 330, L11

Bachelet, E., Hinse, T. C., & Street, R. 2018, AJ, 155, 191

Bagheri, F., Sajadian, S., & Rahvar, S. 2019, MNRAS, 490, 1581

Batista, V., Dong, S., Gould, A., et al. 2009, A&A, 508, 467

Batygin, K., & Brown, M. E. 2010, ApJ, 716, 1323

Beaulieu, J. P., Bennett, D. P., Fouqué, P., et al. 2006, Nature, 439, 437

Bennett, D. P. 2008, Detection of Extrasolar Planets by Gravitational Microlensing, ed. J. W. Mason, 47

—. 2010, ApJ, 716, 1408

Bennett, D. P., & Rhie, S. H. 1996, ApJ, 472, 660

—. 2002, ApJ, 574, 985

Bennett, D. P., Bond, I. A., Udalski, A., et al. 2008, ApJ, 684, 663

Bennett, D. P., Rhie, S. H., Nikolaev, S., et al. 2010, ApJ, 713, 837

Bennett, D. P., Sumi, T., Bond, I. A., et al. 2012, ApJ, 757, 119

Bennett, D. P., Batista, V., Bond, I. A., et al. 2014, ApJ, 785, 155

Bennett, D. P., Bhattacharya, A., Anderson, J., et al. 2015, ApJ, 808, 169

Bennett, D. P., Udalski, A., Bond, I. A., et al. 2018, AJ, 156, 113

Bennett, D. P., Bhattacharya, A., Beaulieu, J.-P., et al. 2020, AJ, 159, 68

Bensby, T., Adén, D., Meléndez, J., et al. 2011, A&A, 533, A134

Bensby, T., Yee, J. C., Feltzing, S., et al. 2013, A&A, 549, A147

Bensby, T., Feltzing, S., Gould, A., et al. 2017, A&A, 605, A89

Bhattacharya, A., Bennett, D. P., Anderson, J., et al. 2017, AJ, 154, 59

Bhattacharya, A., Beaulieu, J. P., Bennett, D. P., et al. 2018, AJ, 156, 289

Bond, I. A., Abe, F., Dodd, R. J., et al. 2001, MNRAS, 327, 868

Bond, I. A., Udalski, A., Jaroszyński, M., et al. 2004, ApJ, 606, L155

Bond, I. A., Bennett, D. P., Sumi, T., et al. 2017, MNRAS, 469, 2434

Borucki, W. J., Koch, D., Basri, G., et al. 2010, Science, 327, 977

Boss, A. P. 1997, Science, 276, 1836

—. 2001, ApJ, 563, 367

Bowler, B. P. 2016, PASP, 128, 102001

Boyajian, T. S., van Belle, G., & von Braun, K. 2014, AJ, 147, 47

Bramich, D. M. 2008, MNRAS, 386, L77

Bramich, D. M., Horne, K., Albrow, M. D., et al. 2013, MNRAS, 428, 2275

Bressan, A., Marigo, P., Girardi, L., et al. 2012, MNRAS, 427, 127

Broomhall, A. M., Chaplin, W. J., Davies, G. R., et al. 2009, MNRAS, 396, L100

Burrows, A., Hubbard, W. B., Saumon, D., & Lunine, J. I. 1993, ApJ, 406, 158

Butler, R. P., Wright, J. T., Marcy, G. W., et al. 2006, ApJ, 646, 505

Cabral, N., Lagarde, N., Reylé, C., Guilbert-Lepoutre, A., & Robin, A. C. 2019, A&A, 622, A49

Carnero Rosell, A., Santiago, B., dal Ponte, M., et al. 2019, MNRAS, 489, 5301

Cassan, A., Kubas, D., Beaulieu, J. P., et al. 2012, Nature, 481, 167

Chabrier, G., Segretain, L., & M'era, D. 1996, ApJ, 468, L21

Childs, A. C., Quintana, E., Barclay, T., & Steffen, J. H. 2019, MNRAS, 485, 541

Choi, J. Y., Shin, I. G., Han, C., et al. 2012, ApJ, 756, 48

Chung, S.-J., Han, C., Park, B.-G., et al. 2005, ApJ, 630, 535

Claret, A., & Bloemen, S. 2011, A&A, 529, A75

Cumming, A., Butler, R. P., Marcy, G. W., et al. 2008, PASP, 120, 531

Dieterich, S. B., Henry, T. J., Golimowski, D. A., Krist, J. E., & Tanner, A. M. 2012, AJ, 144, 64

Dominik, M. 1999, A&A, 349, 108

Dominik, M., Jørgensen, U. G., Rattenbury, N. J., et al. 2010, Astronomische Nachrichten, 331, 671

Dominik, M., Bachelet, E., Bozza, V., et al. 2019, MNRAS, 484, 5608

Dong, S., Mérand, A., Delplancke-Ströbele, F., et al. 2019, ApJ, 871, 70

Duchêne, G., & Kraus, A. 2013, ARA&A, 51, 269

Einstein, A. 1936, Science, 84, 506

Emerson, J., & Sutherland, W. 2010, The Messenger, 139, 2

Epchtein, N., de Batz, B., Capoani, L., et al. 1997, The Messenger, 87, 27

Erdl, H., & Schneider, P. 1993, A&A, 268, 453

Festin, L. 1998, A&A, 333, 497

Freeman, M., Philpott, L. C., Abe, F., et al. 2015, ApJ, 799, 181

Fressin, F., Torres, G., Charbonneau, D., et al. 2013, ApJ, 766, 81

Furusawa, K., Udalski, A., Sumi, T., et al. 2013, ApJ, 779, 91

Gaudi, B. S. 1998, ApJ, 506, 533

—. 2002, arXiv e-prints, astro

Gaudi, B. S., Christiansen, J. L., & Meyer, M. R. 2020, arXiv e-prints, arXiv:2011.04703

Gaudi, B. S., Beaulieu, J. P., Bennett, D. P., et al. 2009, in astro2010: The Astronomy and Astrophysics Decadal Survey, Vol. 2010, 85

Gilliland, R. L., Chaplin, W. J., Jenkins, J. M., Ramsey, L. W., & Smith, J. C. 2015, AJ, 150, 133

Giordano, M., Nucita, A. A., de Paolis, F., & Ingrosso, G. 2017, International Journal of Modern Physics D, 26, 1741009

González Hernández, J. I., & Bonifacio, P. 2009, A&A, 497, 497

Gorbikov, E., Brosch, N., & Afonso, C. 2010, Ap&SS, 326, 203

Gould, A. 1994, ApJ, 421, L75

—. 2000, ApJ, 542, 785

—. 2004, ApJ, 606, 319

—. 2013, ApJ, 763, L35

Gould, A., Huber, D., Penny, M., & Stello, D. 2015, Journal of Korean Astronomical Society, 48, 93

Gould, A., & Loeb, A. 1992, ApJ, 396, 104

Gould, A., & Welch, D. L. 1996, ApJ, 464, 212

Gould, A., & Yee, J. C. 2014, ApJ, 784, 64

Gould, A., Udalski, A., An, D., et al. 2006, ApJ, 644, L37

Gould, A., Udalski, A., Monard, B., et al. 2009, ApJ, 698, L147

Gould, A., Dong, S., Gaudi, B. S., et al. 2010, ApJ, 720, 1073

Graff, D. S., & Gaudi, B. S. 2000, ApJ, 538, L133

Grether, D., & Lineweaver, C. H. 2006, ApJ, 640, 1051

Griest, K., & Safizadeh, N. 1998a, ApJ, 500, 37

—. 1998b, ApJ, 500, 37

Hamer, J. H., & Schlaufman, K. C. 2019, AJ, 158, 190

Han, C. 2006, ApJ, 638, 1080

Han, C., & Gould, A. 1997, ApJ, 480, 196

Han, C., & Jeong, Y. 1998, MNRAS, 301, 231

Han, C., Udalski, A., Sumi, T., et al. 2017, ApJ, 843, 59

Hasselquist, S., Zasowski, G., Feuillet, D. K., et al. 2020, ApJ, 901, 109

Hayashi, C. 1981, in Fundamental Problems in the Theory of Stellar Evolution, ed. D. Sugimoto, D. Q. Lamb, & D. N. Schramm, Vol. 93, 113–126

Hayashi, C., Nakazawa, K., & Nakagawa, Y. 1985, in Protostars and Planets II, ed. D. C. Black & M. S. Matthews, 1100–1153

Henry, T. J., Jao, W.-C., Subasavage, J. P., et al. 2006, AJ, 132, 2360

Henry, T. J., & McCarthy, D. W., J. 1990, ApJ, 350, 334

Henry, T. J., & McCarthy, Donald W., J. 1993, AJ, 106, 773

Henry, T. J., Jao, W.-C., Winters, J. G., et al. 2016, in American Astronomical Society Meeting Abstracts, Vol. 227, American Astronomical Society Meeting Abstracts #227, 142.01

Holtzman, J. A., Watson, A. M., Baum, W. A., et al. 1998, AJ, 115, 1946

Howard, A. W., Marcy, G. W., Johnson, J. A., et al. 2010, Science, 330, 653

Howard, A. W., Marcy, G. W., Bryson, S. T., et al. 2012, ApJS, 201, 15

Howard, C. D., Rich, R. M., Reitzel, D. B., et al. 2008, ApJ, 688, 1060

Ida, S., & Lin, D. N. C. 2004, ApJ, 604, 388

—. 2005, ApJ, 626, 1045

Johansen, A., & Lambrechts, M. 2017, Annual Review of Earth and Planetary Sciences, 45, 359

Johnson, J. A., Howard, A. W., Marcy, G. W., et al. 2010, PASP, 122, 149

Johnson, S. A., Penny, M., Gaudi, B. S., et al. 2020, AJ, 160, 123

Jung, Y. K., Udalski, A., Yee, J. C., et al. 2017a, AJ, 153, 129

Jung, Y. K., Udalski, A., Bond, I. A., et al. 2017b, ApJ, 841, 75

Jung, Y. K., Gould, A., Zang, W., et al. 2019, AJ, 157, 72

Kennedy, G. M., & Kenyon, S. J. 2008, ApJ, 673, 502

Kenyon, S. J., & Hartmann, L. 1995, ApJS, 101, 117

Khakpash, S., Penny, M., & Pepper, J. 2019, AJ, 158, 9

Kim, S.-L., Lee, C.-U., Park, B.-G., et al. 2016, Journal of Korean Astronomical Society, 49, 37

Koch, D. G., Borucki, W. J., Basri, G., et al. 2010, ApJ, 713, L79

Kroupa, P., & Tout, C. A. 1997, MNRAS, 287, 402

Kumar, S. S. 1962, AJ, 67, 579

Laughlin, G., Bodenheimer, P., & Adams, F. C. 2004, ApJ, 612, L73

Lewis, G. F. 2001, A&A, 380, 292

Lindegren, L., Bastian, U., Biermann, M., et al. 2020, arXiv e-prints, arXiv:2012.01742

Lissauer, J. J. 1993, ARA&A, 31, 129

Loeb, A., & Gaudi, B. S. 2003, ApJ, 588, L117

Loeb, A., & Sasselov, D. 1995, ApJ, 449, L33

Luhman, K. L. 2012, ARA&A, 50, 65

Luhman, K. L., Adame, L., D'Alessio, P., et al. 2005, ApJ, 635, L93

Mao, S., & Paczynski, B. 1991, ApJ, 374, L37

Marcy, G. W., & Butler, R. P. 2000, PASP, 112, 137

Matzner, C. D., & Levin, Y. 2005, ApJ, 628, 817

Mayor, M., & Queloz, D. 1995, Nature, 378, 355

Mayor, M., Marmier, M., Lovis, C., et al. 2011, arXiv e-prints, arXiv:1109.2497

McDonald, I., Kerins, E., Penny, M., et al. 2014, MNRAS, 445, 4137

Miyazaki, S., Sumi, T., Bennett, D. P., et al. 2018, AJ, 156, 136

—. 2020, AJ, 159, 76

Mogavero, F., & Beaulieu, J. P. 2016, A&A, 585, A62

Mollière, P., & Mordasini, C. 2012, A&A, 547, A105

Montet, B. T., Yee, J. C., & Penny, M. T. 2017, PASP, 129, 044401

Mordasini, C., Alibert, Y., Benz, W., & Naef, D. 2009, A&A, 501, 1161

Morris, S. L. 1985, ApJ, 295, 143

Mróz, P., Udalski, A., Skowron, J., et al. 2017, Nature, 548, 183

Nakagawa, Y., Hayashi, C., & Nakazawa, K. 1983, Icarus, 54, 361

Nakagawa, Y., Sekiya, M., & Hayashi, C. 1986, Icarus, 67, 375

Nakajima, T., Oppenheimer, B. R., Kulkarni, S. R., et al. 1995, Nature, 378, 463

Nataf, D. M., Gould, A., Fouqué, P., et al. 2013, ApJ, 769, 88

Niikura, H., Takada, M., Yasuda, N., et al. 2019, Nature Astronomy, 3, 524

Nishiyama, S., Tamura, M., Hatano, H., et al. 2009, ApJ, 696, 1407

Nucita, A. A., Giordano, M., De Paolis, F., & Ingrosso, G. 2014, MNRAS, 438, 2466

O'Brien, D. P., Izidoro, A., Jacobson, S. A., Raymond, S. N., & Rubie, D. C. 2018, Space Sci. Rev., 214, 47

Oka, A., Nakamoto, T., & Ida, S. 2011, ApJ, 738, 141

Paczynski, B. 1986, ApJ, 304, 1

Penny, M. T., Gaudi, B. S., Kerins, E., et al. 2019, ApJS, 241, 3

Penny, M. T., Henderson, C. B., & Clanton, C. 2016, ApJ, 830, 150

Penny, M. T., Kerins, E., & Mao, S. 2011, MNRAS, 417, 2216

Penny, M. T., Kerins, E., Rattenbury, N., et al. 2013, MNRAS, 434, 2

Poindexter, S., Afonso, C., Bennett, D. P., et al. 2005, ApJ, 633, 914

Pollack, J. B., Hubickyj, O., Bodenheimer, P., et al. 1996, Icarus, 124, 62

Rahvar, S., & Dominik, M. 2009, MNRAS, 392, 1193

Ranc, C., Cassan, A., Albrow, M. D., et al. 2015, A&A, 580, A125

Rattenbury, N. J., Bond, I. A., Skuljan, J., & Yock, P. C. M. 2002, MNRAS, 335, 159

Rebolo, R., Zapatero Osorio, M. R., & Martín, E. L. 1995, Nature, 377, 129

Refsdal, S. 1966, MNRAS, 134, 315

Robin, A. C., Marshall, D. J., Schultheis, M., & Reylé, C. 2012, A&A, 538, A106

Robin, A. C., Reylé, C., Derrière, S., & Picaud, S. 2003, A&A, 409, 523

Rybicki, K., & Wyrzykowski, Ł. 2014, Acta Astron., 64, 65

Ryu, Y. H., Yee, J. C., Udalski, A., et al. 2018, AJ, 155, 40

Sajadian, S., & Rahvar, S. 2010, MNRAS, 407, 373

Sako, T., Sekiguchi, T., Sasaki, M., et al. 2008, Experimental Astronomy, 22, 51

Santerne, A., Moutou, C., Tsantaki, M., et al. 2016, A&A, 587, A64

Santos, N. C., Israelian, G., & Mayor, M. 2001, A&A, 373, 1019

Schechter, P. L., Mateo, M., & Saha, A. 1993, PASP, 105, 1342

Shin, I. G., Yee, J. C., Gould, A., et al. 2019, AJ, 158, 199

Shporer, A. 2017, PASP, 129, 072001

Shvartzvald, Y., & Maoz, D. 2012, MNRAS, 419, 3631

Shvartzvald, Y., Maoz, D., Udalski, A., et al. 2016, MNRAS, 457, 4089

Skowron, J., & Gould, A. 2012, arXiv e-prints, arXiv:1203.1034

Skowron, J., Udalski, A., Gould, A., et al. 2011, ApJ, 738, 87

Skowron, J., Udalski, A., Kozłowski, S., et al. 2016, Acta Astron., 66, 1

Skrutskie, M. F., Cutri, R. M., Stiening, R., et al. 2006, AJ, 131, 1163

Smith, M. C., Mao, S., & Paczyński, B. 2003, MNRAS, 339, 925

Spergel, D., Gehrels, N., Baltay, C., et al. 2015, arXiv e-prints, arXiv:1503.03757

Sumi, T., & Penny, M. T. 2016, ApJ, 827, 139

Sumi, T., Abe, F., Bond, I. A., et al. 2003, ApJ, 591, 204

Sumi, T., Bennett, D. P., Bond, I. A., et al. 2010, ApJ, 710, 1641

Sumi, T., Kamiya, K., Bennett, D. P., et al. 2011, Nature, 473, 349

Sumi, T., Bennett, D. P., Bond, I. A., et al. 2013, ApJ, 778, 150

Sumi, T., Udalski, A., Bennett, D. P., et al. 2016, ApJ, 825, 112

Suzuki, D., Bennett, D. P., Sumi, T., et al. 2016, ApJ, 833, 145

Suzuki, D., Bennett, D. P., Ida, S., et al. 2018, ApJ, 869, L34

Swastik, C., Banyal, R. K., Narang, M., et al. 2020, arXiv e-prints, arXiv:2012.13694

Szulágyi, J., Morbidelli, A., Crida, A., & Masset, F. 2014, ApJ, 782, 65

Szymański, M. K., Udalski, A., Soszyński, I., et al. 2011, Acta Astron., 61, 83

Tanigawa, T., & Tanaka, H. 2016, ApJ, 823, 48

Terry, S. K., Bhattacharya, A., Bennett, D. P., et al. 2020, arXiv e-prints, arXiv:2009.08461

Trifonov, T., Tal-Or, L., Zechmeister, M., et al. 2020, A&A, 636, A74

Tsapras, Y., Street, R., Horne, K., et al. 2009, Astronomische Nachrichten, 330, 4

Udalski, A., Szymański, M. K., & Szymański, G. 2015, Acta Astron., 65, 1

Udalski, A., Szymanski, M., Stanek, K. Z., et al. 1994, Acta Astron., 44, 165

Udalski, A., Ryu, Y. H., Sajadian, S., et al. 2018, Acta Astron., 68, 1

Verde, L., Peiris, H. V., Spergel, D. N., et al. 2003, ApJS, 148, 195

Wahl, S. M., Hubbard, W. B., Militzer, B., et al. 2017, Geophys. Res. Lett., 44, 4649

Weidenschilling, S. J. 1977, MNRAS, 180, 57

Winters, J. G., Irwin, J., Newton, E. R., et al. 2018, AJ, 155, 125

Witt, H. J. 1990, A&A, 236, 311

Witt, H. J., & Mao, S. 1994, ApJ, 430, 505

Wozniak, P. R. 2000, Acta Astron., 50, 421

Wright, J. T., Marcy, G. W., Howard, A. W., et al. 2012, ApJ, 753, 160

Yee, J. C., Udalski, A., Sumi, T., et al. 2009, ApJ, 703, 2082

Yee, J. C., Shvartzvald, Y., Gal-Yam, A., et al. 2012, ApJ, 755, 102

Yee, J. C., Udalski, A., Calchi Novati, S., et al. 2015, ApJ, 802, 76

Yoo, J., DePoy, D. L., Gal-Yam, A., et al. 2004, ApJ, 603, 139

Youdin, A. N., & Goodman, J. 2005, ApJ, 620, 459

Youdin, A. N., & Shu, F. H. 2002, ApJ, 580, 494

Zhu, W., Petrovich, C., Wu, Y., Dong, S., & Xie, J. 2018, ApJ, 860, 101

Zhu, W., Udalski, A., Novati, S. C., et al. 2017, AJ, 154, 210

Zoccali, M., Renzini, A., Ortolani, S., et al. 2003, A&A, 399, 931

Zuckerman, B., & Becklin, E. E. 1987, Nature, 330, 138